Overcoming geological challenges in the construction of a CFSGD diversion tunnel

Connecting Communities Through Underground Infrastructure – Eberhardt et al. (Eds)
© 2026 The Author(s), ISBN: 978-1-041-35997-5

Overcoming geological challenges in the construction of a CFSGD diversion tunnel

A.A. Mert, M. Salman and F. Çalışkan
General Directorate of State Hydraulic Works, Dams and HEPP Department, Ankara, Turkey

ABSTRACT: The Kırık Dam, a concrete-faced sand-gravel fill dam in Turkey, required a 690 m long, 3.5 m diameter horseshoe diversion tunnel. During excavation, the tunnel encountered extremely weak and water-sensitive graphite schist of the Susuz Formation, conditions far worse than anticipated. This led to a major chimney-shaped collapse at the tunnel entrance (Sta. 0+164) and severe, progressive deformations at the outlet (Sta. 0+670), classifying the ground as NATM Class C2 (Squeezing). Initial and upgraded support systems, including Type 6A, 6A-1, and 6A-2 (spiling), proved insufficient and failed to halt ground movement, leading to the suspension of works. The final successful solution involved a major design revision to the Type 6B support system. This robust system featured a dense 3.5” diameter umbrella arch (forepoling), systematic 6 m long Ø32 IBO (self-drilling) bolts at 0.50 m x 0.50 m spacing, heavy INP 200 steel ribs at 0.50 m intervals, and 30 cm of double-layer (Q335×335) steel mesh shotcrete. Numerical analysis confirmed the stability of this design, with calculated loads (24.2 tons) remaining within the IBO bolts’ capacity (25 tons). This case study highlights the failure of conventional support in squeezing ground and demonstrates the success of an adaptive, robust pre-support and systematic reinforcement strategy.

1 INTRODUCTION

1.1 *Project background and purpose*

The Kirik Dam project on the Karasu Creek involves a Concrete-Faced Sand-Gravel Fill Dam (CFSGD) rising 89.00 m above the thalweg. A critical component is the diversion tunnel, designed to manage the creek’s flow during construction and later serve as a sluice outlet for irrigation and water supply. The general field conditions and topographical layout of the diversion tunnel inlet and outlet portals are illustrated in Figure 1.

Figure 1. General field photographs of the diversion tunnel project site: (a) view of the tunnel inlet area; (b) view of the tunnel outlet area.

DOI: 10.1201/9781042001064-420

Initial designs for the 690 m long, horseshoe-profile tunnel were revised from a 3.0 m to a - 3.5 m diameter to improve maintenance access. The tunnel route passes primarily through the Susuz Formation (schists) and the Boyali Formation (serpentine and diabases). The spatial relationship between the finalized route and the complex geological units is illustrated in Figure 2, providing a basis for the subsequent stability analyses.

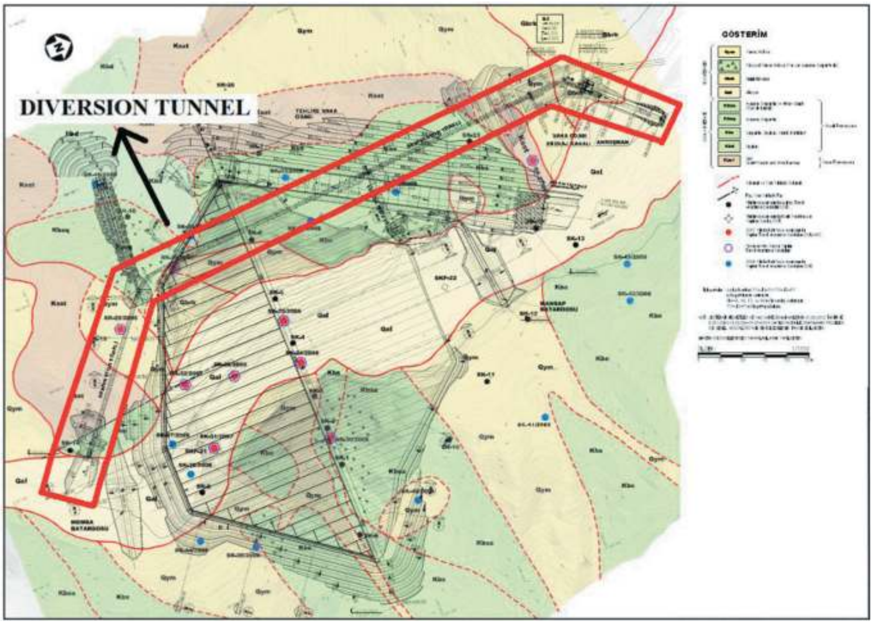

Figure 2. Tunnel alignment and generalized stratigraphy.

1.2 *Anticipated geology and initial design approach*

The drive crosses Susuz (graphite/sericite schists) and Boyali (serpentinite/diabase) units, with ≈31% of the alignment expected in thinly laminated, water-sensitive graphite/sericite schists. Rock-mass classifications indicated RMR ≈ 23 and Q ≈ 0.079, anticipating NATM Class C2 squeezing (ÖNORM B 2203-1, 2017). Early support concepts combined shotcrete, mesh, systematic bolts, and steel ribs; heavier Type 6A-2 support included spiling (Barton et al., 1974; Bieniawski, 1989; Hoek et al., 2000). A comprehensive representation of the subsurface conditions, including the spatial distribution of the schist and diabase units, is presented in Figure 3.

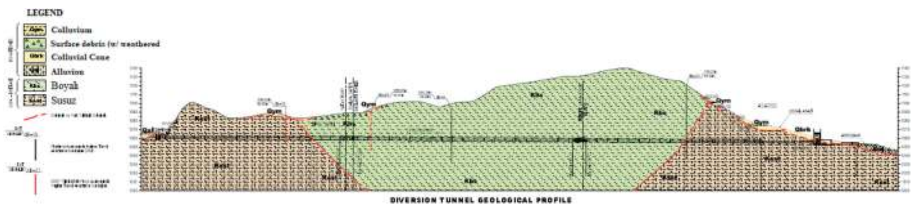

Figure 3. Geological profile through diversion tunnel alignment.

1.3 *Scope of the paper*

This work summarizes failures at the inlet and outlet, critique interim support variants (6A/6A-1/6A-2), and present the final TYPE 6B umbrella-arch & IBO solution verified by numerical checks and field monitoring.

2 GEOLOGICAL SETTING AND SQUEEZING INDICATORS

2.1 *Water-sensitive schists and degradation mechanisms*

Graphite and sericite schists disintegrate, erode, and transport when exposed to air/water. Laminated structure and low effective confinement favour upward chimney-shaped failure and face extrusion under stress redistribution; inflow of loose cover/colluvium can occur near portals (Hoek & Guevara, 2009; Hoek et al., 2000).

2.2 *Classification outcomes and design implications*

RMR ≈ 23 and Q ≈ 0.079 place the ground at the poor/very-poor end, consistent with NATM Class C2. Design implications include (i) dense pre-support (umbrella arch), (ii) systematic, actively tensioned rock reinforcement (IBO/self-drilling), (iii) close rib spacing with robust shot-crete/mesh, and (iv) an invert arch to complete confinement.

3 FAILURE EVENTS AND INITIAL MITIGATIONS

3.1 *Inlet collapse at Sta. 0+164*

Tunnel excavation from the entrance portal proceeded to Sta. 0+162.00, but work was halted due to excessive spalling. Subsequently, a major collapse occurred around Sta. 0+164.00 within the graphite schist unit. This failure created a massive, chimney-shaped void measuring 8 meters in diameter and 19 meters in length, which extended upwards until it daylighted at the natural ground surface. The scale of this instability and its progression from the tunnel crown to the surface are documented in Figure 4.

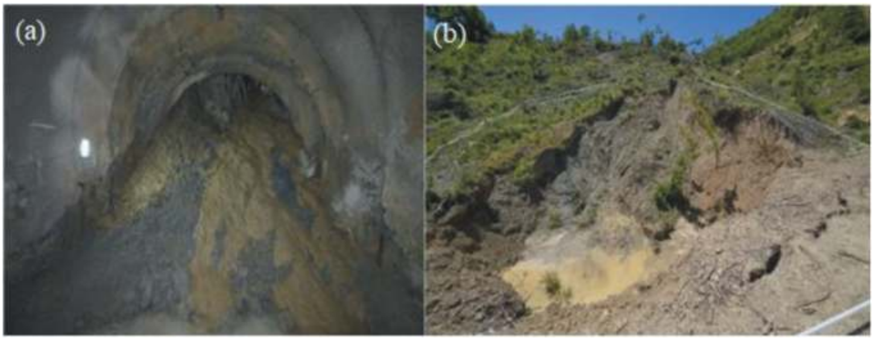

Figure 4. Photos of the chimney-shaped collapse at the tunnel entrance (Sta. 0+164): (a) Internal view showing the failure of the primary lining and accumulation of debris; (b) External manifestation of the collapse on the natural slope surface, illustrating the upward propagation of the instability.

Following the collapse, an attempt was made to restart excavation using the Type 6A-2 support system, which included steel ribs with spiling. This intervention proved insufficient. The implemented spiles were inadequate in both length and thickness to withstand the ground load, causing them to bend and buckle. Due to the inability to safely stabilize the collapse zone, excavation at the tunnel entrance was suspended.

3.2 *Outlet deformations and interventions*

3.2.1 *Initial support upgrade to Type 6A-1*

Excavation from the outlet portal also encountered immediate instability. In the first 20 m, the support was upgraded from the standard Type 6A to Type 6A-1. This upgrade involved installing additional steel ribs, reducing the spacing from 50 cm to 25 cm. Furthermore, tension rods were installed between opposing rib bases and encased in concrete to minimize the effects of ground stress.

3.2.2 *Slope instability and conduit construction*

The geological structure at the outlet portal (clay, colluvium, and altered schist) was highly unstable. Local mass movements on the slope face, exacerbated by atmospheric exposure, threatened the portal. To mitigate this surface instability and allow for safe tunnel commencement, an approximately 20 m long cut-and-cover conduit structure was constructed at the tunnel exit.

Figure 5. Observed structural distress and the remedial measure: (a) Severe deformation of the primary lining with highlighted areas of crown distress and longitudinal cracking; (b) View of the stabilized structure following the 20 m extension of the conduit.

3.2.3 *Observed deformations and structural failures*

Despite the conduit and the upgraded Type 6A-1 support, excavation beyond the conduit (past Sta. 0+670) remained difficult. After advancing approximately 20 m, significant deformations were observed in the installed steel ribs, with movements of 2.5 cm measured over two days.

As instability worsened, ground stresses caused severe structural failures at the critical interface between the tunnel exit and the conduit. The concrete surface experienced ruptures spanning 100 cm, exposing the internal reinforcement bars and demonstrating the high magnitude of the ground load being transmitted to the structure. Figure 6 documents the resulting structural degradation, including the localized crushing of the lining and the failure of the steel support members.

Figure 6. View of the tunnel sections: (a) Close-up view of the structural collapse, showing twisted steel ribs and fractured shotcrete resulting from excessive ground pressure; (b) View of the final completed concrete lining, showing the stable condition achieved after overcoming the initial support failure.

3.3 *Why TYPE 6A/6A-1/6A-2 proved inadequate*

Spiles (Type 6A-2) lacked length/thickness and could not mobilize sufficient arching ahead of the face; rib spacing and shotcrete capacity were insufficient against deep plastic zones typical of C2 squeezing. The absence of an invert arch aggravated floor heave and lateral spread.

4 PROBLEM ESCALATION AND ADVANCED MITIGATION

4.1 *Failure of Type 6A-2 support at the outlet*

During the excavation for rib placement in the first 3 m past Sta. 0+670, loose material from above the crown flowed uncontrolled into the tunnel. Following this event, the Type 6A-2 spiling support project was reapplied in the critical section between Sta. 0+670 and Sta. 0+663.50.

This intervention also failed. The ground experienced significant deformations and torsional distortions, particularly on the left side (relative to flow). The excavation could not be advanced, and work at the outlet section was halted due to safety risks.

4.2 *Extensive deformation and secondary collapse*

The instability in the outlet section (Sta. 0+690.00 to Sta. 0+670.00) escalated into a secondary collapse. The tunnel axis underwent chimney-shaped widening upwards, eventually connecting with the slope surface. Measurements in this zone revealed extreme deformations: a maximum movement of 63 cm in the tunnel axis and 48 cm at the sidewalls.

These events confirmed the complete inadequacy of the Type 6A, 6A-1, and 6A-2 support systems against the squeezing-ground conditions.

4.3 *Final design revision: Type 6B*

With excavation suspended at both ends, a robust solution was required. A joint site inspection by DSI and the contractor led to a major project revision: the implementation of the Type 6B support system. This system was specifically designed for the high-stress NATM C2 (Squeezing) conditions identified in the graphite schists.

The Type 6B design included:

- An umbrella arch (forepoling) using 3.5” diameter, 9 m long pipes at a close 20 cm spacing over the upper 150° of the crown.
- Systematic L=6.00 m, Ø32 IBO (self-drilling) bolts, six per rib bay (3L+3R) at a dense 0.50 m × 0.50 m spacing.
- INP 200 steel ribs spaced at 0.50 m intervals.
- 30 cm of C20/25 shotcrete.
- Two layers of Q335×335 steel mesh.
- An invert arch to create a fully closed support ring.

The technical specifications and geometric arrangement of these reinforcement components, particularly the interaction between the umbrella arch and the radial IBO bolting, are detailed in Figure 7.

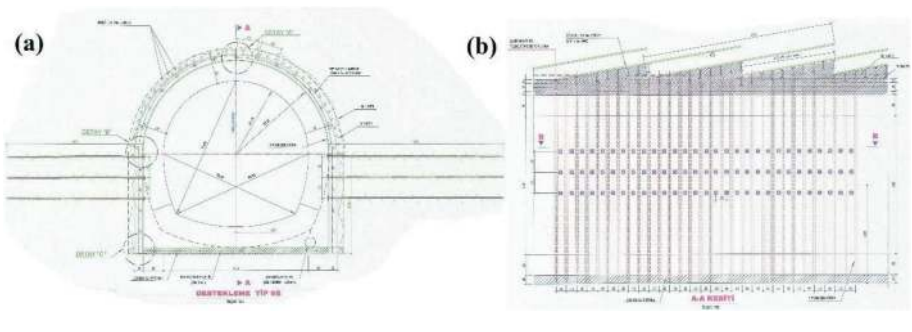

Figure 7. Detailed technical drawing of Type 6B umbrella-arch pre-support system: (a) Transverse cross-section illustrating the semi-circular pattern of the canopy and the specified IBO reinforcement zones; (b) Longitudinal profile (Section A-A) showing the overlapping pipe sequence, grouting intervals, and the spatial relationship between the pre-support and the tunnel face.

The pre-support installation is conducted in a bay-by-bay manner, adhering to a strict procedural sequence. This sequence encompasses: (1) drilling and grouting of Injectable Borehole Anchors (IBOs), (2) installation of forepoles, (3) placement of steel ribs with an initial shotcrete and mesh layer, and (4) early closure of the invert. Following this, the IBOs are tightened to a calibrated torque. This entire process is managed by systematic convergence monitoring, which provides the data to inform adjustments in advance length and stand-time.

While steel canopy tubes are a standard NATM element, their application in the Kirik Dam diversion tunnel was necessitated by extreme geotechnical constraints that rendered standard spiling (Type 6A-2) ineffective. The primary innovation of the Type 6B system in this context was the integration of self-drilling IBO (Injectable Boreable) bolts with the umbrella arch to manage a rock mass that was essentially non-cohesive and water-sensitive.

In the Susuz Formation schists, drilled holes would collapse immediately, making the installation of conventional rock bolts impossible. The use of Ø32 IBO bolts allowed for simultaneous drilling and high-pressure grouting, ensuring that the reinforcement was fully bonded to the surrounding ground despite its poor quality. Furthermore, unlike standard passive spiling, the IBO bolts were actively tensioned to 2 tons using calibrated torque wrenches 18–24 hours after grouting, creating an immediate confined “reinforced ring” ahead of and around the face. This active, high-density reinforcement strategy (0.50m x 0.50m spacing) was the critical factor in arresting the progressive squeezing (NATM Class C2) that had previously caused deformations of up to 63 cm.

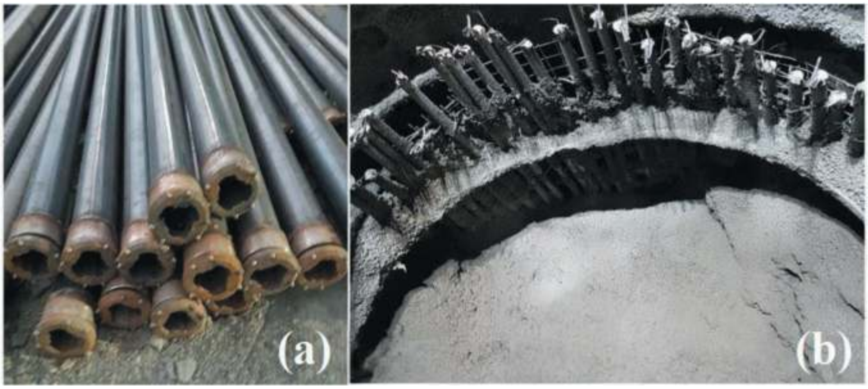

Figure 8. Type 6B support: (a) before; and (b) after application.

5 FINAL IMPLEMENTATION AND ANALYSIS

5.1 *Geotechnical re-assessment and numerical analysis*

The final design was based on detailed geological assessments (borings, RMR, Q, GSI) and numerical analyses (e.g., Phase2) (Rocscience, 2018). The evaluations confirmed the rock mass as RMR 23 (Weak Rock) and NATM C2 (Squeezing), validating the need for the heavy, closed-ring Type 6B support.

Numerical analysis of the Type 6B design confirmed its robustness. The maximum calculated force on the IBO bolts was 24.2 tons, which was safely within the 25-ton capacity of the bolts, indicating the system could withstand the high ground stresses. Figure 9 illustrates the computational framework used for these verifications, including the mesh configuration and the resulting vectorial distribution of ground movement.

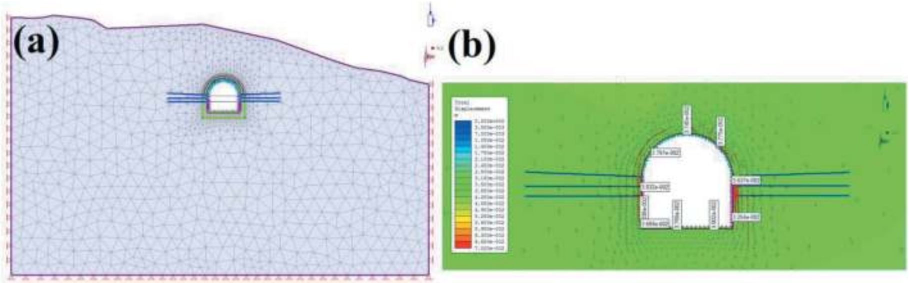

Figure 9. Numerical analysis and resultant deformation patterns for Type 6B reinforcement: (a) Finite element mesh discretization and boundary conditions; (b) Results showing the distribution of total displacement vectors.

5.2 *Successful application and system comparison*

The Type 6B system was implemented in the critical unstable zones at both the entrance (Sta. 0 +164) and the exit (Sta. 0+690 to Sta. 0+658). This system proved effective where all previous types had failed. Table 1 provides a comparison of the support systems applied.

Table 1. Comparison of Type 6 support systems applied in the tunnel.

Support Type	**Rock Mass Class**	**Rock Bolt / IBO (Spacing)**	**Shotcrete & Mesh**	**Steel Arch (Spacing)**	**Forepoling**
6	VW (RMR<20)	SB: 1.0 × 1.5m	20 cm + 2 × Q188/188	INP 160 @ 1.5m	None
6A	VW (Q<0.02)	SB: 1.0 × 1.0m	20 cm + 2 × Q188/188	INP 160 @ 1.0m	None
6A-1	Instability/ High Risk	RB: 1.0 × 1.0m	20 cm + 2 × Q188/188	INP 160 @ 0.25m	None
6A-2	Severe Instability/ Collapse	RB: 1.0 × 1.0m	20 cm + 2 × Q188/188	INP 160 @ 1.0m	Spiles (Steel Pipe) L=4m @ 0.2m
6B	Poor (NATM C2, Squeezing Locally, RMR 23)	IBO: 0.5 × 0.5m	30 cm + 2 × Q335×335	INP 200 @ 0.5m	Umbrella Ø=3.5”, L=9m Upper 150° @ 0.2m

Notes (Abbreviations): VW: Very Weak; SB: Systematic Bolt (L=2.5m, Ø26); RB: SN-Type (L=2.5m, Ø26); IBO: R32N (L=6m); L: length; Ø: diameter; s: spacing; t: thickness; RMR: Rock Mass Rating; Q: NGI Q-system; NATM: New Austrian Tunnelling Method.

The failures of Type 6A-1 (insufficient passive support) and Type 6A-2 (inadequate spile length/thickness) highlighted the gap between conventional support and the demands of squeezing ground. The success of Type 6B was attributed to its integrated, high-capacity design, combining robust pre-support (umbrella arch) with systematic, high-density active support (IBO bolts).

5.3 *Project completion*

The approved Type 6B design provided the necessary stabilization to re-start and complete the excavation through the collapsed and deformed zones. This robust intervention allowed the project to proceed swiftly, ensuring the long-term integrity of the tunnel structure for the final concrete lining.

6 CONCLUSIONS

The Kırık Dam diversion tunnel excavation transformed from a standard excavation into a critical geotechnical challenge upon encountering weak, water-sensitive graphite schists. The primary lesson from this case study is the documented failure of conventional and intermediate support systems (spiling, increased rib density) in managing NATM C2 (Squeezing) ground conditions.

The initial support designs were incapable of handling the deep plastic zones and high stresses, leading to major collapses and deformations (up to 63 cm). The success of the finally implemented Type 6B system was not due to a single component, but to its integrated, multifaceted design: 1) robust pre-support via a dense umbrella arch, 2) systematic, high-capacity soil-nailing using IBO bolts, 3) heavy structural elements (I 200 ribs), and 4) a closed-ring design with an invert arch.

This case validates the necessity of adaptive engineering and the contractual flexibility to implement major design revisions when observed ground conditions deviate significantly from initial assessments. For future projects in similar metamorphic formations, geotechnical investigations must explicitly assess squeezing potential, and designs should include pre-approved, high-capacity support systems like Type 6B to ensure project safety and continuity.

ACKNOWLEDGEMENTS

The authors wish to thank the DSI (State Hydraulic Works) General Directorate and Regional Directorate for their technical support and collaboration in resolving the challenging ground conditions encountered during this project.

REFERENCES

Barton, N., Lien, R., & Lunde, J. (1974). Engineering classification of rock masses for the design of tunnel support. *Rock Mechanics*, 6(4), 189–236.

Bieniawski, Z. T. (1989). *Engineering rock mass classifications*. Wiley.

Hoek, E., Kaiser, P. K., & Bawden, W. F. (2000). *Support of underground excavations in hard rock*. CRC Press.

Hoek, E., & Guevara, R. (2009). Overcoming squeezing in the Yacambü–Quibor tunnel, Venezuela. *Rock Mechanics and Rock Engineering*, 42(2), 389–418.

ÖNORM B 2203-1. (2017). Underground construction works - Part 1: Geotechnical design and construction. Austrian Standards Institute.

ROBIT. (2017). Forepoling and umbrella arch systems technical guidelines. Robit Rocktools Ltd.

Rocscience Inc. (2018). Phase2 2D finite element analysis for rock and soil. Toronto, ON: Rocscience Inc.

Performance of Sürgü, Kartalkaya and Tahtaköprü Dams During February 6, 2023 Türkiye-Kahramanmaraş Earthquakes

Performance of Sürgü, Kartalkaya and Tahtaköprü Dams During February 6, 2023 Türkiye-Kahramanmaraş Earthquakes

Sarper Demirdöğen[1], Sefa Yıldırım, Burcu Yelen, Ahmet Ali Mert, Derya Bilyay
General Directorate of State Hydraulic Works (DSI)

Abstract. *The 2023 February 6, Turkiye-Kahramanmaraş earthquake sequence affected numerous dams in the region, with this study focusing on three significant ones: Surgu Dam in Dogansehir-Malatya, Kartalkaya Dam in Pazarcık-Kahramanmaras, and Tahtakopru Dam in Islahiye-Gaziantep. The seismic activity resulted in peak ground accelerations of approximately 0.5 g at Surgu Dam and around 0.7 g at Kartalkaya Dam. These events led to notable permanent deformations at both sites. At Surgu Dam, lateral displacements and settlements at the dam crest were measured at 20 cm and 5 cm, respectively. In contrast, Kartalkaya Dam experienced more severe deformations due to the stronger shaking, with lateral displacements and settlements of 70 cm and 80 cm, respectively. Furthermore, the wingwalls located at the water inlet of the spillway at Kartalkaya Dam suffered from light damage. Importantly, no cracking was observed on either the upstream or downstream slopes of all three dams, indicating their resilience under seismic stress. Moreover, no surface manifestations of soil liquefaction were observed at or near either dam body. Surgu Dam had previously undergone rehabilitation following past seismic events, which likely contributed to its performance in the recent earthquakes. Similarly, Tahtakopru Dam, having been elevated prior to these events, also demonstrated commendable performance. The historical interventions and upgrades at these dams highlight the importance of continual assessment and improvement of dam infrastructure in seismic regions.*

Keyword: *Dams, Site reconnaissance, Earthquakes, Permanent displacement*

1 INTRODUCTION

On February 6, 2023, two significant earthquakes struck the East Anatolian Fault zone in Kahramanmaraş, Türkiye. The first earthquake, with a moment magnitude of M_w 7.8, occurred at 04:17 local time, followed by a second earthquake with a magnitude of M_w 7.6 at 13:24 local time. Between February 6 and March 1, over ten thousand aftershocks were recorded within a 200 km radius of the epicenters. The epicenter of the first event, located near Kahramanmaraş-Pazarcık, had a focal depth of 8.6 km. The second event, with a focal depth of 7.0 km, occurred in the Kahramanmaraş-Elbistan-Ekinözü region (AFAD, 2023; Çetin and Ilgaç, 2023; Çetin et al., 2024a, 2024b, 2024c).

In the region affected by the Kahramanmaraş earthquake sequence, the General Directorate of State Hydraulic Works (*DSI*) of Türkiye operates 140 dams for irrigation, water supply, flood control, and hydropower generation. Despite being subjected to high seismic intensities during two major earthquakes, these dams maintained their water-retaining capabilities, with no uncontrolled water releases reported. This paper evaluates the three dams, Sürgü, Kartalkaya, and Tahtaköprü, which were subjected to detailed field observations following the earthquakes.

[1] sarperdemirdogen@dsi.gov.tr, *General Directorate of State Hydraulic Works, Ankara, Türkiye.*

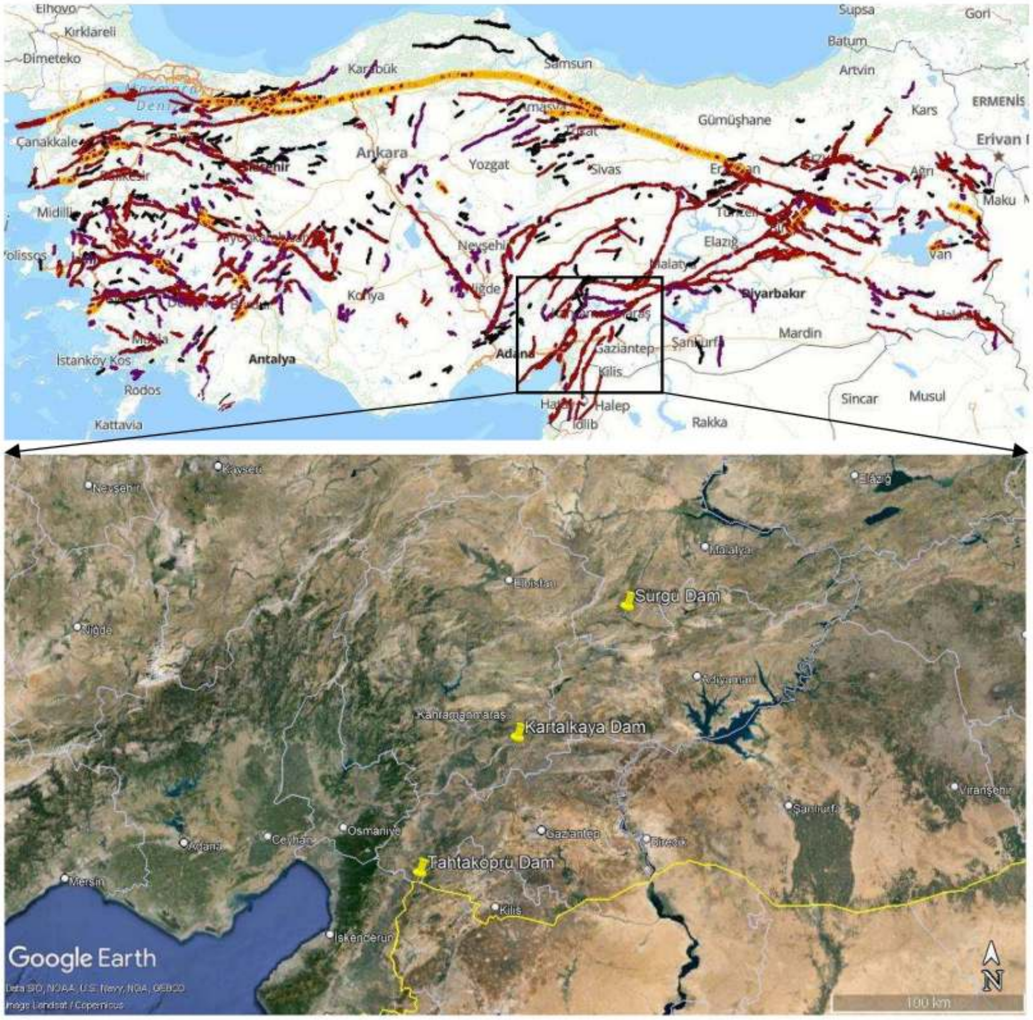

Figure 1: *The locations of Sürgü, Kartalkaya and Tahtaköprü Dams*

2 PERFORMANCE OF SÜRGÜ, KARTALKAYA AND TAHTAKÖPRÜ DAMS

2.1 Sürgü Dam

Sürgü Dam, a rock-fill embankment on the Surgu River in Doğanşehir-Malatya, Türkiye, is 57 meters tall with a crest 736 meters long and 20 meters wide. Completed in 1969 by The State Hydraulic Works of Türkiye, it irrigates 10098 hectares for crops such as apricots and tomatoes and creates Lake Surgu with approximately 71 million cubic meter capacity. The dam has a gated ogee spillway on the left abutment. Originally, the upstream slope had a 1.75H:1V (horizontal:vertical) gradient in the upper sections, transitioning to 2.5H:1V and 3H:1V in the lower sections, while the downstream slope had a 1.75H:1V gradient in the upper sections and 2.5H:1V in the lower sections. After sustaining significant damage from the M_w 5.6 Malatya earthquake in 1986, associated with the Sürgü Fault, the dam underwent rehabilitation. Seismic rockfill retrofitting adjusted the upstream slope to 2.9H:1V and the downstream slope to 2.6H:1V.

Sürgü Dam is located approximately 12 km and 7 km from the fault rupture planes (R_{jb}) of the Pazarcık and Elbistan seismic events, respectively. Although the dam lacks a direct accelerometer measurement, the nearest seismic station with Elbistan data, situated 18.3 km from the rupture plane, recorded a PGA value of 0.47 g in the north-south direction. This recorded value can be considered representative of the seismic conditions at the dam foundation and indicates that the dam experienced significant seismic amplitude.

The photos taken during the site reconnaissance are shown in Fig. 2. Inspections revealed no visible cracking on the upstream and downstream slopes. However, the cracks with widths on the crest ranging from 10 to 25 cm were observed, with depths reaching up to 100 cm. The cracks along the crest were predominantly observed near the upstream section. On the other hand, longitudinal cracks shifted slightly towards the downstream side beyond the maximum section. Differential settlements of up to 5 cm were also observed, which is approximately 0.1% of the total height. This damage can be classified as minor according to Pells and Fell (2002), which aligns with the observations. Although the dam was subjected to high peak ground acceleration (*PGA*) at the site, it exhibited strong performance due to the lack of liquefiable soils on the foundation and the seismic resilience imparted by the prior retrofitting measures.

Figure 2: *Photographs taken during post-earthquake inspections of Sürgü Dam, illustrating moderate levels of cracking along the crest.*

2.3 Kartalkaya Dam

Kartalkaya Dam, a rockfill dam constructed between 1965 and 1972 on the Aksu River in Kahramanmaraş, serves multiple purposes including irrigation, drinking water supply, and industrial water supply. The dam stands 57 m above the riverbed and has a volume of 2323000 m^3. It provides irrigation to 22810 hectares and supplies 45 hm^3 of drinking water annually.

The dam is located at R_{jb} distances of 7.5 km and 59 km from the epicenters of the Pazarcık and Elbistan events, respectively. The nearest seismic station to the dam site recorded a peak ground acceleration (PGA) value of 0.7g during the Pazarcık event, which can be considered representative of the seismic conditions at the dam foundation (Cetin et al., 2024a). It is also known that there is a presence of alluvium beneath the dam.

Fig. 3 shows photographs from a walk-down survey conducted on the dam, indicating no permanent deformations on the downstream and upstream slopes. On the other hand, longitudinal cracks and differential settlements along the crest were identified in the asphalt pavement on the crest road. The maximum width of permanent lateral movement was observed to be up to 80 cm at the center of the crest. Similarly, differential settlements of comparable magnitudes have been observed. This damage can be classified as moderate to major according to Pells and Fell (2002), which aligns with the observed conditions.
Upon examining the auxiliary structures of the dam, it was observed that only the wingwalls at the water inlet of the spillway experienced transverse cracking. However, this is not considered a significant concern in terms of operational status. Additionally, rockfalls have been encountered in many areas on site, further indicating the impact of seismic activity (see Fig. 3).

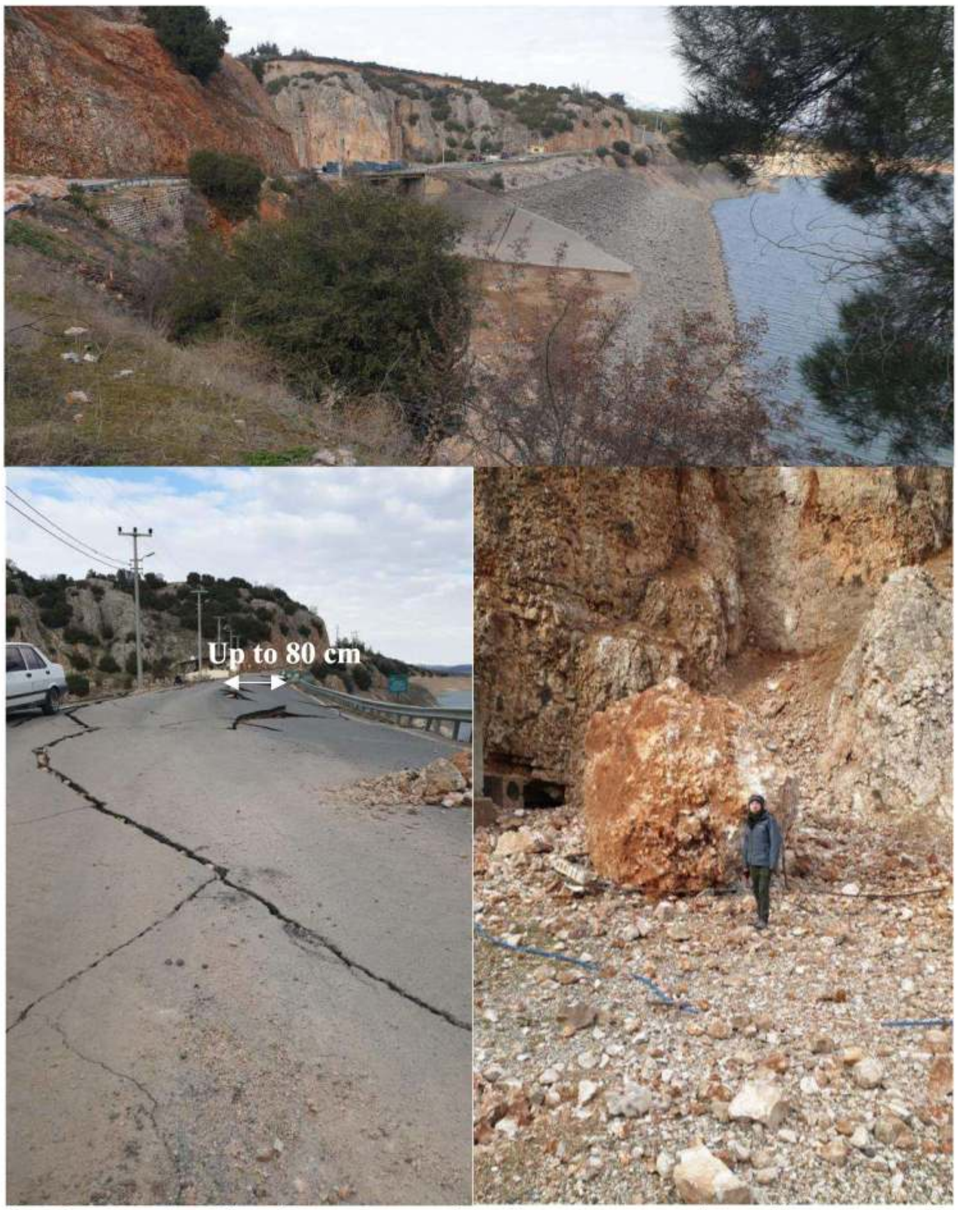

***Figure 3**: Photographs taken during post-earthquake inspections of Kartalkaya Dam, illustrating moderate to major levels of cracking along the crest.*

2.3 Tahtaköprü Dam

The Tahtaköprü Dam, located within the borders of Hatay Province, serves both irrigation benefits for an area of 11575 ha and flood control purposes. The dam, which was completed in 1975, is of a

homogeneous fill type with a clay core and zoned fill. This dam has been elevated for irrigation purposes. The dam's crest width is 10 meters across its entire axis. The crest length of the dam is 400 meters, with an upstream slope of 3H:1V and a downstream slope of 3H:1V.
The Tahtaköprü Dam is located within an R_{jb} distance of 13 km to the Pazarcık fault rupture. The dam is equipped with three seismographs: two are located on the right and left abutments, referring to the rock site, while the third is positioned on the dam crest. The maximum *PGAs* recorded at the dam site were 0.38g at the right abutment, 0.26g at the crest, and 0.16g at the left abutment.
Fig. 4 displays photographs from a walk-down survey conducted on the dam, showing no permanent deformations on the crest, downstream, and upstream slopes. Also, it was observed that minor cracks on the order of millimeters occurred in the auxiliary structures as well.

***Figure 4**: Photographs taken during post-earthquake inspections of Tahtaköprü Dam, illustrating no or slight levels of cracking (DSI, 2023).*

3 CONCLUSIONS

Presented here are select observations of the performance of the Sürgü, Kartalkaya, and Tahtaköprü Dams during the February 6th, 2023, Türkiye earthquakes. Overall, these dams maintained their integrity with no catastrophic breaches and no loss of life, largely due to low reservoir levels at the time of the earthquakes.

The Sürgü Dam benefited significantly from the widening of its crest to nearly twice its original width, which helped limit the damage during the Kahramanmaraş earthquakes. In contrast, the Kartalkaya Dam exhibited moderate to major damage. The presence of alluvium beneath the dam, coupled with higher acceleration values and geometric disadvantages, contributed to its damage. Longitudinal cracks and differential settlements were identified along the crest, with permanent lateral movement up to 80 cm. Additionally, rockfalls and minor transverse cracking in the wingwalls at the spillway inlet were observed, although these did not significantly impact operational status.
The Tahtaköprü Dam, located 13 km from the Pazarcık fault rupture, showed no apparent damage. The maximum *PGA* recorded was 0.38g at the dam site. Despite this measurement, the dam's favorable performance is attributed to its structural elevation for irrigation purposes and lower *PGA* values compared to other dams.
These observations provide good examples of the effectiveness of dam elevation and seismic retrofitting in improving dam resilience. In summary, while the Sürgü and Tahtaköprü Dams exhibited resilience during the seismic events, the Kartalkaya Dam's performance highlighted the importance of considering local geological conditions and structural improvements to mitigate earthquake-induced damages. Moreover, the results observed align with the damage classifications proposed by Pells and Fell (2002).

4 REFERENCES

[1] AFAD (2023) The national disaster emergency management presidency of Türkiye. Available at: https://tadas.afad.gov.tr (accessed 6 August 2024).

[2] Cetin, K. O., Cuceoglu, F., Ayhan, B. U., Yildirim, S., Aydin, S., Demirdogen, S., ER, Y., Gurbuz, A., Moss, R. E. S. (2024a). Performance of hydraulic structures during 6 February 2023 Kahramanmaraş, Türkiye, earthquake sequence. Earthquake Spectra, 87552930241258295.

[3] Cetin, K. O., Ilgaç, M. (2023). Reconnaissance Report on February 6, 2023 Kahramanmaraş-Pazarcık (Mw= 7.7) and Elbistan (Mw= 7.6) Earthquakes. Türkiye Earthquake Reconnaissance and Research Alliance.

[4] Cetin, K.O., Yildirim, S., Demirdogen, S., Cuceoglu, F., Ayhan, B.U. (2024c) Performance of Sultansuyu Dam During February 6, 2023 Türkiye-Kahramanmaraş Earthquake Sequence. Bulletin of Earthquake Engineering.

[5] DSI (2023). Kahramanmaraş Merkezli Depremler Sonrası DSİ 6. Bölge Müdürlüğü Sınırları Dâhilinde Bulunan Depolamalı Tesislere İlişkin Ön İnceleme Raporu (In Turkish).

[6] Pells, S., Fell, R. (2002). Damage and cracking of embankment dams by earthquakes and the implications for internal erosion and piping. University of New South Wales, School of Civil and Environmental Engineering.

Stability of portal slopes of a diversion tunnel after the Kahramanmaraş, Turkey (Türkiye) February 6, 2023 Earthquakes

Tunnelling for a Better Life – Yan, Celestino, Thewes & Eberhardt (Eds)

Stability of portal slopes of a diversion tunnel after the Kahramanmaraş, Turkey (Türkiye) February 6, 2023 Earthquakes

Ahmet Ali Mert* & Fatih Caliskan
General Directorate of State Hydraulic Works, Dams and HEPP Department, Ankara, Turkey

ABSTRACT: This study delves into the stability challenges faced by portal slopes in a diversion tunnel, particularly post-Kahramanmaraş earthquakes in Turkey (February 6, 2023). Geotechnical issues, notably slope failures in portal areas, pose significant threats to tunnel safety and operability. The research analyzes both pre- and post-earthquake scenarios, employing methods like limit equilibrium and pseudo-static analyses. The investigation identifies parameters influencing portal slopes and assesses their behavior under static and dynamic loads. Solutions, including the use of fill and slope flattening (terracing) as a rehabilitation method, are proposed based on comprehensive analyses, field studies, laboratory experiments, and topographic data. The findings contribute valuable insights to combat stability problems in tunnel portal slopes, emphasizing their importance for tunnel safety and longevity. The study aims to guide engineers in developing safer and sustainable solutions for diversion tunnel projects, ultimately enhancing the overall stability and performance of portal slopes.

Keywords: Slope stability, Dams, Diversion tunnels, Earthquakes, Limit equilibrium, Pseudo-static analysis

1 INTRODUCTION

In order Slope stability is an important topic in geotechnical engineering that deals with the assessment of the potential failure or deformation of natural or artificial slopes due to various factors, such as gravity, seepage, external loads, seismicity, and weathering (Day, 2006). Slope stability analysis is necessary for the design and construction of various civil engineering structures, such as dams, embankments, roads, tunnels, excavations, and mines. Slope failure can cause significant economic losses, environmental damages, and human casualties. Therefore, it is essential to evaluate the stability of slopes under different conditions and scenarios using suitable methods and tools.

One of the difficult problems in slope stability analysis is the stability of tunnel portal slopes. Tunnel portals are the openings or entrances of tunnels that connect the underground space with the surface. Tunnel portals are often located on steep slopes that are susceptible to instability due to the excavation process and the presence of weak or fractured rock masses. Moreover, tunnel portals may be exposed to dynamic loads from earthquakes, blasting, or traffic that can generate additional stresses and deformations on the slope. Therefore, tunnel portal slopes need careful design and reinforcement to ensure their safety and functionality (Wang, 2019).

Popescu (2001) conducted a study in which he proposed a concise set of measures to mitigate landslides and recommended a specific format for documenting these landslide remediation efforts (Table 1).

Fatkhiandari et al. (2020) evaluated stability at the Bagong Dam tunnel portals under static and seismic loads using the finite element method. Despite earthquake-induced reductions in the Strength Reduction Factor (SRF), both natural and excavated slopes maintained relative stability.

Oktarina et al. (2023) assessed the stability of Tunnel No. 8 outlet portal under traffic loads, recommending shotcrete reinforcement to prevent instability and landslides in weak rock masses.

Sengkey et al. (2023) analyzed the diversion tunnel portal slopes at Manikin Dam, finding stability issues in the inlet portal slope due to poor mechanical properties of Bobonaro clay.

Huda et al. (2022) studied Lau Simeme Dam's diversion tunnel portals, emphasizing stability under static and earthquake loads. Shotcrete reinforcement was suggested for enhanced stability in poor rock mass conditions.

*Corresponding author: ahmetalimert@utexas.edu

DOI: 10.1201/9781003495505-108

Table 1. Overview of landslide remedial measures (Popescu, 2001).

No.	Category	Remedial Measure
1	Slope Geometry Modification	1.1 Removal of material from the landslide area with potential substitution by lightweight fill
		1.2 Addition of material to maintain stability, using counterweight berms or fill
		1.3 Reduction of the overall slope angle
2	Drainage	2.1 Installation of surface drains to divert water away from the slide area, including collecting ditches and pipes
		2.2 Implementation of shallow or deep trench drains filled with free-draining geomaterials, such as coarse granular fills and geosynthetics
		2.3 Creation of buttress counterforts using coarse-grained materials to achieve a hydrological effect
		2.4 Installation of vertical (small-diameter) boreholes, either pumped or self-draining
		2.5 Establishment of vertical (large-diameter) wells with gravity draining
		2.6 Implementation of sub-horizontal or sub-vertical boreholes
		2.7 Construction of drainage tunnels, galleries, or adits
		2.8 Employment of vacuum dewatering techniques
		2.9 Drainage achieved through siphoning
		2.10 Application of electro-osmotic dewatering techniques
		2.11 Introduction of vegetation planting with a hydrological effect
3	Retaining Structures	3.1 Implementation of gravity-retaining walls
		3.2 Construction of crib-block walls
		3.3 Development of gabion walls
		3.4 Creation of passive piles, piers, and caissons
		3.5 Building cast-in-situ reinforced concrete walls
		3.6 Establishment of reinforced earth-retaining structures with strip/sheet-polymer/metallic-reinforcement elements
		3.7 Installation of buttress counterforts using coarse-grained material to achieve a mechanical effect
		3.8 Deployment of retention nets for rock slope faces
		3.9 Implementation of rock fall attenuation or stopping systems, including rock trap ditches, benches, fences, and walls
		3.10 Use of protective rock/concrete blocks against erosion
4	Internal Slope Reinforcement	4.1 Application of rock bolts
		4.2 Installation of micropiles
		4.3 Implementation of soil nailing techniques
		4.4 Use of anchors, whether pre-stressed or not
		4.5 Application of grouting
		4.6 Creation of stone or lime/cement columns

This study examines stability challenges in diversion tunnel portal slopes, focusing on post-Kahramanmaraş earthquakes in Turkey (February 6, 2023). The earthquakes, magnitudes 7.8 and 7.5, caused widespread damage and numerous fatalities. Portal slope failures pose significant threats to tunnel safety. The research utilizes limit equilibrium and pseudo-static analyses for both pre- and post-earthquake scenarios. Limit equilibrium assesses slope stability by calculating the factor of safety, while pseudo-static analysis simplifies seismic slope stability with constant seismic coefficients (Naseer & Evans, 2020; Hammouri et al., 2008). The investigation identifies parameters influencing portal slopes under static and dynamic loads, proposing solutions such as fill application and slope flattening. Fill material enhances stability by increasing normal stress, reducing pore water pressure, and adding resistance along the potential slip surface (Wang, 2019). The study provides crucial insights for addressing stability issues in tunnel portal slopes, emphasizing thfeir significance for tunnel safety and durability. Intended to guide engineers in developing safer, sustainable solutions for diversion tunnel projects, the research aims to enhance overall stability and efficiency of portal slopes.

2 METHODOLOGY

The dam project involved initial investigations, including 24 foundation borings with a total depth of 1108 m, conducted during the planning stage. These borings were distributed among the dam location (17), two axis locations (17), diversion location (2), spillway route (2), and transmission tunnel (3). In the final project phase, 13 boreholes with a total depth of 400 m were drilled at the dam and construction sites, and 6 boreholes with a total depth of 95 m were drilled at the siphon site on the transmission line. Additionally, 63 pressuremeter tests were performed in 4 boreholes at the dam site.

Parameters for the Rock Mass Rating (RMR) classification method were determined by evaluating field observations, drilling and field studies, literature data, and factors such as weathering, discontinuity conditions, unit boundaries, distribution, and measurements. The RMR method considers parameters related to Rock Quality Designation (RQD), uniaxial compressive strength, joint frequency, joint location, groundwater conditions, and the relationship of the dominant joint system with the slope.

Slope stability analyses were conducted for both inlet and outlet portals, employing the limit equilibrium method for static and seismic conditions (Simplified Bishop, GLE/Morgenstern-Price, Spencer). Pseudo-static slope stability analysis, a simplified approach considering seismic forces as an equivalent static force, was used for seismic conditions. This method assumes instantaneous seismic forces and slope failure under pseudo-static conditions (Duncan and Wright, 2005).

The limit equilibrium analysis involved calculating resisting forces (e.g., frictional forces) and driving forces (e.g., seismic forces, loads) to determine the factor of safety. Analyses considered landslide conditions, landslide prevention support cases, and the aftermath of the February 6, 2023 Kahramanmaraş earthquakes, with corresponding results and recommendations presented.

3 SITE DESCRIPTION

The Ophiolitic complex sediments (Ofk-s) in the project area consist of clay-altered, dispersed, loose, unstable, silicified-radiolarite conglomeratic limestone, and serpentinite blocks. This formation is prevalent at the dam axis, diversion, spillway, relocation roads, post-siphon end sections of the transmission line, and tunnel portal area. Drillings in this formation (Ofk-s) consistently reveal core percentages between 42% and 71%, with an RQD of 0%, indicating a weak and very weak rock mass.

Numerous landslides, both old and active, along with runoff occurrences are observed at the dam axis, mainly within the sedimentary levels of the Ophiolite Complex (Ofk-s). The high alteration of the unit, coupled with weakly cemented clay, sand, gravel, and block-sized material, leads to water absorption during rainy seasons. This absorption causes clay layers to swell, increasing the mass's weight and resulting in mud flow along the slopes.

Vertical faults have developed in the project area within the Ophiolite Complex and at the junction of this unit and the Midyat Formation. Another important fault is the reverse fault at the junction of the Ultrabasics (Ofk-u) and Volcanites (Ofk -v) within the Ophiolite Complex. The ophiolite unit was observed in the field as weakly to very weakly fractured, fragmented and weathered with the influence of these faults and the Eastern Anatolian fault line.

At the inlet and outlet portals and side slope excavations of the diversion tunnel, it was observed that the unit consists of silicified radiolarite units of the ophiolite complex which is clayified, dispersed, weak-very weak rock in places. The portal location is on the dry stream route and water discharge during rainfall comes to the portal excavation slopes through this stream. This unit is clayified in contact with water such as rain and snow, causing surface flows and landslides.

Below are the obtained geotechnical parameters to be used in analyses.

Table 2. General geotechnical parameters.

Parameters	Cohesion (kPa)	Internal Friction Angle (º)
Very weak altered rock near the surface	25	3
Compacted unsorted material to be used in the embankment	5	25
Rock fill	0	40

It is recommended to place 1.00 m of rockfill on slopes to prevent yielding and ensure stability. Seismic hazard analysis indicates peak ground accelerations: MDE (Maximum Design Earthquake) = 0.28g, OBE (Operation Based Earthquake) = 0.14g. Borehole results on the tunnel route show weathered ophiolite (0.00-11.00 m) and ophiolite complex (11.00-50.00 m). Groundwater level is 1.10 m. Borehole tests include permeability, pressurized water, and standard penetration tests at various levels. Rock core samples underwent uniaxial compressive strength and point loading tests (Table 3).

Geotechnical parameters for the weak rock of the ophiolitic unit in the diversion section are cohesion in the range of 100-200 kPa and internal friction angle in the range of 15°-25°.

For the ophiolite complex (siliceous shale), 75 kPa cohesion, 20° angle of internal friction, 25 kN/m^3 unit volume weight were selected as the strength parameters to be used in the calculations considering the calculations and evaluations made for the values of mi = 7 and GSI = 32, uniaxial compression test result 23 kg/cm^2 from laboratory results, as well as laboratory data and field observations.

3.1 *Tunnel inlet*

Diversion Tunnel entrance and water intake structure excavations had been completed. Although there was a requirement for typical slope reinforcement if necessary for excavations to be carried out in the open, only the first benches of the tunnel entrance portal were supported with mesh steel and shotcrete in the diversion tunnel entrance excavations. Diversion tunnel entrance portal, water intake structure and route excavation slopes were opened in ophiolitic unit which is weak to very weak rock. The excavations were exposed without support for a long time, and landslides and flows occurred on the slopes due to the effect of water and rainwater in the unit. It was observed that the additional benches opened in the diversion tunnel route excavations were very close to the dam plinth route.

3.2 *Tunnel inlet*

The exit excavations of the diversion tunnel had been completed, while conduit excavation had not yet commenced. Despite the necessity for standard

Table 3. Ophiolite complex laboratory test results.

Depth (m)	Unit Weight (g/cm^3)	Uniaxial Compression Strength (kg/cm^3)	Modulus of Elast icity (kg/cm^3)	Poisson's Ratio	Point Load Test Is$_{50}$ (MPa)	Point Load Test q$_u$ (kg/cm^2)
36.20-36.40	2.57	162.9	41681	0.26	-	-
45.40-45.60	2.55	-	-	-	2.13	521.27
47.00-47.80	2.49	23.00	25641	0.25	-	-

Figure 1. View of flows on the right and left slope slopes at the diversion tunnel entrance portal.

slope reinforcement in open excavations, there was an absence of support in the diversion tunnel exit excavations. These excavations, situated in an ophiolitic unit with weak to very weak rock slopes, remained exposed for an extended period without support, resulting in landslides and erosion triggered by water and rainwater. The diversion tunnel exit portal excavation, conducted in proximity to the body skirt, was observed to be opened without diverting the tunnel itself. This proximity to the body, and potentially within it, suggests a deviation from standard excavation practices. Furthermore, water inflows perpendicular to the diversion tunnel route were identified.

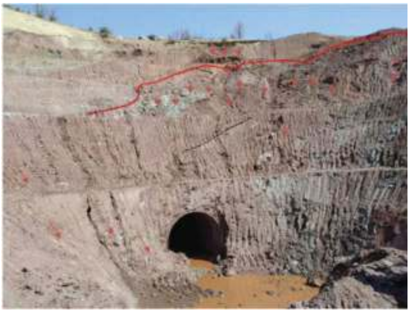

Figure 2. View of the diversion tunnel exit portal and slope failure.

The excavations left exposed formed an altered zone in contact with air and water, lead a sliding, and the diversion tunnel exit was closed (Figure 3).

Figure 3. Diversion outlet, in-situ situation on 01.05.2020.

Figure 4. View from the slides on the hillside at diversion tunnel outlet conduit route.

As can be seen in the following figure, during the February 6, 2023 Kahramanmaraş sequential earthquakes, the first M7.5 magnitude earthquake struck the dam area in 0.1g-0.2g ground acceleration range, while it went up to 0.48g during the second M7.8 magnitude shock. This data was observed at the nearest instrumentation station to the dam site (USGS, 2023).

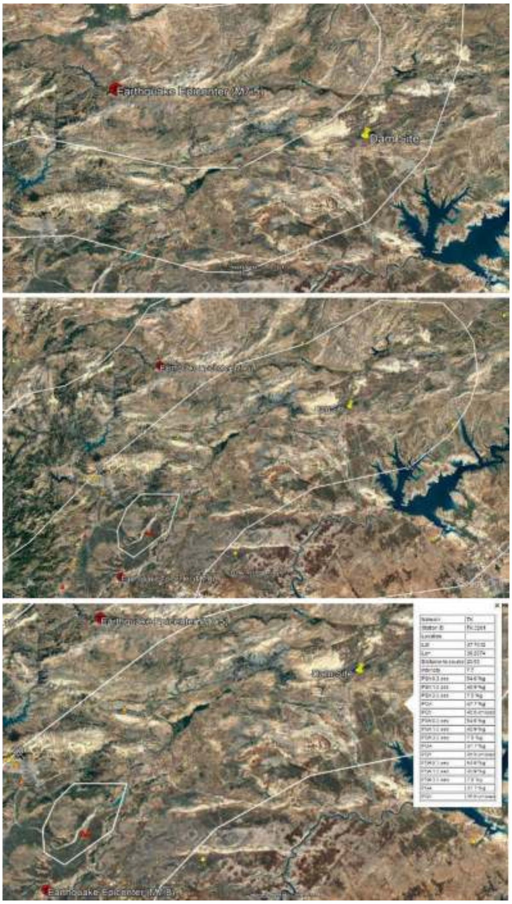

Figure 5. Observed PGA values after M7.5 and M7.8 magnitude earthquakes.

4 SOLUTIONS AND RECOMMENDATIONS

To stabilize the slopes at the diversion tunnel entrance portal, two alternatives were considered. The first involves terracing the slopes at 3H:2V, implementing typical slope support, and incorporating a concrete trapezoidal channel at the base for scour prevention. The existing temporary 1H:1V slopes were part of this alternative. The second alternative proposes a retreat of these slopes, creating a 6.00m base width, constructing a conduit instead of a trapezoidal channel, and covering it with fill before the tunnel entrance. The water intake tower is recommended to be positioned openly on the conduit, away from the portal slope, mitigating potential slope slippage damage.

For the portal excavation, an additional option considers addressing flows at the existing portal location by lowering the excavation slopes and supporting them with a typical support system. In its current state, the portal excavations are at a 1H:1V slope, and flows have occurred. To address this, a design shift to a 3H:2V slope with a 6m high bench and typical support is proposed. The excavation slopes will reach the dam axis and the access road, avoiding the challenges posed by the existing 1H:1V slopes, which are close to the dam plinth line.

The second alternative recommends setting back the temporary 1H:1V slopes on the sides, creating a 6.00m base width, and covering the portal excavation area with fill until the tunnel entrance. The water intake tower is set back 10.00m from the portal to mitigate potential slope slippage risks. The top of the conduit will be backfilled with compacted mineral fill up to the first pallet elevation to form a heel, and the portal slope will be tilted 2H:1V to prevent sliding under the plinth. The excavation slopes are suggested to be arranged with embankment at a 2H:1V slope. Additionally, 1.00m rock filling is recommended to prevent flow and slipping on the embankment, designed in different sections based on the fill load on the conduit.

5 RESULTS AND DISCUSSION

5.1 *Stability analysis*

0.14g ground acceleration (OBE) was used in the seismic (pseudo-static) analyses of slope rehabilitation. For the actual earthquake comparison, the observed PGA of 0.48g was used.

5.1.1 *Inlet*

Geotechnical parameters were determined for the unit in the diversion inlet excavations and slope stability analyses were performed. Necessary alternative studies were carried out to ensure the safety of the slopes and it was aimed to make the slopes safe. Regarding the excavated part of the diversion entrance route, the current situation was mapped and the existing excavation and the structures in the project were processed, and the interaction of the excavations already opened in the field and the body plinth route was evaluated. The following slope stability analyses were performed for the excavations to be carried out at 1H:1V slope gradient. On the ophiolitic complex, which is a weak to very weak rock, a section close to the surface decomposes due to contact with air and water and forms an altered zone. In the analyses, the altered zone formed when the slope surface is left exposed and the situation where the contact of the unit with air and water is cut off with support were also analyzed.

Static and pseudo-static stability analyses are given below for 1H:1V excavation with steel mesh and shotcrete support, where air-water contact on the slope surface is interrupted by weep holes and slope drainage.

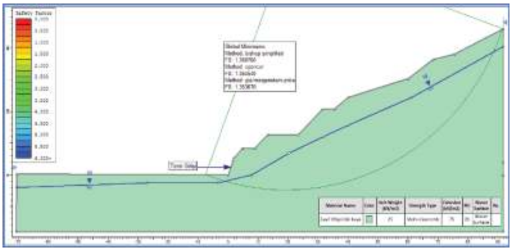

Figure 6. Diversion tunnel inlet 1H:1V supported static stability analysis (FS= 1.35 < 1.5).

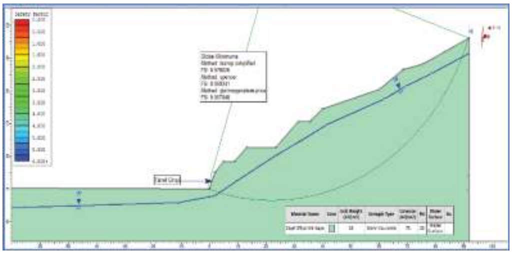

Figure 7. Diversion tunnel entrance 1H:1V supported seismic stability analysis (FS = 0.96 < 1.1).

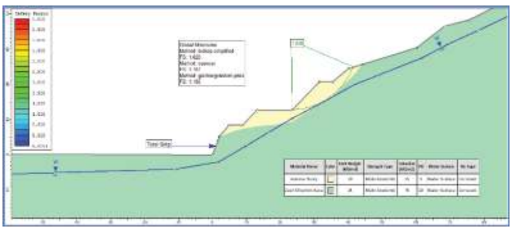

Figure 8. Diversion tunnel entrance 1H:1V unsupported static stability analysis (FS= 1.18 < 1.5).

If the slope is 3H:2V for permanent excavations, the slopes cannot be opened as they reach under the plinth and under the dam body. For this reason, since the portal excavations opened with temporary slope slopes of 1H:1V that do not provide stability, the slope stability will be ensured by constructing a conduit instead of a trapezoidal channel until the tunnel entrance and filling the slopes and conduit with fill and the topography reaching its own slope. Backfill slopes will not be steeper than 2H:1V. It is recommended that 1.00 m of rock fill should be placed on the backfill applied on the slope surface in order to prevent it from collapsing with the current.

Static and pseudo-static stability analyses are given below in case of 2H:1V filling after 1H:1V excavation.

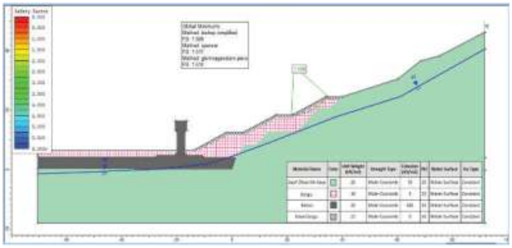

Figure 9. Diversion tunnel inlet conduit section static stability analysis (FS= 1.506 > 1.5).

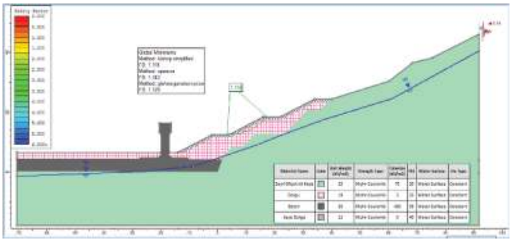

Figure 10. Seismic stability analysis of the diversion tunnel entrance conduit section (FS= 1.118 > 1.1).

It is recommended to apply steel mesh and at least 5cm+5cm shotcrete according to the support type in the project. In the final project, the bolt length is given as 4m, which is not long enough. In this type of soils, the bolts do not work because there is no block, solid rock where the rock bolt will be anchored and the slip surfaces are formed in a wide circle. Due to this reason, it is recommended to lower the slope gradients and reduce the bench heights in terms of stability. In cases where it is not possible to lower the slopes at the entrance section of the diversion (excavations enter into the body), the topography should be brought to its natural slope by passing through a conduit (such as a cut-and-cover tunnel) and backfilling.

The following analysis is not a dam body stability analysis, but an analysis of the interaction between the body and the conduit entrance completed during the construction of the body. According to the height of the body, approximately 4kg/cm^2 load is applied.

Figure 11. Interaction with the body after conduit backfill in static condition (FS=1.54>1.5).

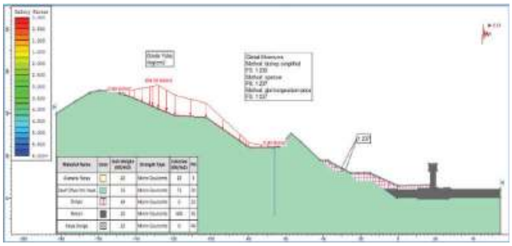

Figure 12. Interaction with the body after conduit backfill for seismic case (FS=1.23>1.1).

Cleaning excavation will be made in the sliding area and it will be covered again with backfill after the conduit. It is recommended that the new slope excavations to be opened by the conduit should be opened with supports and drainage.

The analysis below corresponds to the model in Figure 12, utilizing an actual PGA of 0.48g from the M7.8 magnitude earthquake as the horizontal ground acceleration. Factors of safety below 0.759 are associated with shallow slope failures, and only critical and deep slope surfaces were evaluated, ensuring a minimum factor of safety of 0.759.

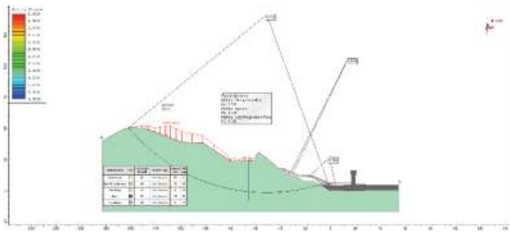

Figure 13. Interaction with the body after conduit backfill for seismic case for 0.48g (FS=0.759<1.0).

5.1.2 *Outlet*

Geotechnical parameters were determined for the diversion outlet excavations, and slope stability analyses were conducted to ensure safety. Mapping the current conditions and evaluating the interaction of the body with existing excavations, particularly those in the field, were part of the assessment. Water flowing perpendicular to the conduit's route will be diverted from upper elevations parallel to the valve chamber access road and released into the stream bed.

Cracks and splits were observed in shaft sections leading to the valve chamber. To preserve the valve room road, the first two slopes from the base were analyzed at a 1H:1V slope, while slopes between the third slope pallet elevation and the valve room access road were analyzed at a 3H:2V slope. Slope stability analyses were conducted for excavations at 1H:1V and 3H:2V slope gradients, considering the altered zone and interruption of the unit's contact with air and water when the slope surface is exposed.

Face portal slope stability analyses were undertaken in two sections—the body and diversion sections—ensuring stability. However, in the interest of brevity, face portal analyses are not included in this paper.

In the analysis performed without support in temporary excavation at the critical section of the diversion outlet, the safety factor was 1.18 due to the effect of the altered zone. As also seen in the field, failures occur from the slope surface (Figure 14).

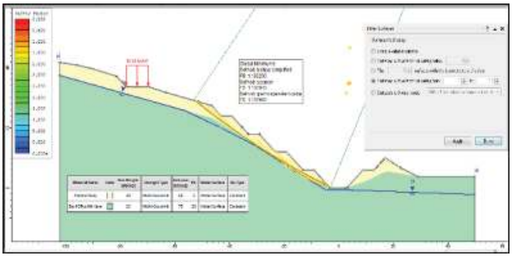

Figure 14. Diversion outlet 1H:1V unsupported static stability analysis (FS=1.18<1.50).

The diversion outlet's critical section underwent analysis with slope reinforcement, utilizing steel mesh and shotcrete during excavations on a 1H:1V slope to obstruct the unit's contact with air and water. It is anticipated that cutting this contact, along with water removal through a drainage system, including head ditches and weep holes in the benches, will prevent the formation of an altered zone. Application of steel mesh, 5cm+5cm shotcrete, and weep holes in the supports was considered. Analysis revealed that the use of short rock bolts did not significantly impact stability, given the wide sliding arc.

Since the safety factor is 1.33 for the first two slope surfaces 1H:1V from the base and 3H:2V for the upper slopes, there will be a stability problem in case of permanent excavation (Figure 15).

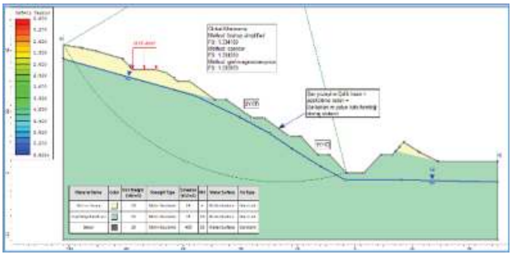

Figure 15. Static stability analysis with diversion outlet 1H:1V support (FS = 1.33 < 1.50).

If filling is done only up to the first bench, stability problems will still persist (Figure 16).

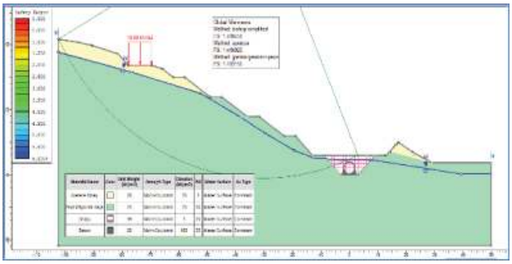

Figure 16. Static stability analysis of backfill up to the first bench at the diversion outlet (FS = 1.41 < 1.50).

The slope heel filling on the slope close to the natural slope of the topography was analyzed below. The case of filling with backfill up to the first two bench elevations and supporting the slope surfaces with 2H:1V slope protection embankment is analyzed. In the slope protection embankment, it is recommended to construct a slope protection cover with 1.00m rock fill against surface runoff.

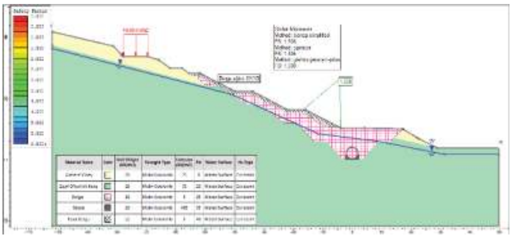

Figure 17. Static stability analysis of embankment up to the first two benches of the diversion outlet (FS = 1.508 > 1.50).

Stability problems will be eliminated if the first two benches are backfilled. The topography approximately reaches its natural slope. Embankments are analyzed as 2H:1V. Embankments should not be constructed at steeper slopes.

Seismic analysis of the slope surfaces in case of 2H:1V embankment and backfilling up to the first two benches is given below.

Figure 18. Seismic condition stability analysis of the embankment up to the first two benches of the diversion outlet (FS = 1.14>1.1).

In accordance with the observed PGA of 0.48g, comparable outcomes to those at the inlet portal were noted, with all factors of safety registering below 1, some marginally so. However, these results are not presented here for the sake of conciseness.

6 CONCLUSIONS

Proposed support by terracing and granular fill is working as seen during site visits, even after the major earthquake sequence in the vicinity of the dam site. This method can be used as a cost-effective method in tunnel projects with similar landslide problems.

On the other hand, the fact that the slopes are failing in the analysis but not in reality might be explained by the following reasons:

– The peak ground acceleration value obtained from the earthquake records is very instantaneous and may not be fully representative of the earthquake on the given site conditions,
– Being conservative when selecting parameters,
– The extent to which the topographic model reflects reality,
– Selection of analysis type and earthquake acceleration,
– Material model and stress-strain behavior.

In addition, the possibility of landslides of invisible size and velocity during site visits should not be ignored.

REFERENCES

Bieniawski, Z. T. (1989). Engineering Rock Mass Classification Mining and Mineral Resources Research Institute. New York, A Willey-Interscience Publication.

Day R.W. (2006). Foundation engineering handbook. McGraw-Hill Companies.

Duncan, J. M., & Wright, S. G. (2005). Soil strength and slope stability. John Wiley & Sons.

Fatkhiandari, I. A., Indrawan, I. G. B., & Karnawati, D. (2020b). NUMERICAL EVALUATION OF TUNNEL PORTAL SLOPE STABILITY AT BAGONG DAM SITE, EAST JAVA, INDONESIA. Journal of Applied Geology. https://doi.org/10.22146/jag.57044

Hammouri N.A., Malkawi A.I.H., & Yamin M.M.A. (2008). Pseudo-static slope stability analysis using a modified dynamic coefficient. Bulletin of Engineering Geology and Environment 67:471–478.

Huda, N., Indrawan, I. G. B., & Wilopo, W. (2022). Stability Evaluation of Diversion Tunnel Portal Slopes at Lau Simeme Dam Site, Indonesia, using Limit Equilibrium Method. Journal of Applied Geology, 7(1), 41. https://doi.org/10.22146/jag.58069

Naseer S., & Evans R. (2020). Stability analysis of slopes using limit equilibrium and finite element methods. In 2nd Conference on Sustainability in Civil Engineering 2020 (pp. 1–8). Department of Civil Engineering Capital University of Science and Technology.

Oktarina, I. M. A., Pramumijoyo, S., & Indrawan, I. G. B. (2023). Slope stability analysis at outlet portal of tunnel No. 8 Jakarta-Bandung high-speed railway, Indonesia. Nucleation and Atmospheric Aerosols. https://doi.org/10.1063/5.0130144

Popescu, M. (2001). A suggested method for reporting landslide remedial measures. Bulletin of Engineering Geology and the Environment, 60(1), 69–74. https://doi.org/10.1007/s100640000084

Sengkey, C. I., Amijaya, D. H., & Indrawan, I. G. B. (2023). Slope stability analyses of the diversion tunnel portals at Manikin Dam, Indonesia, using limit equilibrium and finite element methods. Nucleation and Atmospheric Aerosols. https://doi.org/10.1063/5.0132911

U.S. Geological Survey, 2023, Mw 7.5 - Elbistan earthquake, Kahramanmaras earthquake sequence at https://earthquake.usgs.gov/earthquakes/eventpage/us6000jlqa/executive (Accessed September 18, 2023).

U.S. Geological Survey, 2023, Mw 7.8 - Pazarcik earthquake, Kahramanmaras earthquake sequence at https://earthquake.usgs.gov/earthquakes/eventpage/us6000jllz/executive (Accessed September 18, 2023).

United States Geological Survey (2023). The 2023 Kahramanmaraş, Turkey Earthquake Sequence. Retrieved from https://earthquake.usgs.gov/storymap/index-turkey2023.html (Accessed September 20, 2023).

Wang I.-T. (2019). Stability analysis for tunnel portal slope with weak rock mass by numerical simulation method: A case study in Taiwan. Infrastructures 4(4):70.

New Trends in Determining Soil Properties

Avrupa Bilim ve Teknoloji Dergisi
Özel Sayı 28, S. 998-1007, Kasım 2021
© Telif hakkı EJOSAT'a aittir
Araştırma Makalesi

www.ejosat.com ISSN:2148-2683

European Journal of Science and Technology
Special Issue 28, pp. 998-1007, November 2021
Copyright © 2021 EJOSAT
Research Article

Zemin Özelliklerinin Belirlenmesinde Yeni Trendler

Asena Karslioğlu[1*], Ahmet Ali Mert[2], Mehmet İnanç Onur[3]

[1*]Eskişehir Teknik Üniversitesi, Lisansüstü Eğitim Enstitüsü, İnşaat Mühendisliği, Eskişehir, Türkiye, (ORCID:0000-0001-5178-4069), asenakarslioglu@eskisehir.edu.tr
[2] Eskişehir Teknik Üniversitesi, Lisansüstü Eğitim Enstitüsü, İnşaat Mühendisliği, Eskişehir, Türkiye, (ORCID:0000-0001-9205-488X), ahmetalimert@utexas.edu
[3] Eskişehir Teknik Üniversitesi, Lisansüstü Eğitim Enstitüsü, İnşaat Mühendisliği, Eskişehir, Türkiye, (ORCID:0000-0002-2421-4471), mionur@eskisehir.edu.tr

(1st International Conference on Applied Engineering and Natural Sciences ICAENS 2021, November 1-3, 2021)

(**DOI:** 10.31590/ejosat.1012397)

ATIF/REFERENCE: Karslıoğlu, A., Mert, A. A. & Onur, M.İ (2021). Zemin Özelliklerinin Belirlenmesinde Yeni Trendler. *European Journal of Science and Technology*, (28), 998-1007.

Öz

Zemin özelliklerinin belirlenmesi ve zemin davranışının açıklanması geoteknik mühendisliğinin temellerini oluşturmaktadır. Zemin davranışına ilişkin teoriler 1900'lü yıllarda geliştirilmeye başlanmış, günümüzde ise yeni nesil yöntemler ile yeni bir aşamaya geçilmiştir. Yeni nesil nümerik metotlar ile en karmaşık koşullar altında zemin davranışı modellenebilmektedir. Zemin özelliklerinin belirlenmesi ve zemin davranışının açıklanması genel olarak deneysel çalışmalar ile bu çalışmalardan elde edilen verilen ampirik teorilerde kullanılması olarak yürümekteyken, günümüzde yapay sinir ağları, bulanık mantık gibi uzman sistemler ile mevcut deneysel ekipmanların modifikasyonu ve geleneksel deney metodolojilerinin geliştirilmesi sıkça kullanılmaya başlanmıştır. Bu çalışmada geoteknik mühendisliğinde zemin özelliklerinin belirlenmesi ve zemin davranışının açıklanmasına yönelik yeni nesil yöntemlerin tanıtılması amaçlanmıştır.

Anahtar Kelimeler: Zemin Mekaniği, Geoteknik mühendisliği, Yeni Trendler.

New Trends in Determining Soil Properties

Abstract

Determination of soil properties and explanation of soil behavior are the basis of geotechnical engineering. Theories on soil behavior are developed from the 1900s, and today, a new phase has been started with new generation methods. Soil behavior can be modeled under the most complex conditions with the new generation numerical methods. While the determination of soil properties and the explanation of soil behavior are generally used in experimental studies and empirical theories obtained from these studies, nowadays, expert systems such as artificial neural networks, fuzzy logic, modification of existing experimental equipment and development of traditional experimental methodologies are frequently used. In this study, it is aimed to introduce new generation methods for determining soil properties and explaining soil behavior in geotechnical engineering.

Keywords: Soil mechanics, Geotechnical engineering, New Trends.

[*] Corresponding Author: asenakarslioglu@eskisehir.edu.tr

1. Giriş

Zemin mekaniği ilkelerinin çeşitli yapılar için temellerin tasarımı ve inşasına uygulanması, temel mühendisliği olarak bilinmektedir. Geoteknik mühendisliğinin hem zemin mekaniğini hem de temel mühendisliğini içerdiği düşünülebilir. Aslında Terzhagi'ye göre zemin mekaniği ve temel mühendisliği arasında belirgin bir sınır çizgisi çizmek zordur; geoteknik mühendisliği, temel mühendisliğinin bittiği yerde başlar [1].

Geoteknik mühendisliğinde zemin davranışını modelleyen teoriler 1900'lü yıllarda geliştirilmeye başlanmış, günümüzde teorik zemin mekaniği ve temel mühendisliği yeterli olgunluğa ulaşmıştır. Zemin davranışını modelleyen nümerik metotlar ile en karmaşık yapı geometrisi ve zemin koşullarında yapı-zemin ilişkisini analiz edebilecek seviyeye ulaşılmıştır. Gerek teorik yaklaşımları gerekse nümerik metotları uygulayabilmek için en önemli aşama zeminin doğru modellenmesi, diğer bir deyişle zemin davranışını yansıtacak geoteknik parametrelerin gerçekçi olarak belirlenebilmesidir [2].

Geoteknik mühendisliği deneysel çalışmalar, teoriler ve uygulamalar olarak yürümekteyken, artık günümüzde yeni nesil metotların oluşmasıyla yeni bir safhaya geçmiştir. Bu çalışmada kısaca bu yeni nesil yöntemlerin tanıtılması ve tartışılması amaçlanmıştır.

2. Literatür

2.1. Uzman Sistemler Kullanarak Zemin Özelliklerinin Belirlenmesi

Son yıllarda, zemin özelliklerinin tahmini ve zemin davranışının modellenmesi için makine öğrenmesi veya yapay zekâ yöntemleri yaygın olarak uygulanmaktadır. Uzman sistemler kullanarak yapılan çalışmalar bu bölümde incelenmektedir.

Yapay Sinir Ağlarının (YSA) inşaat mühendisliğinde geoteknik dâhil uygulamaları artmıştır. Işık ve Özden (2013) hem kaba hem de ince taneli zeminlerin sıkıştırma parametrelerini tahmin etmek için YSA tahmin modellerini kullanmıştır. Standart Proctor enerjisinde toplam 200 zemin karışımı hazırlanıp sıkıştırılmıştır. Sıkıştırma parametreleri, farklı girdi veri setleri kullanılarak YSA modelleri aracılığıyla tahmin edilmiştir. YSA tahmin modelleri, indeks özelliklerinden hangilerinin sıkıştırma parametreleriyle iyi ilişkili olduğunu bulmak için geliştirilmiştir. Geçiş ince içerik oranı (TFR), zemin indeksi parametrelerine ek olarak yeni bir girdi parametresi olarak tanımlanmıştır. Optimum su içeriği (Wopt) ve maksimum kuru birim ağırlık tahmininin, temel zemin indeksi parametreleri kullanılarak yüksek doğrulukla yapılabileceği gösterilmiştir. Bununla birlikte, istenen tahmin doğruluğu ve genelleme yeteneği, verilerin uygun şekilde normalleştirilmesi ve bölünmesiyle elde edilebilmektedir. TFR parametresinin kullanılması YSA modellerinin Wopt tahminindeki performansını artırmaktadır [3].

Momeni vd. (2014) kazıkların taşıma kapasitesini tahmin etmek için genetik algoritma (GA) optimizasyon tekniği ile geliştirilmiş YSA tabanlı bir tahmin modeli geliştirmiştir. Modelin oluşturulması için gerekli veri setini sağlamak amacıyla prekast beton kazıklarda 50 dinamik yük testi yapılmıştır. Kazık geometrik özellikleri, kazık seti, çekiç ağırlığı ve düşme yüksekliği ağ girdileri olarak ayarlanmış ve kazık nihai taşıma kapasitesi, GA tabanlı YSA modelinin çıktısı olarak ayarlanmıştır. Sonuçta, GA tabanlı YSA modelinin kazık taşıma kapasitesinin tahmin edilmesinde geleneksel YSA modelinden daha iyi performans gösterdiği bulunmuştur [4].

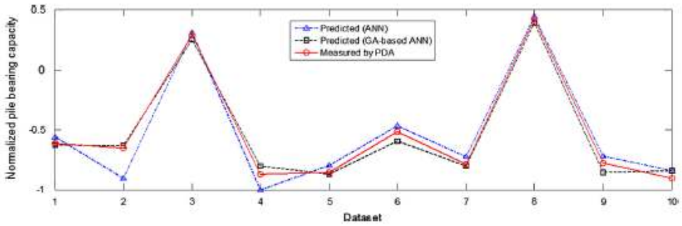

Şekil 1. Kazık taşıma kapasitesinin GA tabanlı YSA ve YSA tahmin modellerinin performansı [4]

Diaz vd. (2018) bir temelin altındaki eğimli ana kaya tarafından sınırlandırılan sonlu bir elastik yarı alanın etkisini dikkate alan etki faktörünün (Ia) belirlenmesini iyileştirmek için sinir ağlarını kullanmaktadır. YSA'nın eğimli bir rijit tabaka ile sonlu bir yarı uzayda oturan temellerin oturmasını doğru bir şekilde tahmin edebildiği doğrulanmıştır. Ayrıca YSA yönteminin geleneksel analitik regresyon yöntemlerinden daha iyi sonuçlar sağlayabileceğini de ortaya koymuştur [5].

Tran vd. (2018) zemin karakterizasyonlarındaki varyasyonları gerçekleştirmek için önerilen bir prosedür geliştirmiştir. Sabit zemin özellikleri ve profili kullanmak yerine, girdi verileri olarak sönümleme (MRD) eğrilerinin belirsizliklerini, katman kalınlığını ve kayma dalgası hızını (Vs) kullanmaktadır. Yapılan analizlerin sonuçları, doğrusal olmayan zemin özelliklerindeki değişkenliklerin medyan yüzey tepki spektrumu ve yüzey hareketlerinin büyütme spektrumu üzerinde önemli bir etkiye sahip olduğunu göstermektedir [6].

Öztoprak vd. (2018) üç boyutlu sonlu farklar kodu FLAC3D'de benimsenen sertliğe dayalı bir yaklaşım aracılığıyla presiyometre testinin tam eğrisini yakalamak için sayısal bir metodoloji önermektedir. Bunu sağlamak için, Mohr-Coulomb zemin modelinin pik dayanımından önce geleneksel doğrusal elastik modelin yerini almak üzere yeni bir hiperbolik model kullanılmış ve kayma modülünün güncellenmesi düşünülmüştür. Sunulan modelleme yaklaşımı ve uygulanan kurucu model etkileyici bir şekilde başarılıdır. Kumları karakterize etmek için tüm parametrelerin elde edilmesini sağlar ve geoteknik yapıların çoğunu modellemek için umut verici görünmektedir. Önerilen yaklaşımı uygulamak için en az iki döngü gereklidir. Daha fazla döngü, daha iyi zemin karakterizasyonu belirlemektedir [7].

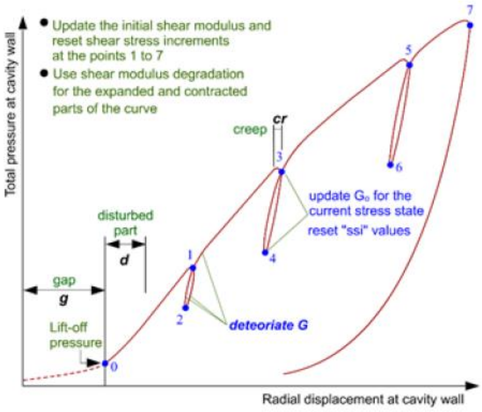

(a) FLAC3D'de modelleme adımlarının sunumu

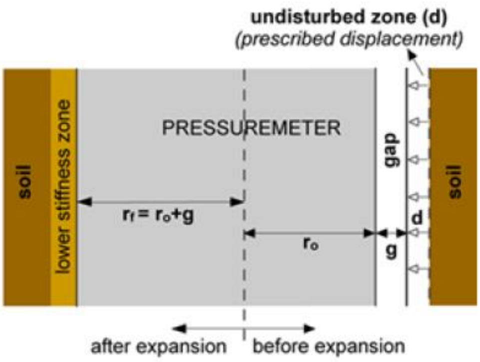

(b) Parametrelerin tanımlanması

Şekil 2. Presiyometre testinin modellenmesi [7]

Zeminin kayma mukavemeti, geoteknik yapıların tasarım ve denetiminde kullanılan önemli bir mühendislik parametresidir. Pham vd. (2018) dört makine öğrenme yönteminin performansını araştırmayı ve karşılaştırmayı amaçlamıştır. Parçacık Sürüsü Optimizasyonu - Uyarlanabilir Ağ tabanlı Bulanık Çıkarım Sistemi (PANFIS), Genetik Algoritma - Uyarlanabilir Ağ Tabanlı Bulanık Çıkarım Sistemi (GANFIS), Destek Vektör Regresyonu (SVR) ve YSA yumuşak zeminlerin kayma dayanımını tahmin etmek için kullanılmıştır. Bu amaçla, modellerin oluşturulması ve doğrulanması için eğitim ve test veri setlerinin oluşturulması için 188 plastik killi zemin örneği kullanılmıştır. Dört modelden PANFIS'in yumuşak zeminlerin mukavemetini tahmin etmek için umut verici bir teknik gösterdiği sonucuna varılabilir [8].

Zemin sınıflandırması, yük altında benzer mühendislik davranışı sergileyecek ortak özelliklere göre zeminleri kategorilere ayırmanın bir yoludur. Ayrıca, temel tasarımından önce gerçekleştirilmesi gereken önemli, maliyetli ve zaman alıcı bir süreçtir. Reale vd. (2018), ESCS (Avrupa Zemim Sınıflandırma Sistemi) ve USCS (Birleşik Zemin Sınıflandırma Sistemi) zemin sınıflandırmalarını otomatik olarak belirlemek için YSA uygulamasını incelemektedir. YSA, zemindeki ince parçacıkların yüzdesini ve LL ile ona karşılık gelen plastisite indeksini tahmin ederek zeminin kıvamını belirlemek için geliştirilmiştir. Bu yaklaşım, hem ESCS hem de USCS zeminlerin yaklaşık % 90'ını doğru bir şekilde sınıflandırmıştır. YSA kullanımı hem zamandan hem de paradan tasarruf edilerek inşaat sürecini kolaylaştırmaktadır [9].

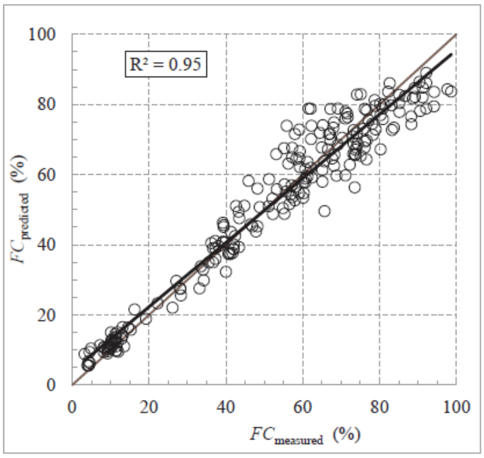

(a) İncelik Yüzdesi

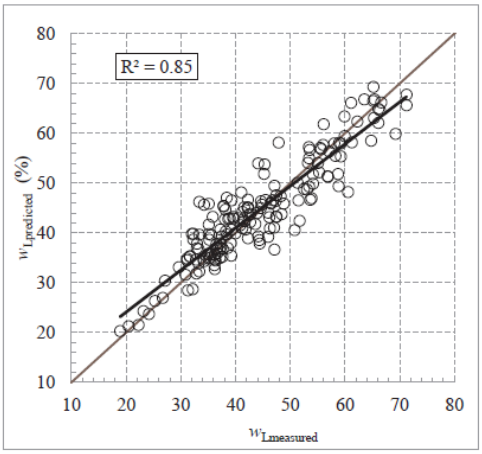

(b) Likit Limit

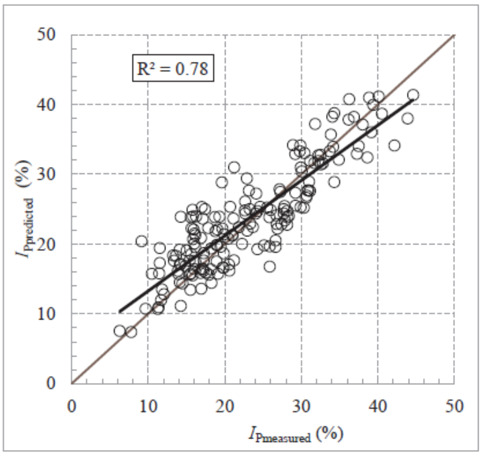

(c) Plastisite İndeksi

Şekil 3. YSA ve laboratuvarda ölçümler [9]

Sihag (2018) zeminin (Ku) doymamış hidrolik iletkenliğini tahmin etmek için bulanık mantık (FL) ve YSA tabanlı modeller geliştirmiştir. Rastgele seçilen modellemede eğitim için verilerin %70'i, test için verilerin %30'u kullanılmıştır. Çalışmadan, her iki yaklaşımın da bu veri setiyle iyi çalıştığı sonucuna varılmıştır. Performans değerlendirme parametrelerinin karşılaştırılmasından YSA yaklaşımının FL yaklaşımlarına göre iyi çalıştığı görülmüştür [10].

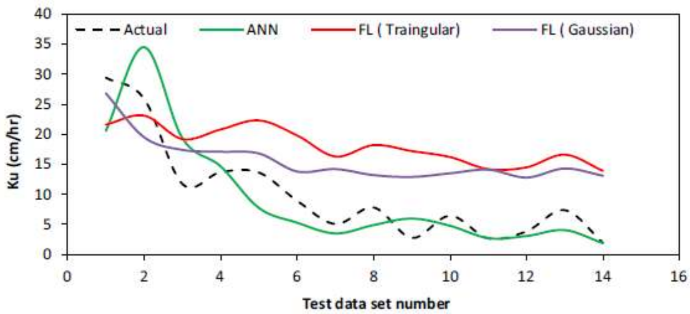

Şekil 4. Ku'nun gerçek değerlerine kıyasla farklı yaklaşımlar kullanarak Ku değerlerinde değişim [10]

Azadmard vd. (2020) neredeyse doymuş zemin hidrolik özelliklerinin tahmini için çoklu doğrusal regresyon (MLR) ve hibrit GA yönteminin YSA ile etkinliğini karşılaştırmak için bir çalışma yapmıştır. MLR analizinin sonuçları, bu yöntemin çalışma alanında neredeyse doymuş zemin hidrolik özelliklerini tahmin etme potansiyeline sahip olduğunu göstermiştir. MLR modellerine kıyasla GA-YSA modellerinin daha yüksek performansı, zeminin fiziksel ve kimyasal özellikleri ile hidrolik özellikler arasında doğrusal olmayan ilişkilerin varlığını doğrulamıştır [11].

Literatürde, Bender elemanı (BE) test simülasyonunun sayısal analizine daha az odaklanılmıştır. Ingale vd. (2020) yaptığı çalışmada sayısal simülasyondan ve deneylerden elde edilen sonuçların analiz edilmesi ve karşılaştırılması yapılmıştır. Bu amaçla, USCS'ye göre altı farklı sınıflandırılmış zemin numuneleri seçilmiş ve farklı sıkıştırma durumlarına göre kalıplanmıştır. BE testleri sonucunda kayma dalgası hızı (Vs) deneysel olarak belirlenmiştir. Ayrıca, sonlu elemanlar yöntemine (FEM) dayalı sayısal bir kod AbaqusTM yardımı ile sayısal simülasyon yapılmıştır. Bu araştırmadaki FE analizinin amacı, numune geometrisinin, sınır koşullarının ve giriş frekansının laboratuvar BE sonuçlarına kıyasla farklı malzeme modelleri üzerindeki etkisini araştırarak doğru bir yaklaşıma ulaşmaktır. FE analizi, belirli bir frekansın ötesinde deneysel olarak elde edilenle makul ölçüde aynı S-dalgası hızlarını vermektedir. Dolayısıyla, FE modelinin BE testini yeniden üretebildiği söylenebilmektedir [12].

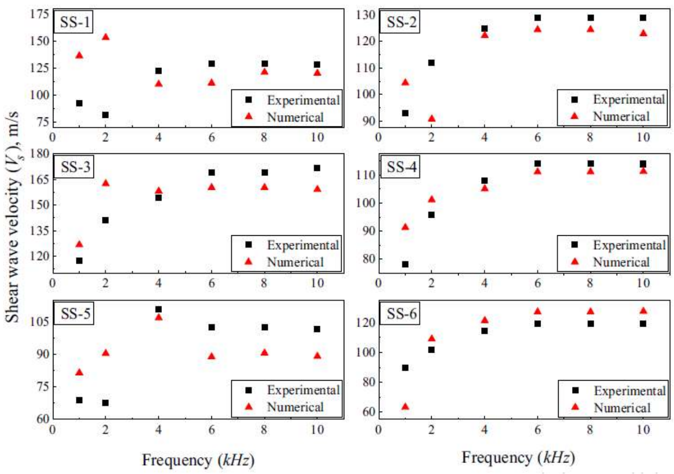

Şekil 5. Farklı zemin örnekleri için giriş frekansı ile kayma dalgası hızındaki değişimi [12]

Adab vd. (2020) yaptıkları çalışmada, pratikte farklı arazi kullanımına göre yüzeye yakın (5 cm) zemin nemini tahmin etmek için dört farklı hızlı doğrusal olmayan veri odaklı model oluşturmuştur. Landsat 8'in optik ve termal sensörleri tarafından zemin nemi geri kazanımı için rastgele orman (RF), destek vektör makinesi (SVM), YSA ve elastik ağ regresyon (EN) algoritmaları uygulanmıştır. İstatistiksel karşılaştırmalar, RF yönteminin, farklı arazi kullanım türleri tarafından kapsanan zemin nemini ölçmek için en yüksek Nash-Sutcliffe verimlilik değerini (0.73) sağladığını göstermektedir. Modellemelerden elde edilen sonuçlar, saha verilerinden elde edilen ölçümlerle karşılaştırılmış ve RF modelinin, zemin nem tahmini için diğer üç yöntemden daha iyi performans gösterdiği belirtilmiştir [13].

Zeminin birim ağırlığının (BA) tahmini laboratuvar yöntemleri kullanılarak gerçekleştirilir. Özellikle BA'nın organik zeminlerde elde edilmesi son derece zor, zaman alıcı ve pahalı olan, örselenmemiş yapılara sahip numuneler şeklinde yüksek kaliteli araştırma malzemesi gerektirmektedir. Straz ve Borowiec (2020) makalede, organik zeminlerin birim ağırlığını tahmin etmek için YSA kullanmayı önermiştir. Alt zeminin ilk tanınması mekanik bir koni penetrasyon testi (CPTM) kullanılarak gerçekleştirilmiştir. Standart çok katmanlı geri yayılım ağları, iki ana değişkene (organik içerik LOIT ve doğal su içeriği w) dayalı olarak BA tahmin etmek için kullanılmıştır. Uygulanan modelin, standart regresyon yöntemleriyle karşılaştırılabilir güvenilir tahmin sonuçları sağladığı belirtilmiştir [14].

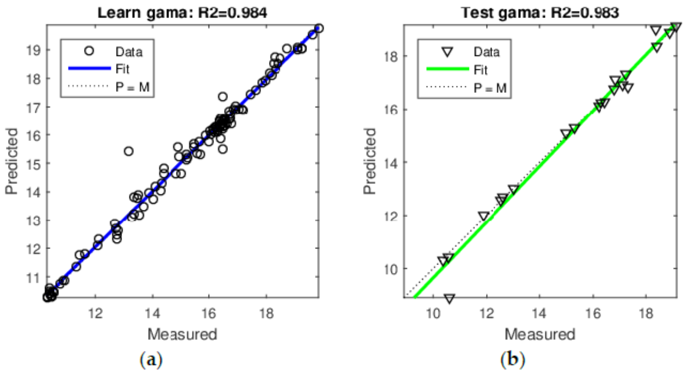

Şekil 6. Zemin BA'nın YSA tahmini (LOIT, w): (a) eğitim verileri ve (b) test verileri [14]

Pham vd. (2020) zeminin drenajsız kesme dayanımını tahmin etmek için rastgele orman (RF) ve parçacık sürü optimizasyon (PSO) modellerinin bir kombinasyonu olan yeni bir hibrit makine öğrenmesi olan RF-PSO modelini önermiştir. Bu model zeminin kil içeriğine, nem içeriğine, özgül ağırlığa, boşluk oranına, likit limite ve plastik limite dayalı olarak zeminin kesme dayanımını tahmin etmek için kullanılmıştır. Önerilen hibrit modelin (RF-PSO) zeminin kesme dayanımı tahmininde yüksek bir doğruluk performansı (R = 0.89) elde ettiği bulunmuştur [15].

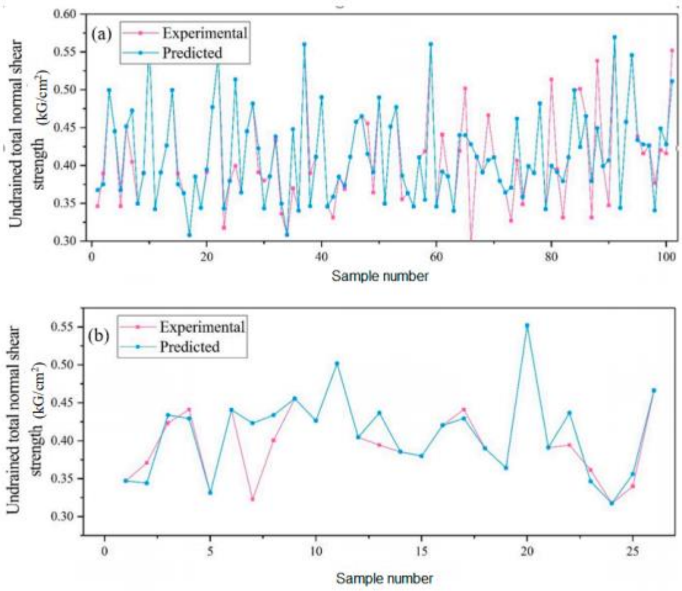

Şekil 7. Deneysel ve tahmin edilen kesme dayanımı değerleri: (a) eğitim seti, (b) test seti [15]

2.2. Zemin Özelliklerinin Belirlenmesinde Yeni Nesil Deney Sistemlerinin Kullanılması

Zemin özelliklerinin ve zemin davranışının belirlenmesi için geçmişten beri çeşitli deney aletleri tasarlanarak kullanılmıştır. Geleneksel deney aletlerinin çeşitli modifikasyonlarla geliştirilerek kullanımı veya yeni üretilen deney sistemleri bu bölümde incelenmektedir.

Kayabalı vd. (2016) likit limit (LL) ve plastik limit (PL) değerlerini tek bir cihazda birleştirmek için, Çamur Baskı Yöntemi (Mud Press Method = MPM) adı verilen ekipman geliştirmiştir. MPM'den elde edilen bulguları doğrulamak için geleneksel yöntemler kullanılmıştır. Toplamda LL = 28 - 166 arasında değişen 275 zemin örneği hazırlanıp incelenmiştir. MPM yönteminden elde edilen log(a) ve 1/b parametreleri, geleneksel yöntemlerin sonuçlarıyla ilişkilendirilmiştir. Yeni yaklaşımın, 1 saat gibi kısa sürede gereken verilerin elde edilmesi ve operatör bağımlılığını en aza indirmesi gibi çeşitli açılardan geleneksel yöntemlerden üstün olduğu belirtilmiştir [16].

Şekil 8. Çamur Baskı Makinesi (Mud Press Machine) [16]

Superpave yoğurmalı sıkıştırıcı (SGS), diğer sıkıştırma yöntemlerine göre daha etkili, doğru ve tekrarlanabilir sonuçlar göstermektedir. Bazı araştırmacılar, SGS'nin saha koşullarına daha benzer olduğunu öne sürmüştür. Dantas vd. (2016) maksimum kuru yoğunluklar karşılaştırılarak Proctor ve SGS yöntemi arasında bir benzerliğe ulaşmaya çalışmıştır. Killi zemin, Brezilya standardına (NBR 7182/1986) göre üç farklı enerjide Proctor testine tabi tutulmuştur. SGS ekipmanı aynı zamanda zemini sıkıştırmak için de kullanılabilir. Ayrıca, SGS'deki prosedür umut vericidir, çünkü optimum parametreler normal ve orta Proctor enerjisine eşdeğer veya daha üstündür [17].

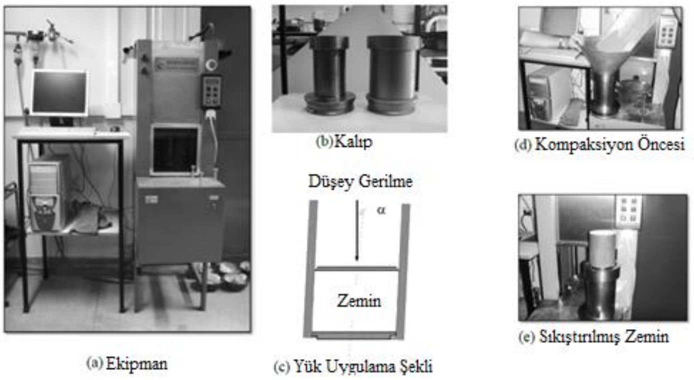

Şekil 9. Superpave yoğurmalı sıkıştırıcıda sıkıştırma şeması [17]

Zhao vd. (2018) beyaz ve siyah renklerde silis kumu partiküllerinin bir karışımı ile hazırlanan numunelerin yerel deformasyon özelliklerini doğrudan ve dolaylı drenajsız üç eksenli testte değerlendirmek için, şeffaf bir membran kullanılarak Partikül Görüntü Velosimetrisine dayalı bir prosedür geliştirilmiştir. Doğrudan ve dolaylı arasındaki karşılaştırma, bitişik kum parçacığına göre membran üzerindeki bir noktanın konumunun sıvılaşmanın başlamasından sonra sabit kalmadığını ortaya koymuştur. Dikey kaymanın değeri, aşırı gözenek suyu basıncı, özellikle büyük bir eksenel gerilme koşulu altında, başlangıçtaki etkili gerilime eşit olduğunda önemli ölçüde artmıştır [18].

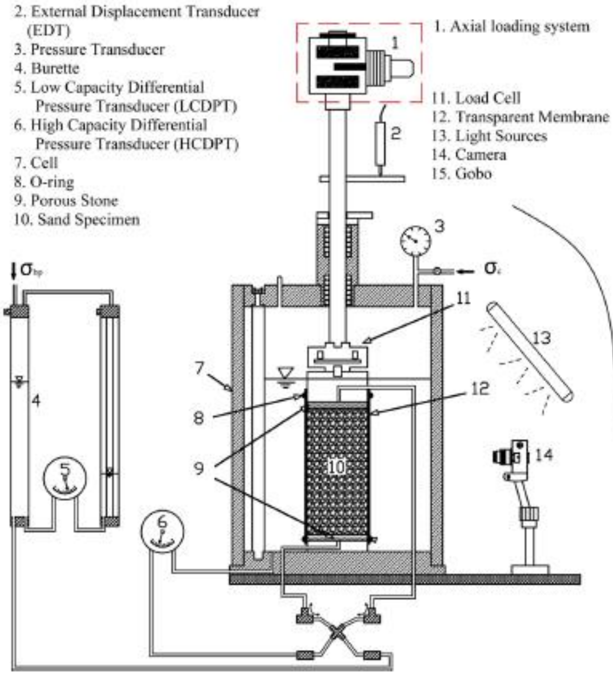

Şekil 10. Üç eksenli deney düzeneğinin şematik diyagramı [18]

Lu vd. (2019), hidrolik iletkenlik (K) ile elektriksel iletkenlik (EC) arasındaki nicel ilişkiyi kurarak, zemin K'sını tahmin etmek için uygun bir yaklaşım sağlamaya çalışmıştır. Deneysel çalışma, sayısal analiz ve model karşılaştırması yapılmıştır. Deneylerde üç faktörün (partikül boyutu, zemin sıkıştırma derecesi ve sıvı (NaCl çözeltisi) konsantrasyonu) K üzerindeki etkileri test edilmiştir. Karşılaştırma EC'yi kullanarak hızlı bir K tahmini sağlayan modellerin, klasik tane boyutu tabanlı formüllerin çoğundan daha iyi performans gösterdiğini göstermiştir [19].

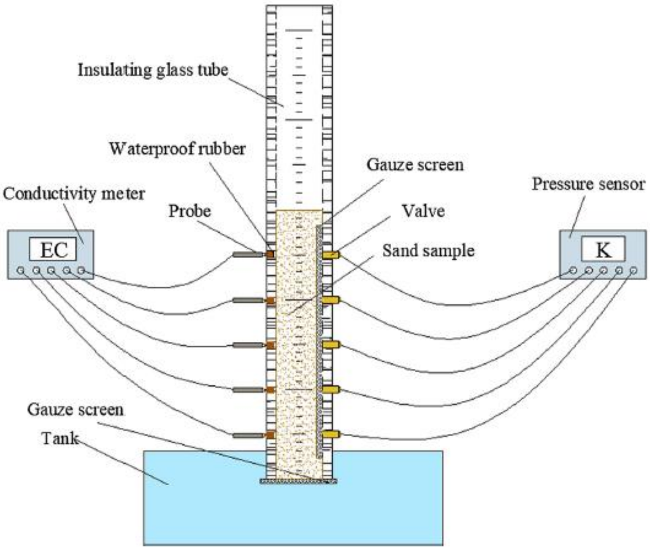

Şekil 11. Zemin hidrolik iletkenliğini ölçmek için tasarlanmış cihaz [19]

Alkayış (2019) yaptığı çalışmada zemin problemleri üzerinde deneyler yapabilmek için laboratuvar ölçekli geoteknik santrifüj deney aleti geliştirmiştir. Deney aleti, bir döndürme kolunun ucundaki model zeminini döndürerek zeminin kendi ağırlık gerilmeleri oluşturulması üzerinde ortaya çıkmıştır. Bu deney sistemi ile tanımlanan ölçek faktörlerine göre küçük modellerin gerçek modelleri büyük ölçüde temsil edildiği vurgulanmaktadır. Deney aleti ile konsolidasyon süreci incelenmiş olup, sistemin 1-D ödometre sonuçlarından elde edilen sonuçların, model üzerindeki teorik konsolidasyon süreci ile Santrifüj konsolidasyon uygunluğu kontrol edilmiştir. Sonuç olarak deney sisteminin konsolidasyon sürecine uygunluğu deney aletinin kalibrasyonu için yeterli görülmüştür. Ayrıca rijit temel altındaki tek ve tabakalı zeminlerin oturma davranışı incelenmiş ve literatür ile karşılaştırılmıştır [20].

Şekil 12. Laboratuvar Ölçekli Geoteknik Santrifüj [20]

Kucerik vd. (2020) laboratuvar koşullarında termogravimetri kullanılarak zemin özelliklerini belirlenmeyi amaçlamıştır. Sonuç olarak, geoteknikte termogravimetri yaklaşımlarının rutin uygulaması için, termogravimetri verileri ve zemin özellikleri arasındaki ilişkileri modellerken teşhis sıcaklıklarındaki olası değişiklikleri hesaba katan bir bağıl nem parametresinin dâhil edilmesi gerektiğini göstermiştir [21].

Kazık bütünlüğünün ultrasonik izlenmesi, sensörler kullanılarak kazık gövdesinde uyarılan ve kaydedilen elastik dalgaların parametrelerinin analizine dayanmaktadır. Lozovsky vd. (2020) COMSOL Multiphysics yazılımında ultrasonik verilerin yorumlanmasına yönelik yaklaşımları açıklığa kavuşturmak için elastik dalgaların yayılmasının sayısal simülasyonu gerçekleştirmiştir. Ultrasonik dalgaların yayılma hızı değerlerinin kazığın dayanım değerlerine çevrilmesinin yanlış olduğu sonucuna varılmıştır [22].

Yıldız vd. (2018), bitki kökü içeren (root-permeated) zeminlerde kesme davranışını belirlemek için yeni oluşturulmuş büyük ölçekli meyilli direkt kesme aparatı (ILDSA) kullanarak, köklerin kuru ağırlığı ile pik gerilim oranı ve azami genleşme açısı ile boşluk oranı ilişkilerinin incelenmesi sonucu kök içeren zemin davranışını araştırmıştır. Köklerin karmaşık yapısı ve zemin davranışının farklı etkenlerden etkilenmesi nedeniyle, basit bir değerlendirme yapmanın zorluğu nedeniyle, en azından laboratuvar ortamında, kök varlığı ve genleşme davranışını dikkate alan bu birleşik yaklaşımın, kök güçlendirmesi etkilerinin miktarının belirlenmesinde daha gerçekçi sonuçlar doğuracağı açıklanmıştır [23].

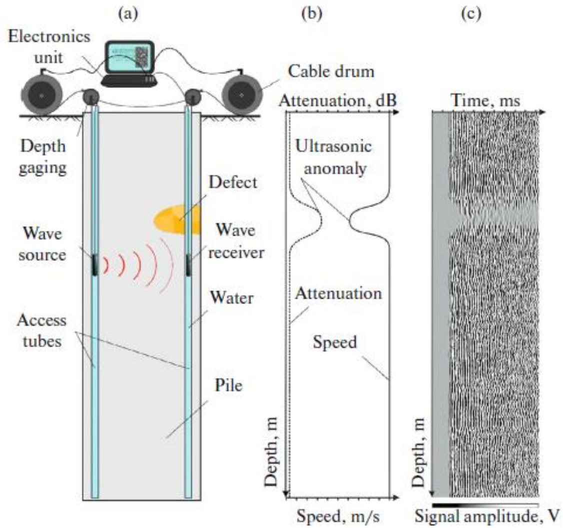

Şekil 13. Ultrasonik kazık bütünlük testi: (a) test tasarımı, (b) yayılma hızı ve ultrasonik dalgaların zayıflaması grafikleri; (c) ölçüm profiline kaydedilen tüm sinyallerden oluşan sismogram [22]

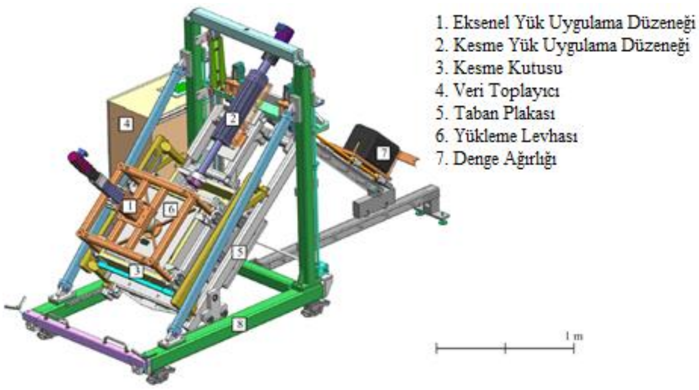

Şekil 14. Büyük Ölçekli Meyilli Direkt Kesme Aparatının (ILDSA) Üç Boyutlu Çizimi [23]

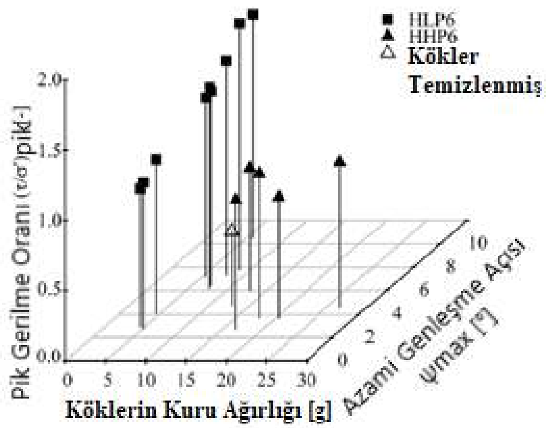

Şekil 15. Tüm Deneyler için Üç Boyutlu Pik Gerilme Oranı, Köklerin Kuru Ağırlığı ve Azami Genleşme Açıları [23]

Beyaz vd. (2020), kesme birim deformasyonu ve rölatif sıkılığın, temiz ince deniz kumunda, kumların sıvılaşma enerjisinin belirlenmesine etkisini, daha önce kullanılmayan bir Devirsel Basit Kesme Düzeneği (DBKD) kullanarak incelemiştir. Cihazın yaygın olarak kullanılan ve sadece düşey yönde tekrarlı yük uygulayabilen cihazlardan farkı, düşeyde dinamik yük ve yatayda iki yönde dinamik kesme kuvveti uygulayabilmesidir. Yapılan 36 deney sonucunda, sıvılaşma potansiyelinde, kesme birim deformasyon oranındaki artış sonucu %3'lük bir azalma meydana gelirken, artan rölatif sıkılığın, kumda kesme direncini artırdığı, sonuç olarak da devir sayısında artış ve sıvılaşmada gecikme gözlemlenmiştir [24].

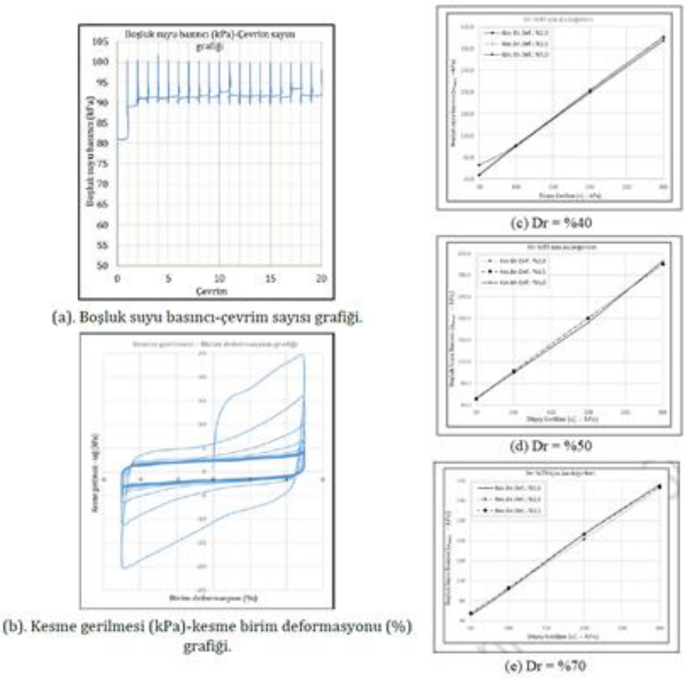

Şekil 16. (a) ve (b) DBKD'den Elde Edilen Grafik Örnekleri. (c), (d) ve (e) Farklı Rölatif Sıkılıktaki Kumların, Farklı Kesme Birim Deformasyon Oranında Boşluk Suyu Basıncı Grafikleri [24]

Genel olarak, konsolidasyon parametreleri laboratuvarda ödometre deneyleri ile yerçekimi şartlarında (1g) gerçekleştirilmekle birlikte, bu süreç uzun zaman almaktadır. Her ne kadar bu süreyi azaltmak için statik yaklaşıma alternatif olarak daha yüksek ivmeli dinamik yaklaşımlar geliştirilmiş olsa da bu yöntemler pahalı ve çok büyük santrifüjlere gereksinim duymaktadır. Dahası, bu santrifüjler, uygulamadan ziyade araştırma odaklıdır. Bu nedenlerle Balcı vd. (2018), çok küçük boyutlu (minyatür) bir santrifüj cihazının konsolidasyon deneylerine uygulanabilirliğini ele almıştır. Sonuç olarak bu düzeneğin, deney süresini birkaç saate düşürdüğü, kullanılan yeni bir parametre ile (Wce: Santrifüj yükü) örselenmemiş numuneler için geleneksel konsolidasyon deney sonuçları ile ilişkilendirmenin sağlandığı ve bakir sıkışma çizgisinin yüksek kesinlik, ön konsolidasyon basıncının ise orta kesinlik ile belirlenebildiği ve doğal numunelere uygulandığında da ümit vadettiği belirtilmiştir [25].

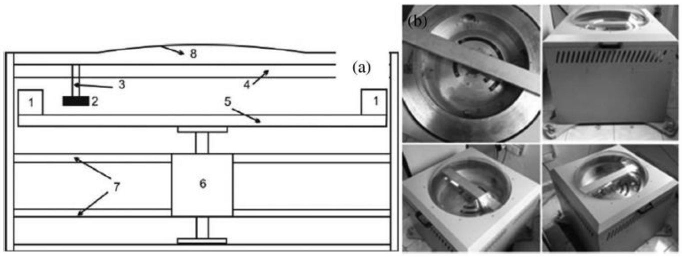

Şekil 17. Araştırmada Kullanılan Minyatür Santrifüj Cihazı (a) Enkesit (b) Genel Görünüm [25]

Mekanik stabilizasyonla zemin iyileştirme sıklıkla, çukurlardan alınan önemli miktarda zemin gerektiren standart Proctor deneyi kullanılarak uygulanmaktadır. Statik kompaksiyon ise alternatif bir laboratuvar deneyidir. Araştırmacılar minyatür boyutlardaki statik kompaksiyon deneylerinin azami kuru yoğunluk ve optimum su muhtevası yönünden standart Proctor deneyi ile kıyaslanabileceğini göstermiş olsalar da drenajsız kayma mukavemeti ve hidrolik iletkenlik gibi sıkışmış zeminin iki esas özelliği konusunda çalışılmamıştır. Kayabalı vd. (2020), (1) standart Proctor deneyindekine benzer sıkışma eğrilerini elde etmek, (2) optimum su muhtevasında standart Proctor ve statik kompaksiyon deneyleri ile sıkışmış zeminleri yeniden oluşturmak ve (3) sıkışmış zeminlerin drenajsız kayma mukavemeti ve hidrolik iletkenliklerini kıyaslamak için gerekli statik kompaksiyon enerjisi seviyesini tahmin edebilmek için bir çalışma gerçekleştirmiştir. Sonuç olarak statik kompaksiyon ile, standart Proctor için gereken enerjinin yaklaşık %40'ı, gereken zemin hacminin ise sadece yaklaşık %10'u kullanılarak kıyaslanılabilir hidrolik iletkenlik ve drenajsız kayma mukavemeti değerleri elde edildiği belirtilmiştir [26].

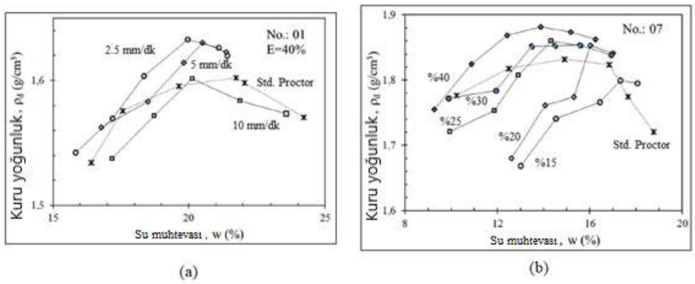

Şekil 18. a) Standart Proctor ve 2.5, 5 ve 10 mm/dk Gerinim Hızı ile Elde Edilmiş Statik Kompaksiyon Eğrileri, (b) Standart Proctor ve Standart Proctor Enerjisinin %15'i, %20'si, %25'i, %30'u ve %40'ı için Elde Edilmiş Statik Kompaksiyon Eğrileri [26]

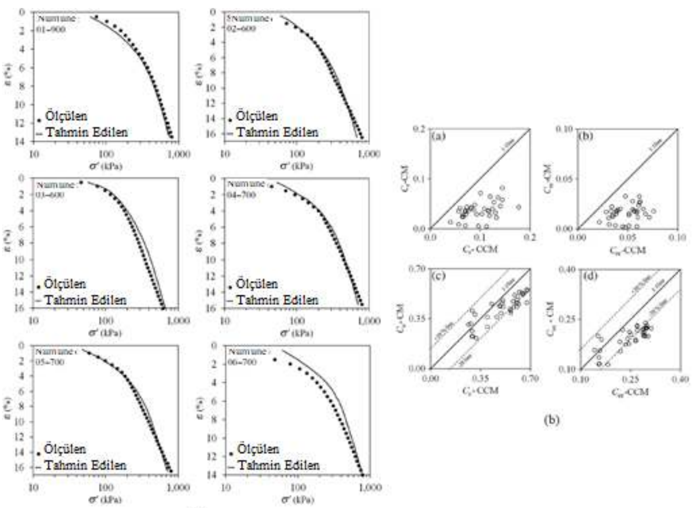

Şekil 19. (a) Ölçülen ve Tahmin Edilen Efektif Gerilmeler, (b) Laboratuvarda Hazırlanan Numunelerde Santrifüj Konsolidasyonu (CCM) ve Geleneksel Konsolidasyon (CM) Yöntemleriyle Elde Edilmiş Sıkışma İndisleri Karşılaştırması [26]

Hidrat içeren sedimentlerin fiziksel doğası ve mekanik davranışlarının anlaşılması, metan gaz hidrat kaynaklarının potansiyellerinin belirlenebilmesi için büyük önem arz etmektedir. Basınçlı karot alma teknikleri ve işleme ekipmanları, bozulmamış (örselenmemiş) numunelerin, yerinde maruz kaldıkları basınçlar altında alınabilmesine olanak sağlamış olsa da bu numunelerin arazi basınç şartları altında testleri mümkün olmamıştır. Priest vd. (2014), bu sorunun üstesinden gelebilmek için, söz konusu bu numunelerin fiziksel ölçümlerinin gerçekleştirilebilmesi için PCATS Üç Eksenli Aparatı'nı geliştirmiş, bu aparatla belirli sayıda basınçlı karot alt numunesi elde ederek başarılı bir şekilde test etmiş, rezonans deneylerinden küçük gerinim rijitliği, üç eksenli kayma testlerinden gerilme-gerinim özellikleri ve permeabilite gibi birtakım geomekanik özellikleri belirlemiştir. Deneyler sonucunda, rijitlik ve drenajsız kayma mukavemetinin, artan dane büyüklüğü, hidrat doygunluğu ve uygulanan efektif gerilme ile arttığı, hidrat içeren kumlarda, hidratsız killere kıyasla permeabilitenin önemli ölçüde azaldığı sonuçlarına ulaşılmıştır [27].

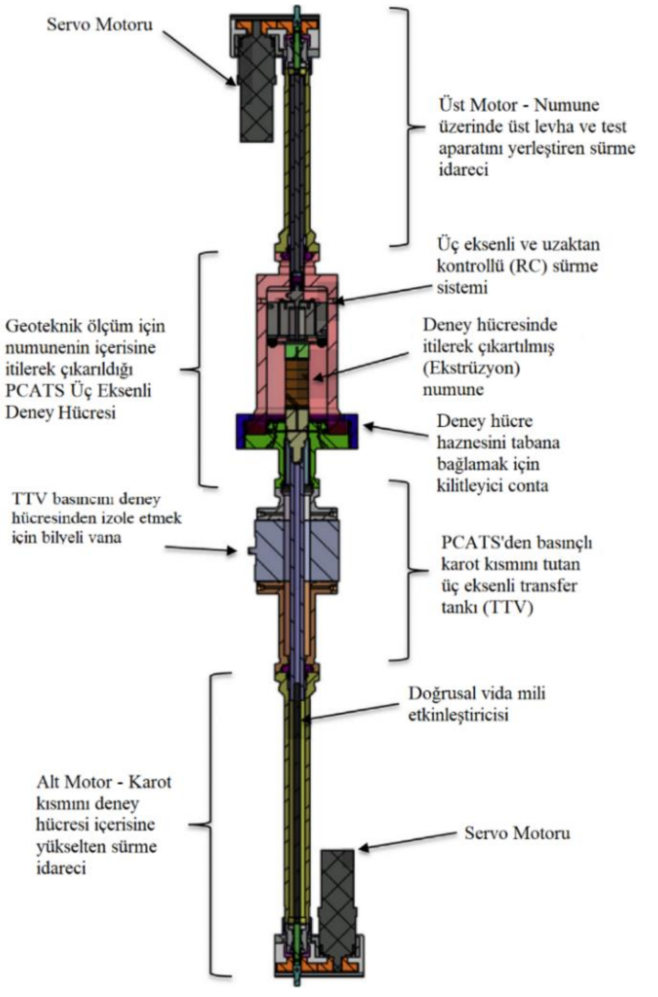

Şekil 20. PCATS Üç Eksenli Aparatı Bütün Görünümü [27]

Suwal ve Kuwano (2018), elastik dalga ölçümü için yeni geliştirilen bir teknik ile bir disk güç dönüştürücü yöntem ve emme ölçümü için bir basınçlı membran tekniğini, silindir bir numunenin hem matrik emmesi hem de elastik dalgalarının teminini sağlayan modifiye edilmiş bir üç eksenli aparatında birleştirmiştir. Aparat, kumlu zeminde 100 kPa'dan az düşük emme aralığında emme değişimini değerlendirmek için oluşturulmuştur. Hem sıkışma hem de kayma dalgaları, ilgili matrik emme ile birlikte ölçülmüştür. Matrik emme, numunelere su enjeksiyonu ile çeşitlendirilmiş ve ilgili elastik dalga hızları disk güç dönüştürücü ile bulunmuştur. Bu çalışma, disk güç dönüştürücü yönteminin doygun olmayan zemin numunelerine uygulanabilirliğini ve düşük aralıkta emme gösteren kumlu zeminlerin mekanik davranışı üzerine matrik emmenin etkilerini desteklemektedir [28].

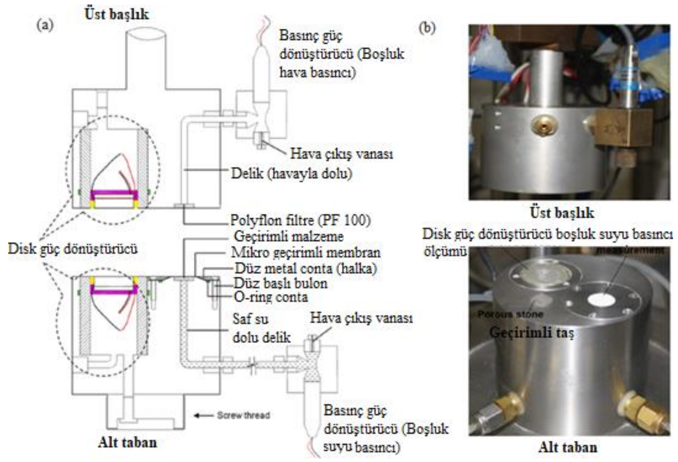

Şekil 21. (a) Matrik Emme ve Elastik Dalga Ölçüm Düzeneği Gösterimi, (b) Üst Başlık ve Alt Taban Fotoğrafı [28]

Li ve Zhang (2014), doygun olmayan zeminlerde matrik emmenin laboratuvarda tespiti amacıyla ticari basınç güç dönüştürücüler için iki yeni yüksek emmeli gerilimölçer (tansiyometre) tasarlamış ve üretmiştir. Yapılan serbest buharlaşma deneyleri sonucu azami ulaşılabilir emmenin yaklaşık 1100 kPa olduğu görülmüştür. Mevcut yüksek emmeli tansiyometrelere kıyasla, yeni geliştirilen cihazların sağlam ve doygun olmayan zeminlerde matrik emme ölçümü için güvenilir olduğu görülmüştür [29].

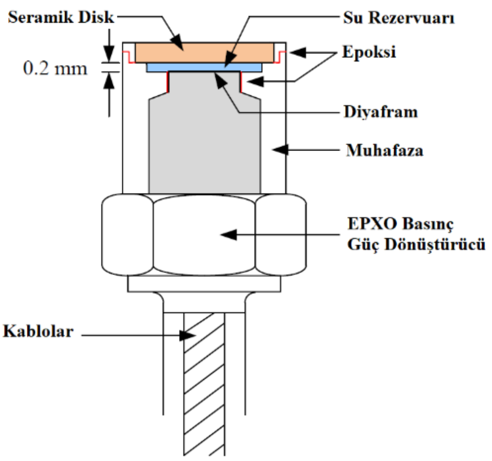

Şekil 22. Geliştirilen Tansiyometrenin Şematik Gösterimi [29]

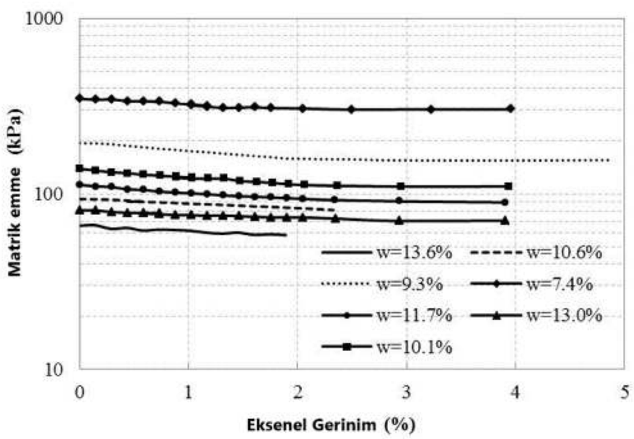

Şekil 23. Serbest Basınç Deneyi Esnasında Farklı Su Muhtevalarına Sahip Zemin Örneklerinde Matrik Emme Ölçüm Sonuçları [29]

3. Tartışma

Son yıllarda, zemin özellikleri ve zemin davranışı tahmin modelleri oluşturulmasında makine öğrenmesi veya yapay zekâ yöntemleri gibi uzman sistemler kullanımı yaygınlaşmıştır. Uzman sistemler kullanarak zemin özellikleri başarılı bir şekilde tahmin edildiği literatürde görülmektedir. Zemin özellikleri ve zemin davranışının belirlenmesi için geleneksel deney aletlerinin çeşitli modifikasyonlarda geliştirilerek kullanımı veya yeni üretilen deney sistemleri tasarımına günümüzde sıkça rastlanılmaktadır. Bu yeni nesil deney sistemleri ile başarılı çalışmalar yapıldığı literatürde yer bulmaya başlamıştır.

4. Sonuçlar ve Öneriler

Bu çalışmada geoteknik mühendisliğinde zemin özelliklerinin belirlenmesi ve zemin davranışının açıklanmasına yönelik yeni nesil yöntemlerin tanıtılması amaçlanmıştır. Zemin özelliklerinin belirlenmesi ve zemin davranışının açıklanması için günümüzde yapay sinir ağları, bulanık mantık gibi uzman sistemler sıkça kullanılmaktadır. Yapay sinir ağlarının geleneksel regresyon yöntemlerine göre avantajlı bir yöntem olduğu vurgulanmalıdır, yani model bir kez eğitilip test edildikten sonra, belirlenen koşullar altında yerleşimlerin tahmini için doğru ve hızlı bir araç olarak kullanılabilmektedir. Diğer yandan mevcut deneysel ekipmanların modifikasyonu ve geleneksel deney metodolojilerinin geliştirilmesi de çalışmalarda artış göstermiştir. Bu aletler ile deney sürelerinin kısalması ve daha doğru sonuçlar elde edilmesi mümkün hale gelmiştir. Geoteknik mühendisliğinde yeni nesil trendlerin kullanımı ile yeni bir safhaya geçildiği düşünülmektedir.

5. Teşekkür

Yazar Asena KARSLIOĞLU Tübitak Bideb 2211-A Genel Yurt İçi Doktora Bursu ve YÖK 100/2000 Doktora Bursu ile desteklenmesinden dolayı ilgililere teşekkür eder.

Kaynaklar

[1] Venkatramaiah, C. (1995). Geotechnical engineering. New Age International.

[2] Erol, A. O., & Çekinmez, Z. (2014). Geoteknik mühendisliğinde saha deneyleri. Yüksel Proje Yayınları.

[3] Isik, F., & Ozden, G. (2013). Estimating compaction parameters of fine-and coarse-grained soils by means of artificial neural networks. Environmental earth sciences, 69(7), 2287-2297.

[4] Momeni, E., Nazir, R., Armaghani, D. J., & Maizir, H. (2014). Prediction of pile bearing capacity using a hybrid genetic algorithm-based ANN. Measurement, 57, 122-131.

[5] Díaz, E., Brotons, V., & Tomás, R. (2018). Use of artificial neural networks to predict 3-D elastic settlement of foundations on soils with inclined bedrock. Soils and Foundations, 58(6), 1414-1422.

[6] Tran, T. T., Han, S. R., & Kim, D. (2018). Effect of probabilistic variation in soil properties and profile of site response. Soils and Foundations, 58(6), 1339-1349.

[7] Oztoprak, S., Sargin, S., Uyar, H. K., & Bozbey, I. (2018). Modeling of pressuremeter tests to characterize the sands. Geomechanics and Engineering, 14(6), 509-517.

[8] Pham, B. T., Hoang, T. A., Nguyen, D. M., & Bui, D. T. (2018). Prediction of shear strength of soft soil using machine learning methods. Catena, 166, 181-191.

[9] Reale, C., Gavin, K., Librić, L., & Jurić-Kaćunić, D. (2018). Automatic classification of fine-grained soils using CPT measurements and Artificial Neural Networks. Advanced Engineering Informatics, 36, 207-215.

[10] Sihag, P. (2018). Prediction of unsaturated hydraulic conductivity using fuzzy logic and artificial neural network. Modeling Earth Systems and Environment, 4(1), 189-198.

[11] Azadmard, B., Mosaddeghi, M. R., Ayoubi, S., Chavoshi, E., & Raoof, M. (2020). Estimation of near-saturated soil hydraulic properties using hybrid genetic algorithm-artificial neural network. Ecohydrology & Hydrobiology, 20(3), 437-449.

[12] Ingale, R., Patel, A., & Mandal, A. (2020). Numerical modelling of bender element test in soils. Measurement, 152, 107310.

[13] Adab, H., Morbidelli, R., Saltalippi, C., Moradian, M., & Ghalhari, G. A. F. (2020). Machine learning to estimate surface soil moisture from remote sensing data. Water, 12(11), 3223.

[14] Straż, G., & Borowiec, A. (2020). Estimating the Unit Weight of Local Organic Soils from Laboratory Tests Using Artificial Neural Networks. Applied Sciences, 10(7), 2261.

[15] Pham, B. T., Qi, C., Ho, L. S., Nguyen-Thoi, T., Al-Ansari, N., Nguyen, M. D., ... & Prakash, I. (2020). A novel hybrid soft computing model using random forest and particle swarm optimization for estimation of undrained shear strength of soil. Sustainability, 12(6), 2218.

[16] Kayabali, K., Akturk, O., Fener, M., Ozkeser, A., Ustun, A. B., Dikmen, O., ... & Asadi, R. (2016). Determination of Atterberg limits using newly devised mud press machine. Journal of African Earth Sciences, 116, 127-133.

[17] Dantas, G. H. S., Furlan, A. P., Fabbri, G. T. P., & Suárez, D. A. A. (2016). On gyratory compaction of a clayey soil. EJGE, 21(17), 5725-5733.

[18] Zhao, C., Koseki, J., & Sasaki, T. (2018). Image based local deformation measurement of saturated sand specimen in undrained cyclic triaxial tests. Soils and Foundations, 58(6), 1313-1325.

[19] Lu, C., Lu, J., Zhang, Y., & Puckett, M. H. (2019). A convenient method to estimate soil hydraulic conductivity using electrical conductivity and soil compaction degree. Journal of Hydrology, 575, 211-220.

[20] Alkayış M.H., Laboratuvar Ölçekli Santrifüj Deney Sitemi ile Zemin Parametrelerinin Tayini. (2019) Yüksek Lisans Tezi, Eskişehir Teknik Üniversitesi.

[21] Kučerík, J., Svatoň, K., Malý, S., Brtnický, M., Doležalová-Weismannová, H., Demyan, M. S., ... & Tokarski, D. (2020). Determination of soil properties using thermogravimetry under laboratory conditions. European Journal of Soil Science, 71(3), 415-419.

[22] Lozovsky, I. N., Zhostkov, R. A., & Churkin, A. A. (2020). Numerical Simulation of Ultrasonic Pile Integrity Testing. Russian Journal of Nondestructive Testing, 56(1), 1-11.

[23] Yildiz, A., Graf, F., Rickli, C., & Springman, S. M. (2018). Determination of the shearing behaviour of root-permeated soils with a large-scale direct shear apparatus. Catena, 166, 98-113.

[24] Beyaz, T., KAYABALI, K., & SÖNMEZER, Y. B. (2021). Kumların sıvılaşmasında rölatif sıkılık ve kesme birim deformasyonu etkisinin incelenmesi. Pamukkale Üniversitesi Mühendislik Bilimleri Dergisi, 27(3), 431-440.
[25] Balci, M. C., Kayabali, K., & Asadi, R. (2018). Miniature Centrifuge Modeling for Conventional Consolidation Test. Geotechnical Testing Journal, 41(3), 590-600.
[26] Kayabali, K., Asadi, R., Fener, M., Dikmen, O., Habibzadeh, F., & Aktürk, Ö. (2020). Estimation of the compaction characteristics of soils using the static compaction method. Bulletin of the Mineral Research and Exploration, 162(162), 75-82.
[27] Priest, J. A., Druce, M., Roberts, J., Schultheiss, P., Nakatsuka, Y., & Suzuki, K. (2015). PCATS Triaxial: A new geotechnical apparatus for characterizing pressure cores from the Nankai Trough, Japan. Marine and Petroleum Geology, 66, 460-470.
[28] Suwal, L. P., & Kuwano, R. (2018). Triaxial apparatus equipped with elastic waves and matric suction measurement techniques. Soils and Foundations, 58(6), 1553-1562.
[29] Li, L., & Zhang, X. (2014). Development of a new high-suction tensiometer. In Soil behavior and Geomechanics (pp. 416-425).

Geotechnical Effects of Hurricane Harvey
in the Houston, Beaumont, and Port Arthur Areas

Geotechnical Effects of Hurricane Harvey in the Houston, Beaumont, and Port Arthur Areas

R. Lee Wooten, *Principal, GEI Consultants, Inc., Woburn, MA, USA; email: lwooten@geiconsultants.com*
Stacey Kulesza, *Ph.D., P.E., Assistant Professor, Civil Engineering, Kansas State University, Manhattan, KS, USA; sekulesza@k-state.edu*
Chadi El Mohtar, *Ph.D., Associate Professor, Civil, Architectural and Environmental Engineering, The University of Texas at Austin, Austin, Texas, USA; elmohtar@mail.utexas.edu*
Brian Diaz, *PhD Student, Zachry Department of Civil Engineering, Texas A&M University, College Station, Texas, USA; Briandavd@gmail.com*
Olusola Ilupeju, *PhD Student/Graduate Assistant, Zachry Department of Civil Engineering, Texas A&M University, College Station, Texas, USA; olusola.ilupeju@tamu.edu*
Marcus Rasulo, *PhD Student, Zachry Department of Civil Engineering, Texas A&M University, College Station, Texas, USA; marcusrasulo@gmail.com*
Patrick Bassal, *P.E., Geotechnical Engineer, WSP, New York, NY, USA; patrick.bassal@wsp.com*
Ahmed Hussien, *PhD Student, Civil, Architectural and Environmental Engineering, The University of Texas at Austin, Austin, Texas, USA; ahussien@utexas.edu*
Behdad Mofarraj Kouchaki, *PhD Student, Civil, Architectural and Environmental Engineering, The University of Texas at Austin, Austin, Texas, USA; mofarraj@utexas.edu*
Michael V. Little, *PhD Student, Civil, Architectural and Environmental Engineering, The University of Texas at Austin, Austin, Texas, USA; mvlittle@utexas.edu*
Ahmet A Mert, *Graduate student, Civil, Architectural and Environmental Engineering, The University of Texas at Austin, Austin, Texas, USA; ahmetalimert@utexas.edu*
Christopher W. Nelsen, *Graduate Student, Civil, Architectural and Environmental Engineering, The University of Texas at Austin, Austin, Texas, USA; nelsenc@utexas.edu*

ABSTRACT: *The Geotechnical Extreme Events Reconnaissance (GEER) Association deployed multiple teams of engineers from academia and practicing firms to the coast of Texas in late August and early September 2017 following Hurricane Harvey. This report summarizes the observations and data from the GEER team that focused primarily on the inland effects of Hurricane Harvey in the Houston area with some observations in the Port Arthur / Beaumont area east of Houston. Rain, not storm surge or wind, caused the observed damage in Houston, Beaumont, and Port Arthur by overwhelming stormwater management facilities and creating high flows and flooding in and near area waterways. The major Houston-area flood structures, Addicks and Barker Dams, performed well from a geotechnical perspective. Observed damages included shallow slides along levees, severe erosion along riverways, isolated road and culvert erosion and uplift, and area-wide flood effects in low and poorly drained neighborhoods.*

KEYWORDS: hurricane, flood, erosion, dam, levee, highway, residential

SITE LOCATION: **Geo-Database**

INTRODUCTION

Hurricane Harvey affected a wide area along the Texas coast with both high wind and unprecedented, for the area, rainfall totals. The damage in the Houston and Beaumont / Port Arthur areas was largely due to the flooding and stream flow that resulted from the rain. The GEER Hurricane Harvey Houston team (GEER Houston) visited Houston area sites that were

Submitted: 12 August 2018; Published: 2 July 2020
Reference: Wooten L., Kulesza S., El Mohtar C., Diaz B., Ilupeju O., Rasulo M., Bassal P., Hussien A., Mofarraj Kouchaki B., Little M. V., A Mert A., and Nelsen C. W. (2020). Geotechnical Effects of Hurricane Harvey in the Houston, Beaumont, and Port Arthur Areas. International Journal of Geoengineering Case Histories, Volume 5, Issue 4, pp. 77-105, doi: 10.4417/IJGCH-05-04-05

known to be of significance for flood risk reduction or were identified by the media as areas with affected infrastructure. Figure 1 shows the ten areas of significance visited by GEER Houston, followed by a legend listing the site names. Descriptions of observations at each site can be found in later sections of this paper.

This report summarizes the following aspects of the GEER Houston team reconnaissance:

- Description of the Hurricane Harvey rainfall.
- Performance of the two large U.S. Army Corps of Engineers (USACE) flood protection dams, Addicks and Barker Dams.
- Performance of area levees built and maintained by Levee Improvement Districts (LIDs).
- Erosion along area rivers, bayous, and streams.
- Highway damage.
- Residential impacts.

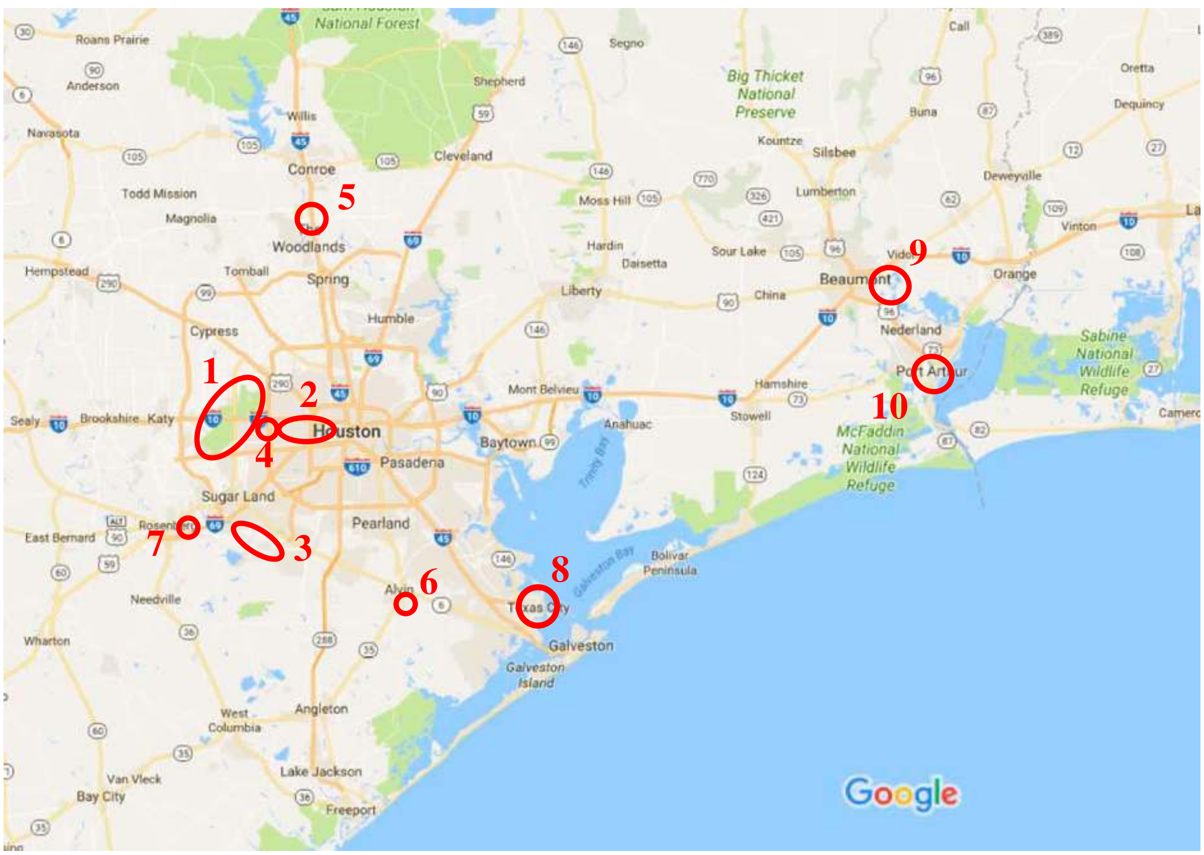

Figure 1. Observation Areas by GEER Hurricane Harvey Houston Team (see following list for site names). 1 – USACE Houston Flood Risk Management Dams – Barker and Addicks Dams, 2 – Buffalo Bayou, 3 – Brazos River Levees, 4 – Beltway 8 Underpass Slab, 5 – San Jacinto River Bridges, 6 – Mustang Bayou Bridge, 7 – FM 762 Road Culvert, 8 – Texas City Levees, 9 – Beaumont, 10 – Port Arthur

HURRICANE HARVEY

Harvey began as a tropical wave off the west coast of Africa on August 13, 2017, moved westward across the Atlantic Ocean and Caribbean Sea, and made landfall on the Texas coast on August 25 as a Category 4 hurricane. The storm continued to the northwest and eventually stalled over Houston on August 26 before changing direction again and heading back southeast.

Harvey made landfall one final time as a tropical strom near Cameron, Louisiana, on August 30. Fig. 2 shows the trajectory of the storm center as well as flood levels in some coastal areas.

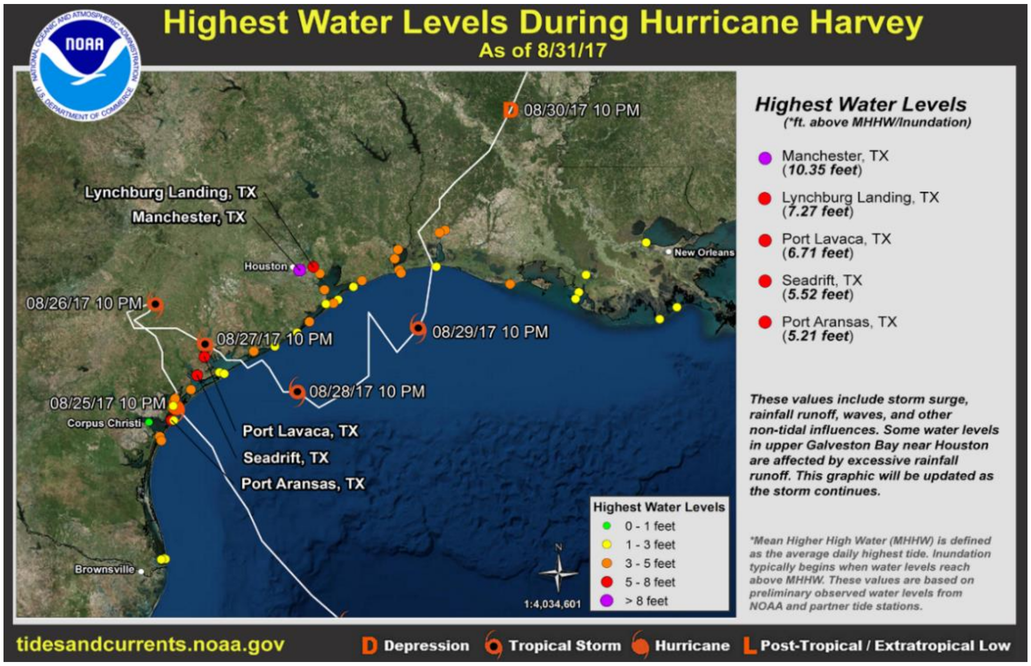

Figure 2. Harvey's path with the highest flood levels (NOAA, 2017).

The stalling of Harvey over the Houston area led to considerable amounts of rainfall, with much of the Houston area receiving at least 102 cm (40 inches) of rainfall (Fig. 3). South Houston received nearly 114 cm (45) inches of rainfall during this event. The largest amount of rainfall was recorded as 154 cm (60.6 inches) near Nederland, Texas. This massive amount of rain caused severe flooding along the area's rivers. Most of the damages from this event were caused by flooding. Early estimates placed the cost of Hurricane Harvey at $70-180 billion (USD).

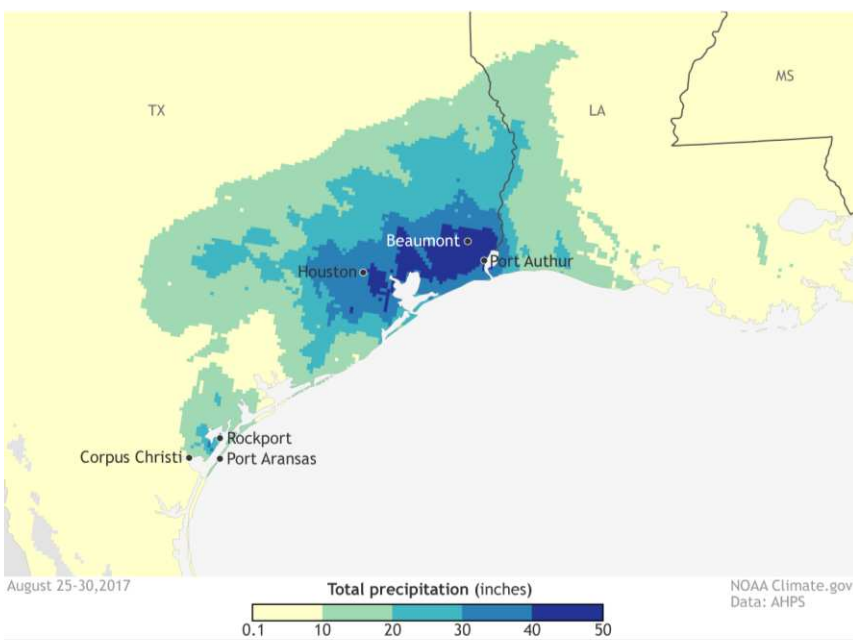

Figure 3. Rainfall totals in Texas from Hurricane Harvey, sourced from the National Weather Service.
(https://www.climate.gov/news-features/event-tracker/reviewing-hurricane-harveys-catastrophic-rain-and-flooding)

ADDICKS AND BARKER DAMS

Descriptions

In 1929 and 1935, major flood events occurred in Houston. The USACE responded to these floods by constructing the Addicks and Barker Dams in a large and mostly undeveloped region west of Houston and east of Katy between 1942 and 1948. The Addicks Dam is located on the north side of Interstate 10, the Barker Dam is on the south side of Interstate 10, and both are flanked by West Sam Houston Parkway on the east and Fry Street on the west (see Fig. 4).

Both dams are long earth embankments, with each dam having one gated outlet structure near mid-length and two auxiliary spillways, one at each end. Key characteristic data for the dams are given below. Note that all elevations in this paper are relative to NAVD 88.

<u>Addicks Dam</u>
Length: 22,200 m (72,900 ft or13.8 miles)
Maximum height: ~11 m (~36 ft)
Crest elevation: 36.9 m (121.0 ft)
Natural ground elevations at ends of auxiliary spillways: north – 32.9 m (108 ft), south – 34.1 m (112 ft)
Maximum storage capacity: 248 million cubic meters (201,000 acre-ft)
North auxiliary spillway length: ~2.595 m (~8,480 ft)
South auxiliary spillway length: ~3,206 m (~10,520 ft)
Previous maximum pool elevation: 31.3 m (102.7 ft) (April 2016)

<u>Barker Dam</u>
Length: 18,800 m (61,666 ft or 11.7 miles)
Maximum height: 15 m (~50 ft)
Crest elevation: 34.5 m (113.1 ft)
Natural ground elevations at ends of auxiliary spillways: 31.7 m (104 ft)
Maximum storage capacity: 258 million cubic meters (209,000 acre-ft)
North auxiliary spillway length: ~887 m (~2,910 ft)
South auxiliary spillway length: ~3,545 m (~11,630 ft)
Previous maximum pool elevation: 29.1 m (95.24 ft) (April 2016)

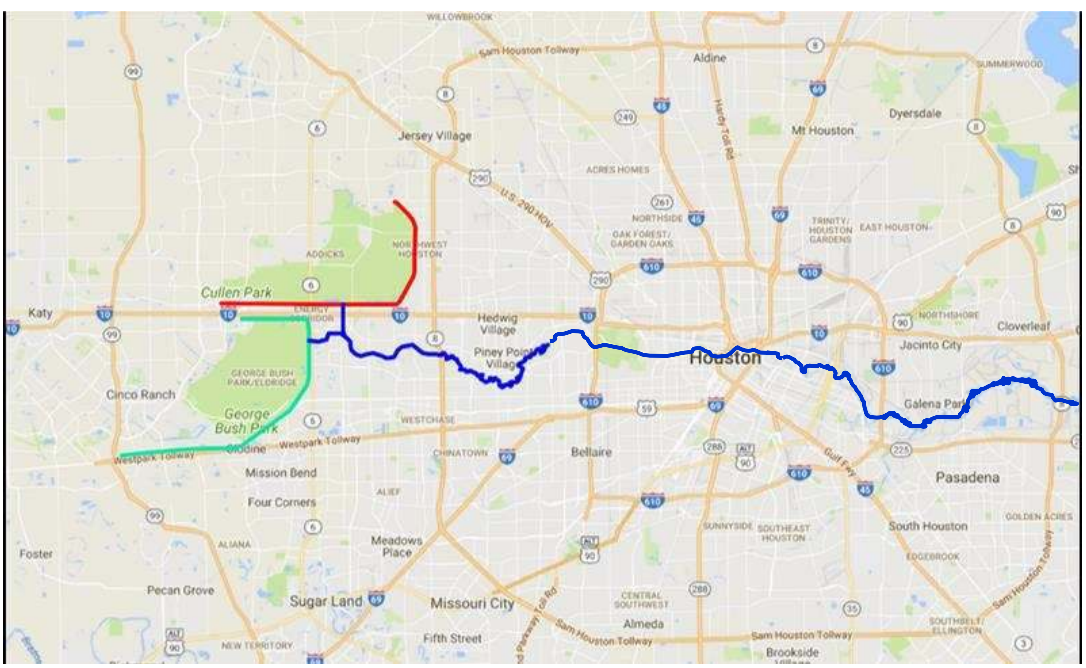

Figure 4. Addicks (red) and Barker (green) Dams and their feed into the Buffalo Bayou (blue) (Google Maps).

Normal reservoir outflows occur through a gate structure and channel at each dam, into east-flowing Buffalo Bayou, through Houston and into the central business district where it joins White Oak Bayou, and continue east to the Houston Ship Channel. Based on personal communications with USACE personnel, the Addicks and Barker Reservoirs are dry about 95% of time, allowing them to host several recreational facilities, which were visited more than 4.4 million times in 2008 (USACE, 2009). Several local roads traverse the dams and reservoirs for use during normal, low water periods. In addition to the gated outlets, both dams also have long auxiliary spillways across the ends of the earth embankments. The auxiliary spillway crests are covered with roller compacted concrete (RCC) for scour protection.

The Addicks and Barker Dams and the property owned by the USACE within the reservoir are abutted by residential and commercial developments. The USACE property within the reservoirs extends to elevations of 31.5 m (103.2 ft) for Addicks and 29.0 m (95.0 ft) for Barker. For reference, the 100-year-flood levels are estimated to be El. 30.6 m (100.5 ft) (Addicks) and El. 29.1 m (95.5 ft) (Barker). The dams are designed to contain floods in excess of the 100-year flood. Residential development extends up to these property lines, and one could stand on the auxiliary spillways, look upstream, and see housing within the reservoir area.

At the time of Harvey's arrival, the USACE was in the middle of remedial construction projects on the dams. These projects included replacing the gate structures for both dams, which required the construction of two cofferdams, construction of slurry trench cutoff walls at the structures and, at a potential seepage location at Barker, filling of voids under the outlet conduits, installation of a seepage controlling granular filter along the conduit, and construction of a parabolic spillway.

Performance

Our primary focus was to document geotechnical aspects of the dams associated with the high-water levels of Hurricane Harvey. Fortunately, during and after the hurricane, the Addicks and Barker Dams were stable and showed no signs of distress from a geotechnical standpoint.

Although hydrologic/hydraulic performance of the dams was outside of our purpose and primary expertise, it appeared that Addicks and Barker Dams fulfilled their mission of reducing the impact of flooding for a significant part of the Houston area, specifically along Buffalo Bayou downstream of the dams, including the central business district. During the heaviest rainfall, around 86-89 cm (34-35 inches) of rainfall was recorded in the watershed. Peak reservoir levels occurred on about August 30, 2017 at 33.3 m (109.1 ft) and 31.0 m (101.6 ft) in the Addicks and Barker reservoirs, respectively. The highest elevations of the crest for these two dams are 34.1m (121 ft) and 34.1 m (112 ft), respectively, which provided freeboards of approximately 3.4 m (11 ft) (Addicks) and 3.0 m (10 ft) (Barker) at the peak reservoir levels. The peak reservoir water level in Addicks slightly exceeded the level of the ground at the north end of Addicks north auxiliary spillway (details below). The USACE opened the Addicks outflow gates on August 28, 2017 to reduce risks associated with higher water levels. These outflows peaked around August 30, 2017 at about 200 cubic meters/second (m^3/s) (7,000 cubic ft per second [cfs]) for Addicks and 180 m^3/s (6,300 cfs) for Barker. The USACE noted that Addicks and Barker Dams reduced peak flows in Buffalo Bayou by more than 3,540 m^3/s (125,000 cfs) during the April 2016 flooding, a smaller event than Hurricane Harvey. The April 2016 event, also known as the Tax Day Flood, resulted from about 43 cm (17 inches) of rain, which accumulated over just 12 hours and caused the previous record pools for the dams. During the time of our visit on September 9, 2017, the gates of the dams were opened to allow flows of 170 m^3/s (6,000 cfs) (Addicks) and 110 m^3/s (4,000 cfs) (Barker) for a total flow into the Buffalo Bayou of 280 m^3/s (10,000 cfs) (see Figs. 5 and 6). The USACE gradually reduced outflows from these levels to a total of 110 m^3/s (4,000 cfs) on September 17, 2017.

Figure 5. Addicks outlet releasing ~170 m^3/s (~6000 cfs) (September 9, 2017, 29.79026° N, 95.62378° W).

Figure 6. Barker outlet releasing ~110 m^3/s *(~4000 cfs) (September 9, 2017, 29.76977° N, 95.64629° W).*

The USACE had contracted to construct new outlet structures and cutoff walls at each dam. This construction was in progress at the time of Hurricane Harvey and was suspended until the consequences of and recovery from the flooding could be assessed. At the time of the hurricane, cofferdams were in place and parts of the cutoff walls had been constructed. The cofferdams performed suitably in keeping the water in the reservoir from flooding the construction zone; however, the high backwater from the channel to Buffalo Bayou flooded the Addicks construction zone (see Fig. 7), and rainwater and underseepage pooled in the Barker cofferdammed area.

Figure 7. Interior of Addicks construction cofferdam for new outlet structure, flooded from Buffalo Bayou backwater; note erosion channels on slopes (September 9, 2017, 29.79063° N, 95.62586° W).

High water in the Addicks Reservoir (~33.3 m [~El. 109.1 ft]) exceeded the elevation of the level ground at the end of the north auxiliary spillway RCC (~El. 108), resulting in small outflows (~6 m^3/s [~200 cfs]) that began on August 29, 2017. Figure 8 shows this area on September 7, 2017 when some small spillage was still taking place. These outflows were within the design intent of the dam and the auxiliary spillway, and should not be described as dam overtopping. Overtopping implies that the water levels have risen above the main dam, which is typically a serious condition that can lead to rapid erosion of the dam and a dam failure.

Figure 8. North end of Addicks auxiliary spillway (September 3, 2017, 29.84977° N, 95.58904° W, photo by USACE).

The high-water levels in the Addicks (El. 33.3 m [El. 109.1 ft]) and Barker (El. 31.0 m [El. 101.6 ft]) Reservoirs exceeded not only the April 2016 historic high levels (El. 31.3 m [102.7 ft] at Addicks and El. 29.0 m [95.24 ft] at Barker) but also the elevations at the upstream edge of the USACE property. As noted previously, housing developments extended up to these boundaries and, consequently, were flooded during Harvey (see Figs. 9, 10, and 11). Area subsidence likely contributed to the upstream extent of flooding. Subsidence in the Houston area is due to consolidation of the underlying aquifers resulting from groundwater withdrawal and has resulted in elevation changes as large as 3.0 m (10 ft) (USGS). The 1.2 m (4 ft) difference in elevations between the two emergency spillways at Addicks Dam is due to this subsidence.

Figure 9. Aerial photograph of flooding within the Addicks Reservoir along the south auxiliary spillway (September 3, 2017, 29.79222° N, 95.68830° W, USACE photograph).

Figure 10. Flooded residential area in the southwest corner of the Barker Dam (September 9, 2017, 29.70706° N, 95.72835° W).

Figure 11. High water mark on fences surrounding residential area (September 9, 2017, 29.70706° N, 95.72835° W).

Nearby runoff that is not captured by the dams is managed in drainage ditches or creeks immediately adjacent to the dams' downstream toes. These drainage channels, along with numerous other stormwater / flood management features, are managed by the Harris County Flood Control District. The team observed several slope failures that will require repairs along Turkey Creek near the southeast corner of Addicks Dam (see Figure 12). Contributing factors to the sloughs could have included the steepness of the banks, flow forces acting on trees on the banks or diverted by trees in the waterway, undercutting by flood flows, reduced shear strength in the clay soils, and the drawdown of the creek water level.

Figure 12. Slope failures along Turkey Creek drainage ditch (September 9, 2017, 29.79009° N, 95.59639° W).

LEVEE IMPROVEMENT DISTRICTS (LIDS) LEVEES

Fort Bend County, southwest of Houston, is home to 19 levee improvement districts (LIDs) and municipal utility districts (MUDs) that maintain levee systems along the Brazos River. These districts have constructed and manage about 160 km (100 miles) of levees systems, along with large drainage ditches, outfall structures, pump stations, flood gates, detention/retention ponds, internal drainage systems, and other stormwater management facilities to protect residents in their districts from flooding from both the Brazos and from stormwater internal to the levees. Residents within the districts fund the construction and management of these facilities through property taxes. Figure 13 shows the LIDs (green) and MUDs (purple) with levees (red dashed lines) in Fort Bend County along with the numbered locations of various features that are described herein. The numbering legend is given below in the figure.

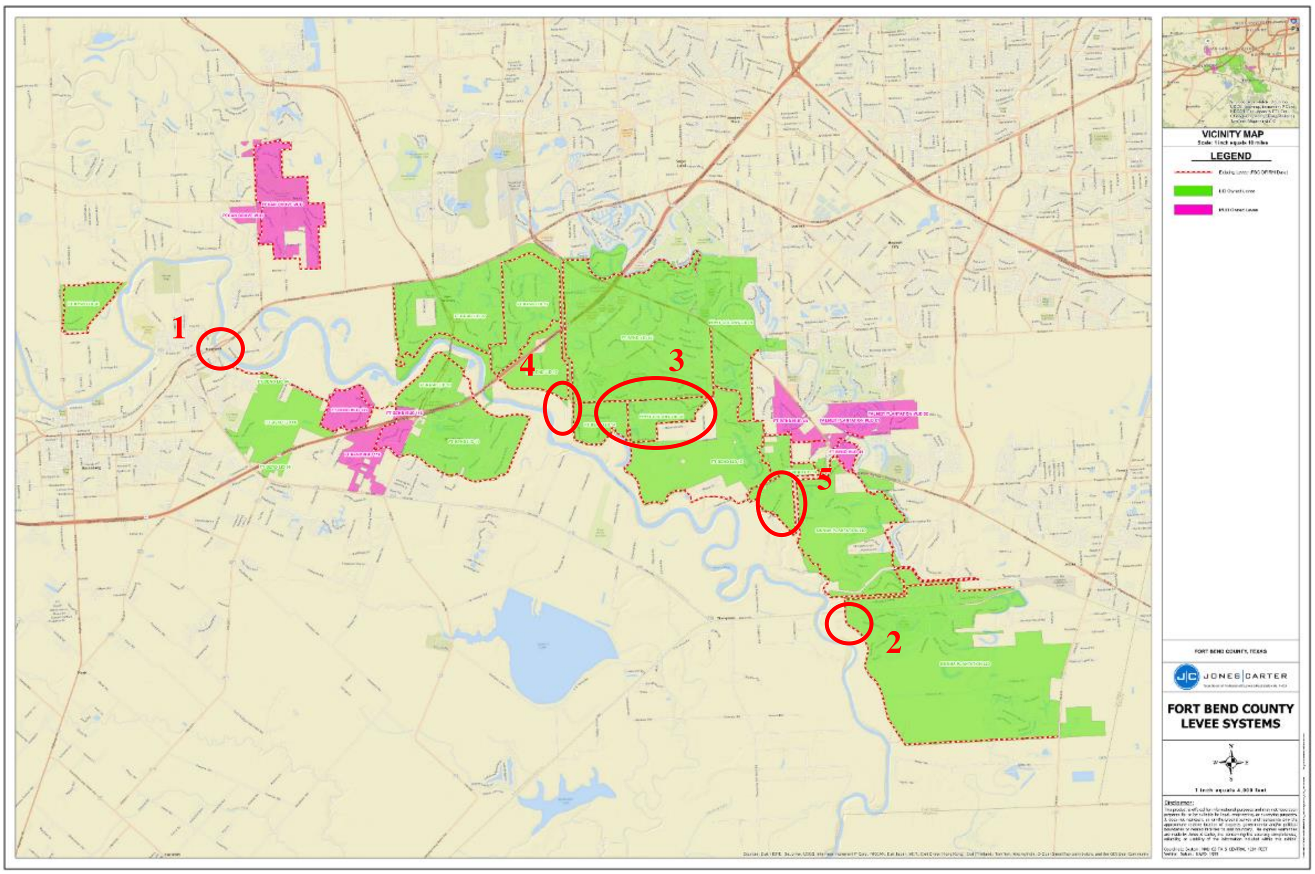

Figure 13. Fort Bend County Levee Systems. See following list for names of labelled systems. Existing levees are shown as red-dashed lines, LIDS in green, and MUDs in purple (from Jones|Carter), 1 – Richmond, Texas, USGS gauge on the Brazos River, 2 – Sienna Plantation Levee Improvement District levee surficial slough, 3 – First Colony LID 2, 4 – Ditch H, 5 – Flat Bank Diversion Channel

During the Hurricane Harvey flooding, the USGS stream gauge for the Brazos River at Richmond, Texas, (see Location 1 on Fig. 13) recorded a peak reading of 16.8 m (55.19 ft) corresponding to about 3,540 m^3/s (125,000 cfs). The gauge also recorded a total of 64 cm (25 inches) of rain between August 25 and August 29, 2017. The previous high-water record at the gauge was 16.7 m (54.74 ft) on June 2, 2016 during the Memorial Day Flood.

Overall, we understand that the Brazos River LID levees performed well, with no major failures, breaches, or overtopping. One incident of a surficial slide on the protected slope of a Sienna Plantation LID levee was reported and photographed by others as shown in Fig. 14 (see Location 2 on Fig. 13). The GEER team visited the First Colony LID 2 (see Location 3 on Fig. 13) and two of the drainage ditches that serve the LIDs (see Locations 4 and 5 on Fig. 13). Despite the good levee performance, flooding occurred within several LIDs due to the issues with storm water removal from the protected side behind the levees to the river side. Some LIDs were even completely cut off due to water surrounding the entirety of the LID.

Figure 14. Aerial photo (right) and Google Earth (left), August 30, 2017, 29.491844° N, 95.541017° W.

First Colony LID 2 (FCLID2)

The levee system in FCLID2 was built in 1988, protects 1,200 homes, which are collectively valued at $430,000,000, and performed well during the Hurricane Harvey event. Major elements of the system include the levees, a pump station with two 83-cubic-meter/minute (22,000-gallon/minute) pumps, a diesel generator for emergency power, and a flood gate structure with two 91-cm (36-inch) discharge outfalls and four 183-cm (72-inch) flood gates. During the event, an emergency pump was brought on site for backup. Due to the record rise of the Brazos River, both pump outlets were discharging under several feet of water but were able to keep up with internal stormwater accumulation. The water height on the river side reached a surveyed maximum elevation of 21.6 m (70.8 ft) along the FCLID2 levee. The levee crest at FCLID2, at elevation 23.8 m (78.1 ft), provided a freeboard of 2.2 m (7.3 ft). The high-water level within the pump station basin on the protected side of the levee is visible in Fig. 15 at about El. 19.8 m (65 ft) on the gauge. Fig. 16 shows the condition of the levee and drainage ditch that conveys water from the protected side of FCLID2 out to the Brazos River. The FCLID2 monitored the levee and pump station system 24 hours a day during the hurricane and high-water levels of the Brazos River. Routine levee maintenance by the FCLID2 included keeping a dense grass cover that is long enough to ensure solid root structures, irrigation for the grass cover and to prevent levee desiccation cracking, and repair of damage caused by rooting and burrowing animals. In FCLID2, wild hogs and fire ants are the main burrowing animal concerns.

Figure 15. FCLID2 drainage outfall / pumping station basin, showing four 1.4 m (60 inch) flood gates, high water line at ~19.8 m (65 ft) gauge height, levee in background (September 10, 2017, 29.55509° N, 95.61779° W).

Figure 16. FCLID2 drainage ditch to Brazos River facing FBLID14 levee. High water line and persistent water lines visible on FBLID14 levee (September 10, 2017, 29.55292º N, 95.61820º W).

Drainage Ditch Slope Slides

The team made observations of slope slides at two large drainage ditches in Fort Bend County: Ditch H and the Flat Bank Diversion Channel. The ditches serve as channels for drainage from and across the LIDs. Ditch H extends due north from the Brazos River, past LIDs 14, 2, and 17, and connects to the Bullhead Bayou and the Oyster Creek watershed in Sugar Land. Flat Bank Diversion Channel runs between Sienna Plantation LID North and LID 19 to connect Oyster Creek to Steep Bank Creek, which then connects to the Brazos River. Fig. 13 shows the locations of both ditches, and Fig. 17 shows a Google Earth aerial of Ditch H during the Harvey flooding.

The observed ditch geometries typically consisted of, from bottom to top, an approximately 20-m- (70-ft-) wide channel bottom, a 15-m- (50-ft-) high, 2.5H:1V channel slope, a small 1-m- (3-ft-) high collector ditch berm, a 1-m- (3-ft-) wide collector ditch, and an 2.4-m- (8-ft-) high levee with a 3H:1V slope. All ditch dimensions and slopes were estimated. The widths of the channels from levee crest to levee crest are about 150 m (500 ft) at Ditch H and 90 m (300 ft) at the Flat Bank Diversion Channel. The flood-side collector ditches at the base of the levees drain down the ditch slope through buried corrugated metal pipes (CMPs) to the channel.

The team observed several slope failures or sloughs along the slopes of Ditch H and numerous feral hog burrows. The east side slopes had some scarps that ranged in height from 15 to 99 cm (6 to 39 inches). Figs. 18 and 19 show two of the sloughs. The slope failures were likely due to softening of the clay soils by the flooding and the subsequent increases in stress on the slope due to drawdown of the flood water. Leakage from either an intact or ruptured CMP could have also contributed to one of the slope failures. The team also observed an erosion gulley below a drainage outfall on the University Avenue bridge (Fig. 20), which could have been prevented with hardened material protection (e.g., riprap, concrete blocks) below the outfall.

Figure 17. A Google Earth image of LID # 14 and Ditch H and its connection to the Brazos River (August 30, 2017).

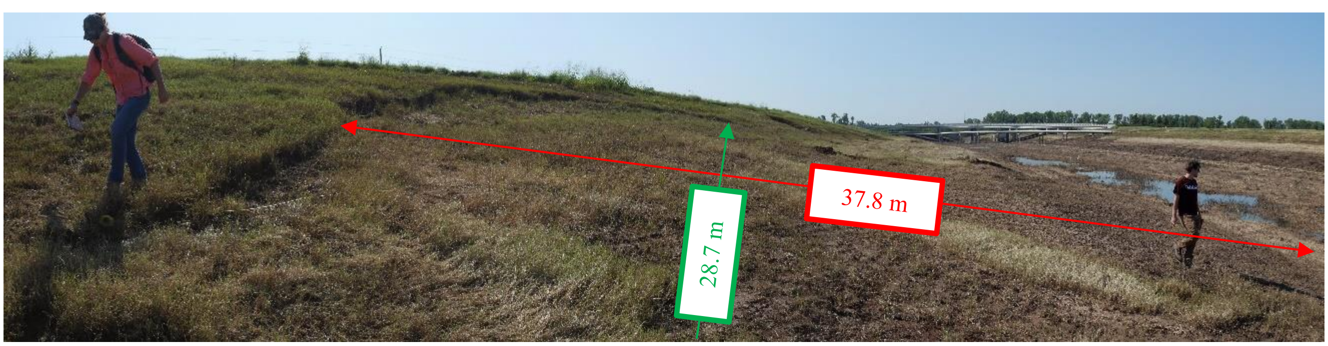

Figure 18. Ditch H levee, dimensioned slope failure (September 10, 2017, 29.55797°N, 95.63792°W).

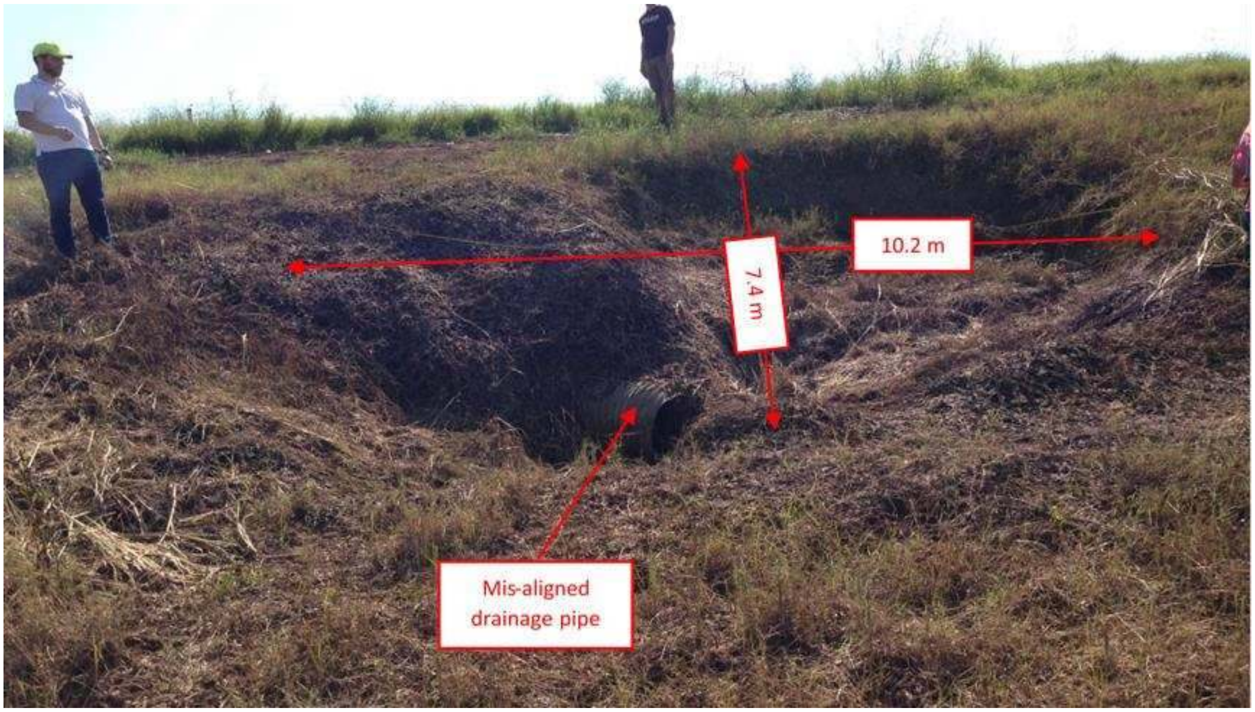

Figure 19. Sour hole at ruptured drainage pipe on Ditch H levee (September 10, 2017, 29.55759°N, 95.63768°W).

Figure 20. Erosion on Ditch H levee under the University Blvd Bridge due to flow impact from bridge drainage outfall (red arrow, September 10, 2017, 29.55902° N, 95.63744° W).

The team observed numerous slope failures along the Flat Bank Diversion Channel (see Fig. 13 for location) between 29.53103° N, 95.56200° W and 29.52572° N, 95.56201° W. Fig. 21 shows the dimensions of one large slide where the team collected a soil sample that was subsequently classified at the Kansas State University laboratory as low plasticity clay (CL) with a 21.3% moisture content. The team noted a drainage CMP outfall on an intact portion of the slope adjacent to this slide and another slide to the south. Figure 22 shows another embankment slough that extended into the base channel.

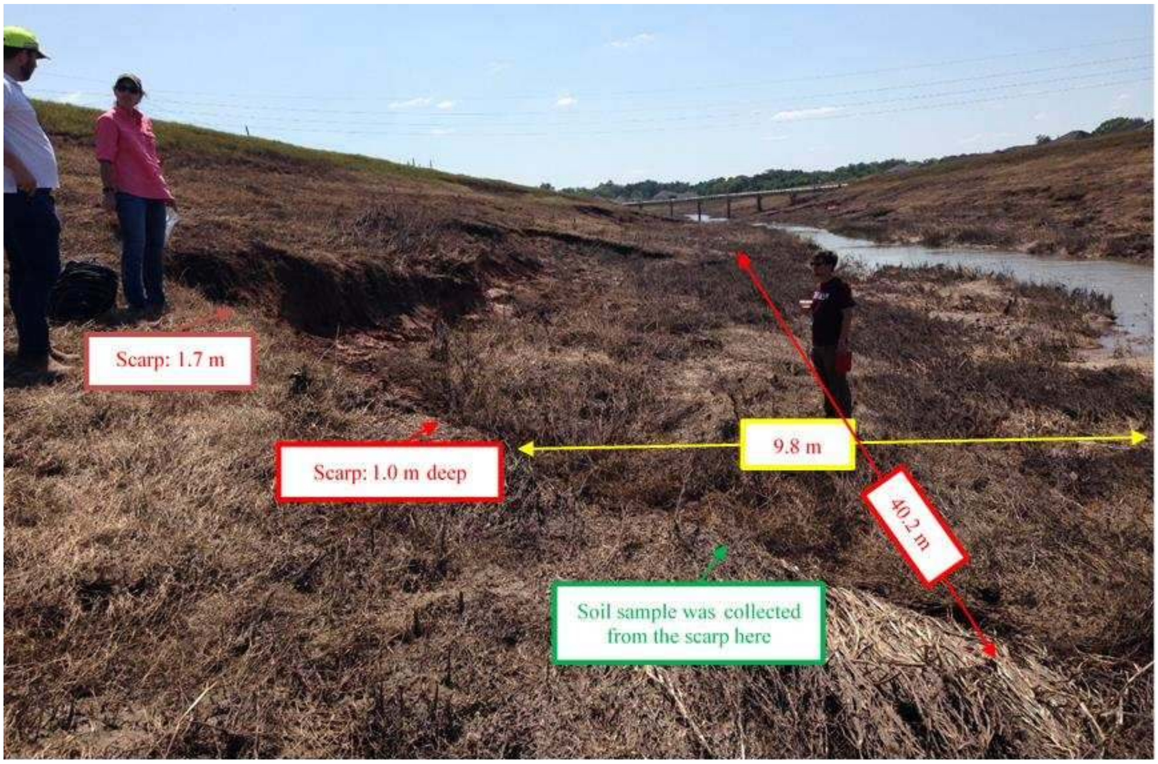

Figure 21. Slope failure north of damaged drainage pipe on the east side of ditch (September 10, 2017, 29.52647°N 95.56194°W),

Figure 22. Earth slumping on the west side embankment (September 10, 2017, 29.53103° N, 95.56200° W).

EROSION ALONG AREA RIVERS, BAYOUS, AND STREAMS

Buffalo Bayou

Buffalo Bayou normally is a slow-flowing waterway that runs from Katy, Texas, 85 km (53 miles) to the east, through much of Houston to the Houston Ship Channel into Galveston Bay. The bayou itself is part of the larger Buffalo Bayou watershed and is a critical part of the Houston flood control system, serving as the downstream channel for both the Barkers and Addicks Reservoirs as shown in Fig. 4. During and after Hurricane Harvey, local stormwater and outflows from the reservoirs into the Buffalo Bayou resulted in significant flooding along the waterway's path as shown in the inundation maps in Fig. 23. Flooding lasted well beyond the hurricane, with significant road closures along the bayou up to the GEER team visit's on September 9, 2017.

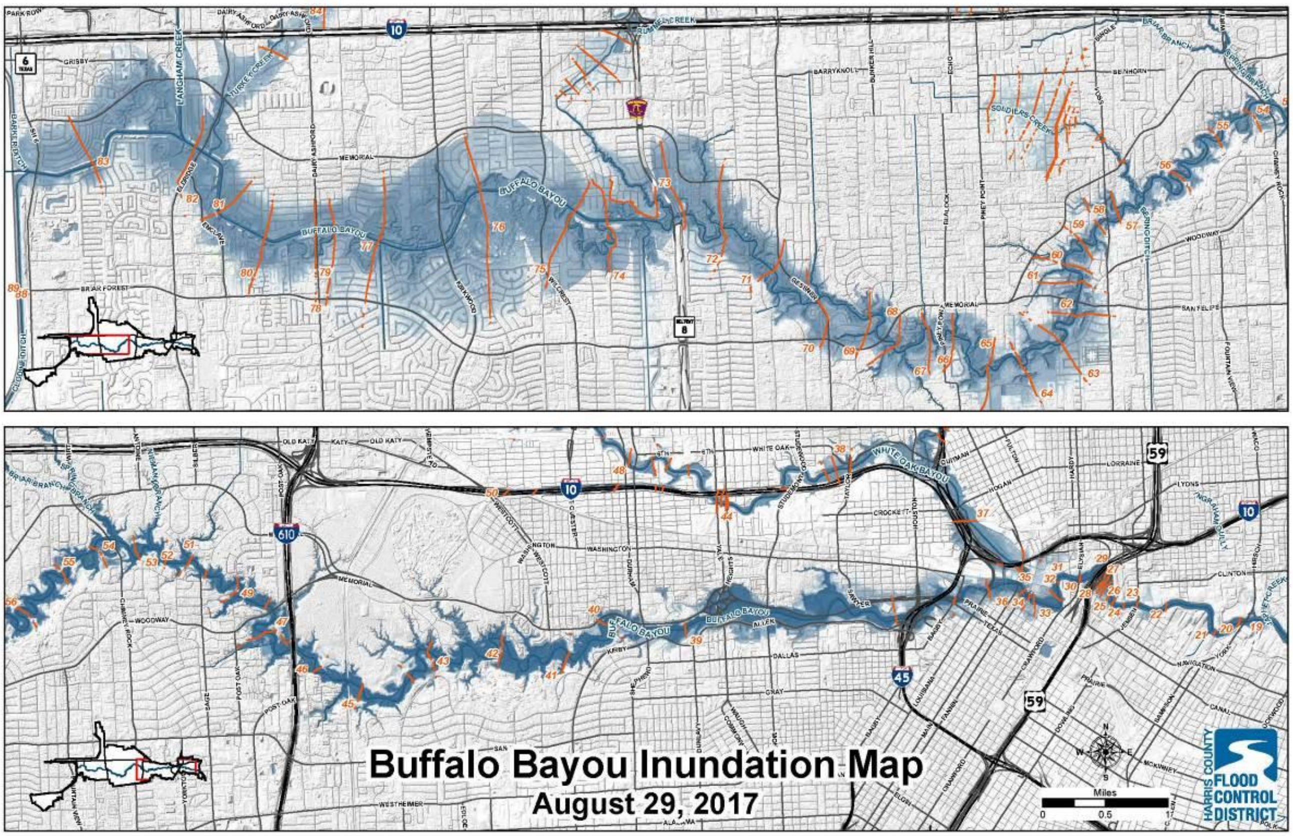

Figure 23. Buffalo Bayou inundation map (courtesy of Harris County Flood District).

Upon arrival of the GEER team at sites along Buffalo Bayou on September 9, 2017, the observed flows in the bayou were about 210 m^3/s (7,300 cfs) at the USGS Addicks gauge. Flooding of residential areas had been largely reduced by September 9, though much of the former parks and trails along the bayou were still inundated with water. Signs of the previous flooding could be seen with river debris noted on bridge girder and railings (see Fig. 24). No critical geotechnical failures were noted along the observed portions of Buffalo Bayou, but scour areas and a slope failure were observed (see Figs. 25 and 26).

Figure 24. Buffalo Bayou evidence of bridge overtopping (flood debris:) a) Montrose Bridge (September 9, 2017, 29.76307° N 95.39377° W), and b) Memorial Bridge (September 9, 2017, 29.76219° N 95.38425° W).

Figure 25. Buffalo Bayou evidence of scour a) Bridge abutment, and b) Downstream of Woodway Drive Bridge (September 9, 2017, 29.76457° N 95.45815° W).

Figure 26. Buffalo Bayous slope failures (September 9, 2017, 29.76318° N, 95.45945° W).

Beaumont – Neches River

As shown on Fig. 3, rainfall totals from Hurricane Harvey in the Beaumont / Port Arthur area were between 102 and 127 cm (40 and 50 inches) and were generally greater than those in the Houston area. This extraordinary amount of rain caused interior flooding behind levees and high stream and river flows.

In Beaumont, the team observed significant erosion scour along the Neches River in the downtown area. Riverfront Park, behind City Hall and located on an outside bend of the river, was severely affected with the loss of shoreline and undercutting of many park features. Fig. 1 shows the location of Beaumont within the study area. Fig. 27 shows the location of Riverfront Park along the Neches River. Fig. 28 shows aerial / satellite images from Google Earth of Riverfront Park taken before the Harvey flooding (January 2015) and during the Harvey flooding (September 2015), respectively.

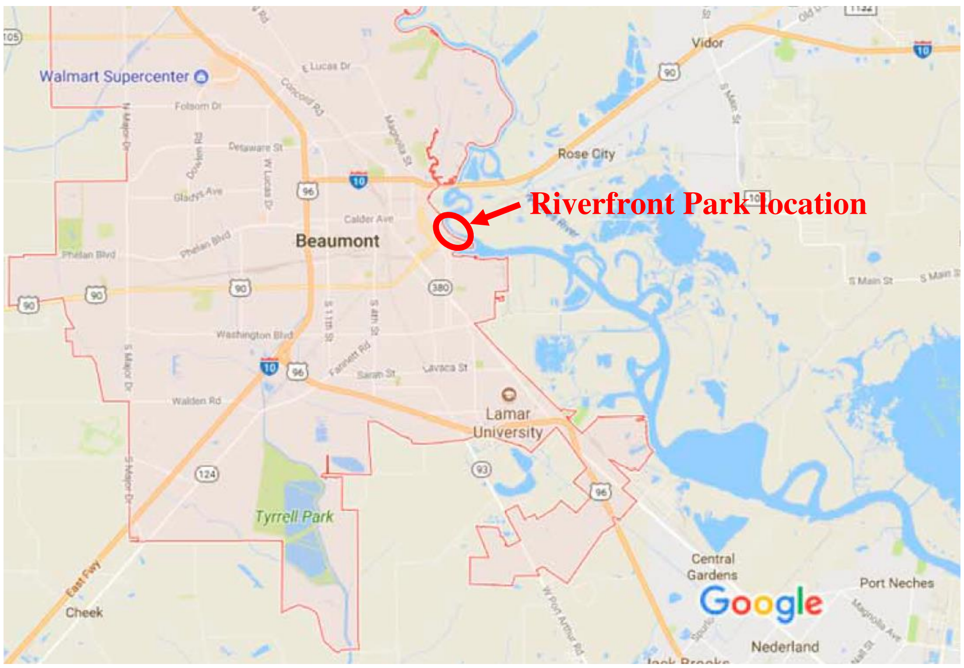

Figure 27. Riverfront Park location (Google Maps for source map).

Figure 28. Aerial images of Beaumont Riverfront Park, January 2015 (left) and September 3, 2017 (right) (Google Earth).

Figs. 29 and 30 show the loss of shoreline and scarps left by the Neches River erosion of the park shoreline, starting from an upstream section protected by riprap and extending through the downriver port area. The pre-hurricane park area shoreline was fronted with a riverwalk/dock (see aerial on Fig. 28), which was largely washed out. Based on pre-hurricane aerials on Google Earth, the shoreline had eroded up to about 15 m (50 ft) from the previous shoreline.

Figure 29. Scour under amphitheater structure. Scarp is estimated to be about 12 m (40 ft) back from previous shoreline (September 11, 2017, 30.08334° N, 94.09441° W).

Figure 30. Downstream end of park. Scarp is estimated to be about 10.7 m (35 ft) back from previous shoreline (September 11, 2017, 30.08184° N, 94.09278° W).

Scarps along the waterfront were up to about 5 m (15 ft) in height, with the highest scarps at the amphitheater. Exposed soils in accessible scarps were stratified, with fill (primarily sand) over stratified silty/clayey (slightly plastic to non-plastic) sand with shells and varying amounts of organic fines. The riprap-covered (30- to 46-cm- [12- to 18-in-] sized rubble concrete) shoreline at the north end of the park was largely intact.

Port Arthur

Port Arthur is located downstream of Beaumont on Sabine Lake, which connects to the Gulf of Mexico via the Sabine Pass. Port Arthur is the historic and current home of several refineries and port facilities. Sabine Lake at the Port Arthur is broad enough that flood flows from upriver have significantly less velocity and height than in Beaumont. However, because of its proximity to the Gulf, Port Arthur is at greater risk from hurricane storm surges and has several levee and floodwall structures to protect it from such surges. Based on our limited observations at several levee locations in Port Arthur and on discussions with local officials, the storm surge from Hurricane Harvey did not overtop or breach the Port Arthur levees. Most of the damage from Hurricane Harvey in Port Arthur occured behind the levees because interior drainage systems had to deal with the 102 to 127 cm (40 to 50 in) of rainfall accumulation.

Texas City

Texas City is located southeast of Houston in the Galveston Bay area (see Fig. 1 for location). It is protected by the Texas City Hurricane-Flood Protection Levee (TCHFPL) system and the nearby Texas City Dike. The TCHFPL is a 27-km- (17-mi-) long levee system that was built by the U.S. Army Corps of Engineers between 1962 and 1982 following Hurricane Carla. When Hurricane Ike hit the area in 2008, the levees, which ranged between 6 m to 7 m (19 to 23 ft) above sea level, managed to hold back the Galveston Bay storm surge with only about 0.6 m (2 ft) of remaining freeboard in some sections. The little damage that occurred was mostly due to erosion (Evans, 2008). The storm surge in this area during Hurricane Harvey was well below that of Hurricane Ike, and no storm damage was visible to the GEER team during their drive along a road built on top of the levee's crest.

ROADWAY / INFRASTRUCTURE DAMAGE

Beltway 8 Underpass Slab Uplift

Flooding caused roadway damage to and closure of a major area artery at the underpass intersection of the Sam Houston Parkway / Beltway 8 and Boheme Drive (see Fig. 1 for location, 29.76736° N, 95.56210° W). The parkway is depressed at this intersection and floods often enough that flood depth sign gauges are posted along the road to warn motorists of the standing water depth (see Fig. 31).

Figure 31. Beltway 8 / Boheme Drive underpass and flood depth signs (September 11, 2017, 29.76694° N, 95.56139° W).

The roadway damage consisted of an uplifted road slab (or slabs) on Beltway 8 and a washout of the adjacent access road, West Sam Houston Parkway N, which is supported about 6.7 m (22 ft) above the parkway by a cantilevered retaining wall consisting of precast panels, which are supported by H-pile reinforced concrete piers. It appears that flood water from the area west of the parkway flooded the access road, drained down behind the retaining wall, and uplifted the Beltway 8 slabs. These flows then washed out soil behind the wall and under the access road and adjacent sidewalk, leaving a 5 m- (17 ft) deep hole. Fig. 32 photographs show the state of the damaged roadway during and after the flooding event. Fig. 33 shows repair work conducted on the uplifted slabs.

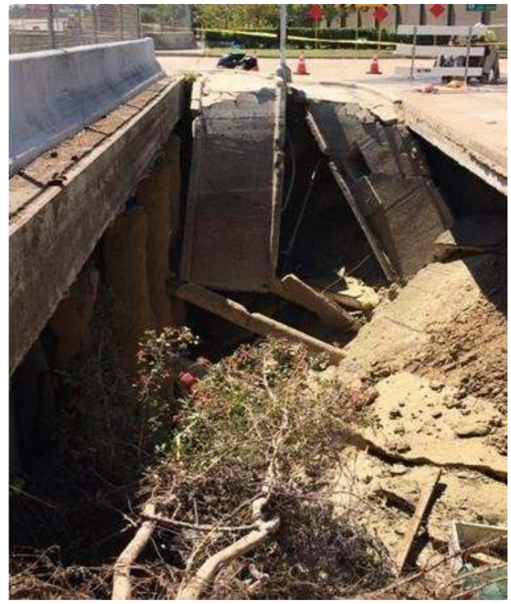

Figure 32. Damage of the walkway slab on Beltway 8 (left photo courtesy Brian Klein, a resident in the area, August 27, 2017, and right photo courtesy of a construction worker on site, 29.76735° N, 95.56219° W).

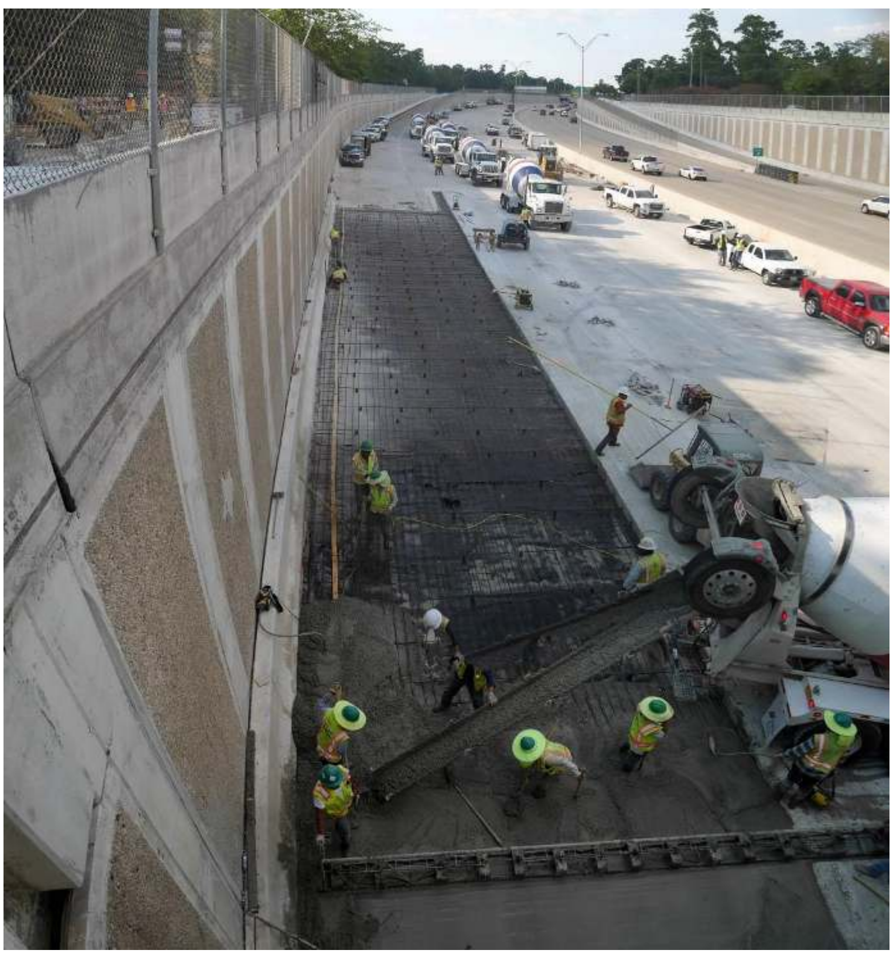

Figure 33. Road pavement repair in progress on Beltway 8 (September 10, 2017, 29.76736° N, 95.56208° W).

San Jacinto River I-45 & Missouri Pacific Railroad Bridges

The GEER team visited the bridge foundations and supports of Interstate 45 (I-45) and the Missouri Pacific Railroad over the West Fork San Jacinto River south of Conroe, Texas, approximately 16 km (10 mi) downstream of the Lake Conroe Dam on September 11, 2017 (see Fig. 1 for location, Fig. 34 for aerial). The USGS river gauge 08068000 on the West Fork San Jacinto River, downstream of the Lake Conroe Dam, measured maximum water levels of approximately 38.7 m (127 ft) on August 29, which the USGS correlates with 3,230 m^3/s (114,000 cfs) (statistic daily mean 13.5 m^3/s [477 cfs] prior to regulation by Lake Conroe).

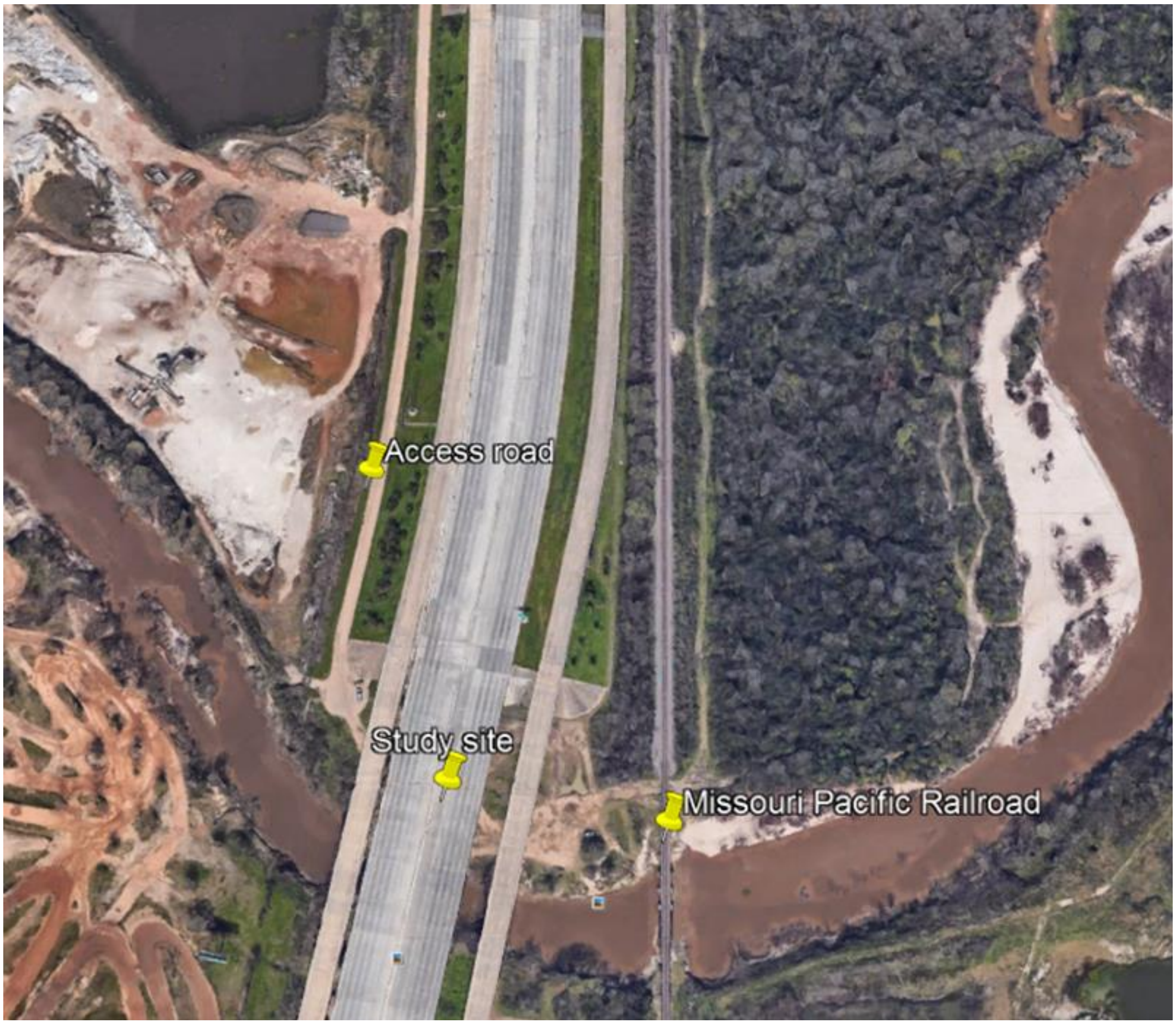

Figure 34. San Jacinto River Area observation locations (Google Earth image for April 2017, 30.24599° N, 95.45722° W).

As expected, bridge columns with no erosion control had variable amounts of accumulated debris (see Fig. 35) and scour (see Figs. 36 & 37). No measurable scour was observed around columns with erosion control (see Fig. 38), which included riprap and polymeric reinforcement. Fig. 40 shows the bank of the San Jacinto River from the north side, facing south. The riprap along the banks likely reduced the erosion of the fine, sandy soil. Fig. 41 shows an observed 2.4-m- (8-ft-) diameter scour hole in the sandy bank material. Despite the observed scour, no geotechnical or structural failures were observed on the I-45 Bridge over the San Jacinto River.

Figure 35. Observed debris on first column in flow direction. Debris pile is 1.24 m (49 inches) tall around the 1-m- (3-ft-) diameter bridge column (September 11, 2017, Time 10:04 CDT, 30.24688° N, 95.45796° W).

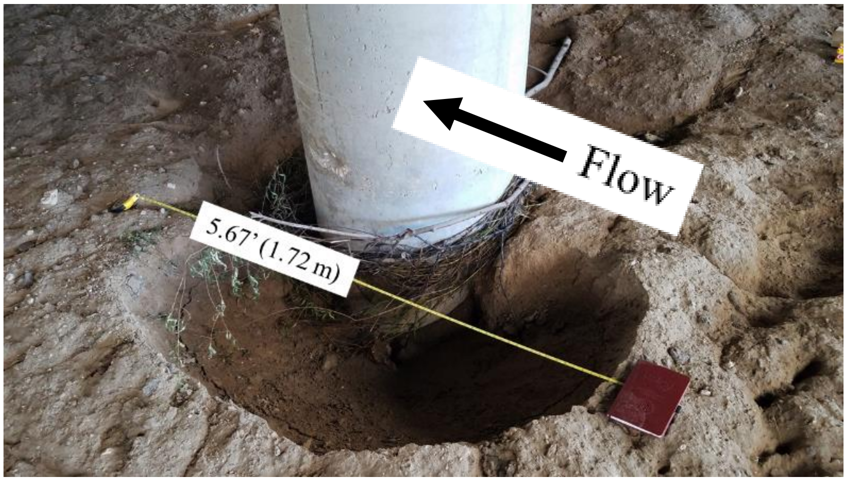

Figure 36. Bridge column scour (September 11, 2017, Time 10:06 CDT, 30.24688° N, 95.45796° W).

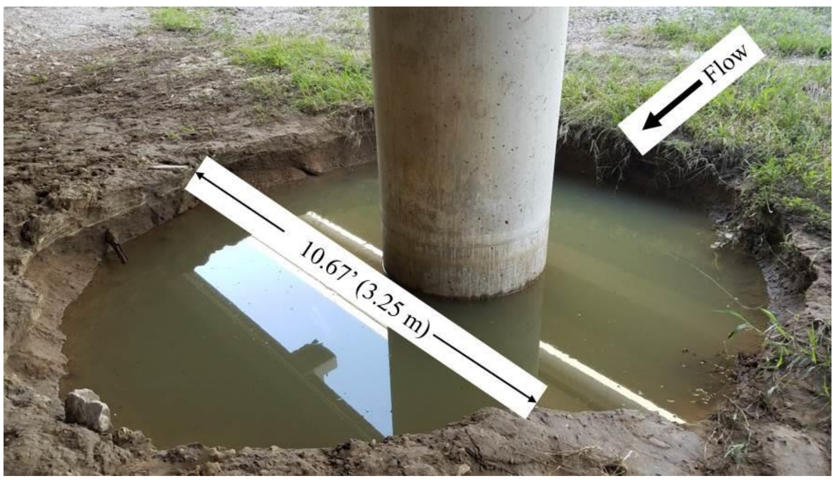

Figure 37. Scour hole on column closer to river. The hole was 3.7 m (12.3 ft) long in the flow direction and 3.25 m (10.67 ft) perpendicular to flow. The depth of the scour hole was 0.8 m (2.75 ft) from the existing ground (September 11, 2017, Time 10:23 CDT, 30.25071° N, 95.45703° W).

Figure 38. Erosion control riprap, including polymeric reinforcement, with minimal observed scour (September 11, 2017, Time 10:19 CDT, 30.24688° N, 95.45796° W).

Figure 39. Riprap along south bank of San Jacinto River (September 11, 2017, Time 10:56 CDT, 30.24574° N, 95.45761° W).

Figure 40. Scour around columns on San Jacinto Banks (sandy soil). The scour hole was approximately 2.4 m (8 ft) across and 0.6 m (2 ft) deep (September 11, 2017, Time 10:59 CDT, 30.243364°N, 95.46452°W).

Figs. 41 and 42 show the Missouri Pacific Rail Road Bridge downstream of I-45. Bank erosion was noted on the south bank of the San Jacinto River downstream of the railroad bridge. Fig. 42 shows debris on top of the pile caps and at the top of the bents on the railroad bridge. These high debris levels were consistent with the maximum measured gauge height during Harvey of approximately 10 m (33 ft) above average gauge height.

Figure 41. Bank erosion on the San Jacinto River downstream of I-45 and a railroad bridge parallel to the highway (September 11, 2017, Time 11:05 CDT, 30.24688° N, 95.45796° W).

Figure 42. Debris on railroad bridge indicating flow levels and scour around pile caps below current flow levels (September 11, 2017, Time 11:10 CDT, 30.24688° N, 95.45796° W).

FM 762 Road Culvert Washout

The culvert failure and subsequent washout of the 3900 Block of 762 in Rosenberg, Texas, southwest of Houston (see Fig. 1 for the general site location), was heavily featured on news coverage at the time of our visit. The replacement flow structure observed by the team was a set of three concrete ~1-m- (~3-ft-) diameter culverts running beneath the FM 762 highway, carrying flows from the adjacent railroad and shopping center culverts to the south into a creek that empties into the Brazos River. The failure of the road culverts was first reported on August 27, 2017, and resulted in a road closure through the time of our September 10, 2017 visit.

Erosion of the road progressed from the downstream side (see Fig. 43) until the entire width of the road washed out, stopping within 18 m (60 ft) of the adjacent railroad tracks. Repair construction was underway at the time of our visit. Possible erosion mechanisms could have included overtopping flow, culvert leakage or failure, or embankment seepage.

Figure 43. FM 762 Washout on August 27, 2017
(Courtesy of the Rosenberg Police Department, 29.5442° N, 95.7434° W).

Mustang Bayou Bridge

The erosion at the State Highway 35 Bypass bridge and pipe crossing over Mustang Bayou in the city of Alvin (see Fig. 1 for location) was typical for small waterways with high flow. Two shallow soil slump failures with slip depths of about 0.3 to 0.6 m (1 to 2 ft) were noted along the north bank of the bayou, one of which was beside and under a pipeline pile cap (Fig. 44).

Figure 44. Shallow soil failure along the north bank of Mustang Bayou, adjacent to pipe-support foundation (September 4, 2017, Time 12:48 CDT, 29.40889° N, 95.23234° W).

RESIDENTIAL IMPACTS

Area residents, especially in low-lying areas, suffered significant damage to their homes and businesses, but generally were able to return to start clean-up and repairs soon after the storm (see Figs. 45 and 46 for photos of typical flood damage debris on curbs). Area subsidence probably contributed to flood vulnerability and resulting residential damage, especially within the Addicks Reservoir. While many homeowners and businesses suffered greatly because of the damage, we hope and expect that the combination of rapid restoration of infrastructure and businesses, along with a robust local economy, has allowed for a quick recovery for the area.

Figure 45. Residential flood damage debris, Houston.

Figure 46. Residential flood damage debris, Port Arthur.

SUMMARY

Rain, not storm surge or wind, caused the observed damage in Houston, Beaumont, and Port Arthur by overwhelming stormwater management facilities and creating high flows in area waterways. The dams and levees that the GEER team visited performed well from a geotechnical perspective, although we understand that fifteen private, non-regulated dams did fail or suffered significant damage. The USACE dams, Addicks and Barker, showed no signs of structural distress and served their primary function of reducing flood damage to large areas of Houston, including the central business district. The USACE made controlled releases of water from the dams to Buffalo Bayou to reduce risks associated with high reservoir water levels. The high flows in Buffalo Bayou from area runoff and these releases were what flooded low elevation residences and businesses along the bayou. Area levees built and maintained by LIDs protected their districts from riverside flooding. However, interior flooding occurred within several LIDs where rainfall accumulation and pumping against high riverside pressures overwhelmed LID stormwater management facilities.

The team observed numerous shallow slide failures along drainage channels associated with the LIDs. Slopes constructed in area clays are very susceptible to these shallow slides, most likely due to infiltration of water into desiccation cracks, softening of the clay, and increased loading when water levels in adjacent channels drop. High river, bayou, and stream flows eroded the soil around and under constructed facilities, as one would expect. The most pronounced observed damage occurred to the Riverfront Park along the Neches River in Beaumont. Some limited damage to transportation structures occurred along flooded waterways and at a major highway underpass. The observed damage to transportation facilities was either repaired or under repair, and traffic had returned to normal dense levels at the time of our observations.

The team prepared a GEER report with additional details about observations, which, like all GEER reports, is available on the GEER website at http://www.geerassociation.org/.

ACKNOWLEDGEMENTS

The GEER reconnaissance of the Houston / Beaumont / Port Arthur areas affected by Hurricane Harvey was supported by the National Science Foundation (NSF) through the Geotechnical Engineering Program under Grant No. CMMI-1266418. Any opinions, findings, and conclusions or recommendations expressed in this material are those of the authors and do not necessarily reflect the views of the NSF.

The research team wishes to acknowledge the gracious logistical support and technical interaction provided by the U.S. Army Corps of Engineers, who granted access and hosted the visit to the Barker and Addicks Dams. Traci Thomas and Brad

Boothby of the Galveston District briefed the team, served as guides, and answered questions during the visits to the dams. Zach Weimer also deserves thanks for access and information about the First Colony LID 2 facilities and experience with the flooding. Brian Klein graciously shared photographs of the Beltway 8 damage.

The Geotechnical Extreme Events Reconnaissance (GEER) Association is made possible by the vision and support of the NSF Geotechnical Engineering Program Directors: Dr. Richard Fragaszy and the late Dr. Cliff Astill. GEER members also donate their time, talent, and resources to collect time-sensitive field observations of the geotechnical effects of extreme events.

Finally, we'd like to thank Ellen M. Rathje, Ph.D., P.E., University of Texas at Austin, who provided guidance, information, and encouragement as the GEER Steering Committee liaison, as well as Prof. Jonathan D. Bray, Ph.D, P.E., University of California at Berkeley, in his capacity as past Chair of GEER, for logistical support and encouragement for the reconnaissance effort.

REFERENCES

Di Liberto, Tom. (2017). "Reviewing Hurricane Harvey's catastrophic rain and flooding." <https://www.climate.gov/news-features/event-tracker/reviewing-hurricane-harveys-catastrophic-rain-and-flooding> (Sept. 2018).

Evans, Thayer. (2008). "Levee System Kept Texas City from Flooding." *Houston Chronicle*, <www.chron.com/news/hurricanes/article/Levee-system-kept-Texas-City-from-flooding-1622095.php> (Nov. 5, 2008).

Google Earth. (2017). Various aerial images.

Harris County Flood Control District. (2017). "Hurricane Harvey Flooding Impacts in Connection with Reservoirs." <https://www.hcfcd.org/hurricane-harvey/flooding-impacts-in-connection-with-the-reservoirs/>.

Harris County Flood Control District. (2017). "Projects & Studies, Buffalo Bayou." <https://www.hcfcd.org/projects-studies/buffalo-bayou/>.

Jones|Carter. (undated) Plan – "Fort Bend County Levee Systems."

National Oceanic and Atmospheric Administration. (2017). "Highest Water Levels During Hurricane Harvey as of 8/31/17." <https://www.tidesandcurrents.noaa.gov/images/quicklook_high_wl/Extreme_WL_Harvey_2017.png>.

National Weather Service. (2017). "Major Hurricane Harvey - August 25-29, 2017." <http://www.weather.gov/crp/hurricane_harvey>.

The Weather Channel. (2017). "Historic Hurricane Harvey's Recap" <https://weather.com/storms/hurricane/news/tropical-storm-harvey-forecast-texas-louisiana-arkansas>.

U.S. Army Corps of Engineers, Galveston District. (2009). "2009 Master Plan, Addicks and Barker Reservoirs." <www.swg.usace.army.mil/Portals/26/docs/2009%20Addicks%20 and%20Barker %20MP.pdf>.

U.S. Army Corps of Engineers, Galveston District, and Pannell, Richard P. (2016) "Addicks and Barker Dam Safety Update.". <www.swg.usace.army.mil/Portals/26/AddicksBarker%209Mar2016%20Public%20Mtg%20Brf%20(final).pdf> (March 9).

U.S. Army Corps of Engineers, Galveston District. "Addicks and Barker Dams, Construction Update Map." <http://geospatial.swg.usace.army.mil/StoryMaps/CESWG/AddicksBarker2/>.

U.S. Geologic Survey. "Texas Gulf Coast Groundwater and Land Subsidence, Over Forty Years of Research in the Houston-Galveston Region." <https://txpub.usgs.gov/houston_subsidence/home/>.

U.S. Geologic Survey, National Water Information System. (2017). "Web Interface for various gaging stations:"

- "USGS 08073500 Buffalo Bayou nr Addicks, Texas." <https://waterdata.usgs.gov/nwis/inventory/?site_no=08073500&agency_cd=USGS>;>
- "USGS 08114000 Brazos Rv at Richmond, Texas." <http://fbcdd.maps.arcgis.com/apps/Viewer/index.html?webmap=b612be63a5404c89807e7e207e13d10d>;
- "USGS 08068000 W Fk San Jacinto Rv nr Conroe, Texas." <https://waterdata.usgs.gov/nwis/inventory?agency_code=USGS&site_no=08068000>.